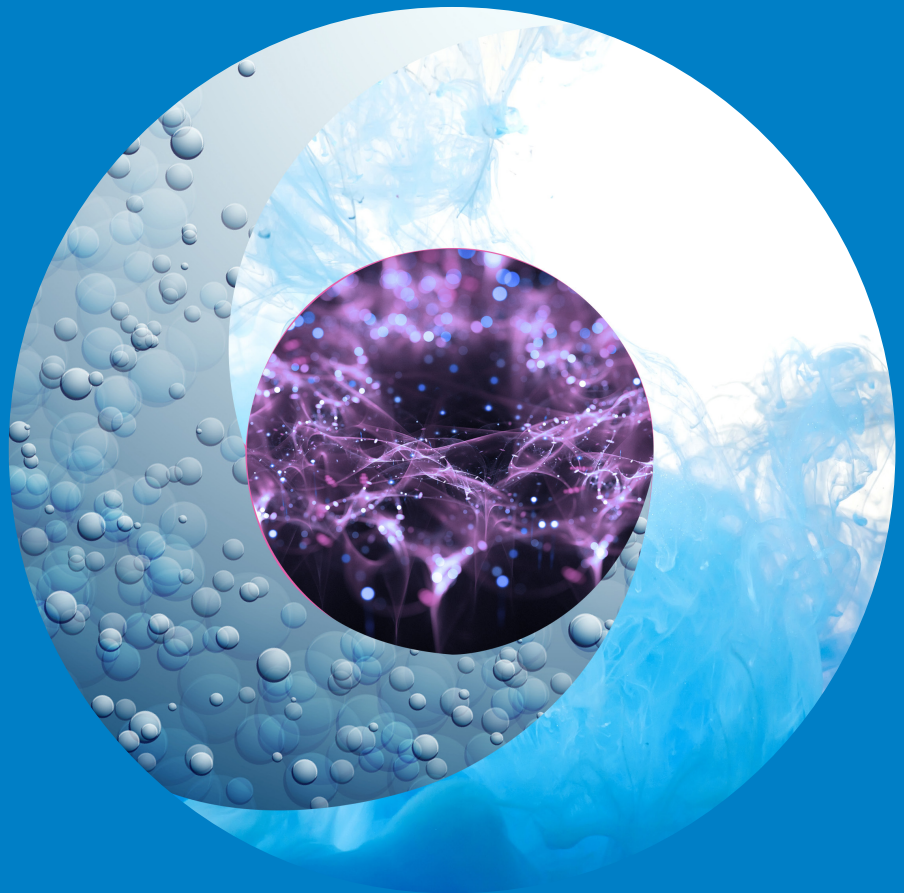


Department of Chemical and Metallurgical Engineering

Numerical Simulation of Reactive Crystallization in Stirred Tank Reactors

Wenli Zhao



Numerical Simulation of Reactive Crystallization in Stirred Tank Reactors

Wenli Zhao

A doctoral dissertation completed for the degree of Doctor of Science (Technology) to be defended, with the permission of the Aalto University School of Chemical Engineering, at a public examination held at the Auditorium KE2 of the school on the 20th of April, 2018 at 12 noon.

Aalto University
School of Chemical Engineering
Department of Chemical and Metallurgical Engineering
Research Group of Chemical Engineering

Supervising professor

Professor Ville Alopaeus, Aalto University, Finland

Thesis advisor

Professor Antonio Buffo, Politecnico di Torino, Italy

Preliminary examiners

Professor Daniele Marchisio, Politecnico di Torino, Italy

Professor Hongyuan Wei, Tianjin University, China

Opponent

Professor Tuomas Koiranen, Lappeenranta University of Technology, Finland

Aalto University publication series

DOCTORAL DISSERTATIONS 56/2018

© 2018 Wenli Zhao

ISBN 978-952-60-7915-8 (printed)

ISBN 978-952-60-7916-5 (pdf)

ISSN-L 1799-4934

ISSN 1799-4934 (printed)

ISSN 1799-4942 (pdf)

<http://urn.fi/URN:ISBN:978-952-60-7916-5>

Unigrafia Oy

Helsinki 2018

Finland



Author

Wenli Zhao

Name of the doctoral dissertation

Numerical Simulation of Reactive Crystallization in Stirred Tank Reactors

Publisher School of Chemical Engineering**Unit** Department of Chemical and Metallurgical Engineering**Series** Aalto University publication series DOCTORAL DISSERTATIONS 56/2018**Field of research** Chemical Engineering, Fluid Dynamics**Manuscript submitted** 4 December 2017**Date of the defence** 20 April 2018**Permission to publish granted (date)** 12 March 2018**Language** English **Monograph** **Article dissertation** **Essay dissertation****Abstract**

Model development is essential for design and scale up of multiphase chemical reactors to provide a better understanding of physical and chemical phenomena between phases at different scales. Mathematical descriptions of the reactive crystallization include mass transfer, chemical reaction, crystallization kinetics, population balance and hydrodynamics, which consist of a set of partial differential equations with high nonlinearity. A full simulation with a commercial computational fluid dynamics (CFD) software is possible with existing computational resources but not desirable during the initial stage of reactor design. The purpose of this thesis is to explore the mechanism of multiphase reactive crystallization and develop a compartmental model to combine hydrodynamics and detailed reaction efficiently.

The chemical system of $\text{CO}_2(\text{G})\text{-H}_2\text{O}(\text{L})\text{-Mg}(\text{OH})_2(\text{S})$ is chosen as the practical application to reveal mechanisms of multiphase reactive crystallization, which couple the reactive dissolution, chemical absorption and crystallization. As modeling of such complex system is challenging, the reactive dissolution of $\text{Mg}(\text{OH})_2(\text{S})$ in $\text{HCl}(\text{aq})$ and reactive crystallization of $\text{CaCO}_3(\text{S})$ from $\text{CO}_2(\text{G})$ and $\text{Ca}(\text{OH})_2(\text{aq})$ system are studied separately. The first part of the thesis introduces the gas-liquid and solid-liquid mass transfer models based on two-film theory and Nernst-Planck electroneutrality. In addition, enhancement factor is adopted to modify mass transfer fluxes when chemical reaction occurs in liquid film. Then, population balance model is presented along with several solution techniques to calculate particle size distributions of gas bubbles and final crystal products. The closure models include nucleation and growth of crystals, breakage, coalescence and agglomeration of gas bubbles and crystals. Finally, a compartmental model combining the flow field obtained by CFD simulation and reaction mechanisms is constructed to estimate the influence of flow field on multiphase crystallization.

The compartmental modelling results show that heterogeneous mixing has a strong influence on local mass transfer rates and size distribution of final crystal products. By appropriate division of the fluid domain, compartmental model can offer a more efficient simulation for reactive crystallization without the limitation of chemical components and geometries of different reactors. This characteristic highlights the potential extensibility and portability of compartmental model in reactor design and scale up.

Keywords Crystallization, CFD, Population balance, Compartmental modeling**ISBN (printed)** 978-952-60-7915-8**ISBN (pdf)** 978-952-60-7916-5**ISSN-L** 1799-4934**ISSN (printed)** 1799-4934**ISSN (pdf)** 1799-4942**Location of publisher** Helsinki**Location of printing** Helsinki**Year** 2018**Pages** 140**urn** <http://urn.fi/URN:ISBN:978-952-60-7916-5>

Preface

The thesis was done based on the research in the Chemical Engineering Research Group at the Department of Chemical and Metallurgical Engineering, School of Chemical Engineering at Aalto University between 2012 and 2017.

When I initially started my PhD study on numerical simulation I met countless problems and felt tired and unconfident every day. I received many supports during that period, without which I could not accomplish my study. Therefore, I would like to express my appreciation to many individuals who have contributed to my work.

First and foremost, I am deeply grateful to thank Professor Ville Alopaeus for his dedication in guiding me during the entire PhD study. His patience and inspiration have made the past 5 years a valuable and memorable period in my life. Instead of offering a direct solution, he always encourages me to keep positive and stay away from comfortable zone when my study is bogged down. Critical and independent thinking is the most valuable thing I received during my PhD study.

My sincere thanks also for my co-authors, Prof. Marjatta Louhi-Kultanen, Prof. Zuoliang Sha, Prof. Antonio Buffo, Dr. Zheng Liu, Dr. Bing Han, Dr. Mei Han, Dr. Kaj Jakobsson, Elina Nauha, Mohamed Ali Jama and Ningfeng Zhang for their contributions to my publications and to this thesis. In addition, I would thank Sirje Liukko, Lasse Westerlund and Sirpa Aaltonen for their supports in administrative issues.

The financial support from FLUKI project and PORLIS project are gratefully acknowledged.

At last, I would show my deep thankfulness to my parents Jiying Zhao and Yuhong Wang for their mostly emotional support and encouragement during my study.

Otaniemi, Espoo, November 30, 2017

Wenli Zhao

List of Publications

In this thesis, four publications are contained as listed in the followings.

- I. Zhao Wenli, Han Bing, Jakobsson Kaj, Louhi-Kultanen Marjatta, Alopaeus Ville. Mathematical model of crystallization of magnesium carbonate with carbon dioxide from the magnesium hydroxide slurry. *Computers & Chemical Engineering* (2016), 87,180-189.
- II. Zhao Wenli, Jama Ali Mohamed, Buffo Antonio, Alopaeus Ville. Population balance model and experimental validation for reactive dissolution of particle agglomerates. *Computers & Chemical Engineering* (2018), 108,240-249.
- III. Zhao Wenli, Buffo Antonio, Alopaeus Ville, Bing Han, Marjatta Louhi-Kultanen. Application of the Compartmental Model to the Gas–Liquid Crystallization of CO₂-Ca(OH)₂ Aqueous System in a Stirred Tank. *AIChE Journal* (2017), 63, 378-386.
- IV. Guo Zhichao, Han Wenxiang, Zhao Wenli, Li Liye, Wang Baodong, Xiao Yongfeng, Alopaeus Ville. The effect of microwave on the crystallization process of magnesium carbonate from aqueous solutions. *Powder Technology* (2018), 328, 358-366.

Author's Contributions to the Publications

- I. Zhao Wenli developed, solved and verified the models, fitted the model parameters against the experimental data, analyzed the results and wrote the paper. Bing Han and Louhi-Kultanen Marjatta provided experimental data. Jakobsson Kaj and Alopaeus Ville assisted in developing the model and writing the paper.
- II. Zhao Wenli developed the models, carried out the experimental validation, fitted the model parameters against the experimental data, analyzed the results and wrote the paper. Jama Ali Mohamed, Buffo Antonio and Alopaeus Ville assisted in developing the model and writing the paper.
- III. Zhao Wenli carried out the experiments with the co-authors, developed the model, analyzed the results, and wrote the paper. Bing Han and Louhi-Kultanen Marjatta assisted in performing the experimental validation. Buffo Antonio and Alopaeus Ville assisted in developing the model and writing the paper.
- IV. Guo Zhichao, Han Wenxiang and Li Liye carried out the experimental validation and wrote the paper. Zhao Wenli developed the mathematical models, fitted the model parameters against the experimental data, analyzed the results with the co-authors and assisted in writing the paper. Alopaeus Ville assisted in developing the model. Wang Baodong and Xiao Yongfeng provided the experimental equipment.

List of Abbreviations and Symbols

a	specific mass transfer area	m^{-1}
A	surface area of particle or compartment	m^2
$B(L_i, L_j)$	breakage table	m^{-1}
B_p	volumetric growth rate of particle in p -th category	$m^3 \cdot s^{-1}$
c	concentration of liquid component	$mol \cdot m^{-3}$
D	diffusion coefficient	$m^2 \cdot s^{-1}$
d_b	bubble diameter	m
E, E_i	enhancement factor and reaction factor	[-]
Eo	Eötvös number	[-]
f	partial molar volume	$m^3 \cdot mol^{-1}$
F	liquid flow rate between compartment	$m^3 \cdot s^{-1}$
$F(L_i, L_j)$	agglomeration or coalescence frequency	$m^3 \cdot s^{-1}$
Fl_G	gas flow number	[-]
$g(L_i, L_j)$	breakage frequency	s^{-1}
$G(L_i)$	growth rate	$m \cdot s^{-1}$
Ha	<i>Hatta number</i>	[-]
H_{cc}	Henry's coefficient	$mol \cdot m^{-3} \cdot atm^{-1}$
$J_{n,pr}$	primary nucleation rate	$\# \cdot m^{-3} \cdot s^{-1}$
$J_{n,se}$	secondary nucleation rate	$\# \cdot m^{-3} \cdot s^{-1}$
k	mass transfer coefficient	$m \cdot s^{-1}$
k_g	empirical constant for crystal growth	$mol^{-g} \cdot m^{(3g+1)} \cdot s^{-1}$
$k_{n,pr}$	empirical constant for primary nucleation	$mol^{-n1} \cdot m^{(3n1-3)} \cdot s^{-1}$
$k_{n,se}$	empirical constant for secondary nucleation	$kg^{-1} \cdot mol^{-n2} \cdot m^{(3n1+3b-3)} \cdot s^{a-1}$
K_{sp}	solubility product of particles	$mol^2 \cdot m^{-6}$
K_w	water auto-ionization constant	$mol^2 \cdot m^{-6}$
M	torque moment	$N \cdot m$
m_k	k -th moment of the particle size distribution	m^{k-3}
N	impeller speed	rpm
N_s	impeller speed	rps
$n(L)$	number density	$\# \cdot m^{-4}$
n_m	mass transfer rate of component m	$mol \cdot m^{-3} \cdot s^{-1}$
NB	total number of compartments	[-]
NC	total number of size categories	[-]

N_m	mass transfer flux of component m	$\text{mol}\cdot\text{m}^{-2}\cdot\text{s}^{-1}$
P	Pressure	atm
R	gas constant	$\text{J}\cdot\text{K}^{-1}\cdot\text{mol}^{-1}$
Re_N	impeller Reynold number	[-]
S	supersaturation	$\text{mol}\cdot\text{m}^{-3}$
Sc	Schmidt number	[-]
Sh	Sherwood number	[-]
T	Temperature	K
U_{ij}	velocity of gas bubble	$\text{m}\cdot\text{s}^{-1}$
V	total volume	m^3
v_p	volume of particle in p -th category	$\text{m}^3\cdot\text{mol}^{-1}$
$Y(L_i)$	paricle number density,	$\#\cdot\text{m}^{-3}$
z	charge of cationic and anionic	[-]

Greek letters

ε	turbulent energy dissipation	$\text{m}^2\cdot\text{s}^{-3}$
ν	kinematic viscosity	$\text{m}\cdot\text{s}^{-1}$
$\beta(L_i, L_j)$	daughter size distribution (DSD) function	m^{-1}
δ_L	thickness of liquid film	m^{-1}
η	Kolmogorov length scale	m
η_T	Kolmogorov time scale	s
ϑ	relative dissipation factor	[-]
μ	dynamic viscosity	$\text{Pa}\cdot\text{s}$
$\xi(L_i, L_j)$	growth table	[-]
ρ	density	$\text{kg}\cdot\text{m}^{-3}$
σ	surface tension	$\text{kg}\cdot\text{s}^{-2}$
φ	volume fraction	[-]
$\chi(L_i, L_j, L_k)$	agglomeration table	[-]
Ψ	collision efficiency	[-]
$\Omega(L_i)$	nucleation table	[-]

Subscripts

ag	agglomeration
br	breakage
cl	coalescence
co	collision
disp	dispersion
G	gas phase
het	heterogeneous
hom	homogeneous
i, j, k	index of particle size class
in	index of the feeding compartment

L	liquid phase
m	index of components
out	index of the flow out compartment
p	index of phase
S	solid phase
slip	velocity

Contents

Preface.....	i
List of Publications.....	iii
Author's Contributions to the Publications	iv
List of Abbreviations and Symbols.....	v
Contents	viii
1. Introduction.....	1
2. Mass transfer	5
2.1 Phase equilibrium.....	5
2.2 Mass transfer coefficient (k).....	6
2.2.1 Gas-liquid mass transfer coefficient	7
2.2.2 Solid-liquid mass transfer coefficient	8
2.3 Electroneutrality.....	9
2.4 Enhancement factor for mass transfer	10
3. Population balance	13
3.1 General formulation	13
3.2 Numerical solution	14
3.2.1 HMMC.....	16
3.2.2 QMOM.....	17
3.3 Closure models	17
3.3.1 Supersaturation.....	18
3.3.2 Nucleation	18
3.3.3 Growth.....	19
3.3.4 Coalescence and Agglomeration	20
3.3.5 Breakage.....	22
4. Flow dynamics	27

4.1	Computational flow dynamics (CFD)	29
4.1.1	Basic two-fluid equation.....	29
4.1.2	Turbulence model.....	29
4.1.3	Interphase forces	30
4.2	Compartmentalization	30
4.3	Compartmental model	32
4.3.1	Governing equations.....	32
4.3.2	Flows between compartments	34
4.3.3	Closure models	35
5.	Applications of mass transfer, population balance and compartmental model	39
5.1	Experimental equipment	39
5.2	Modelling of mass transfer, reaction and crystallization in gas-solid-liquid system	
	40	
5.2.1	Introduction.....	40
5.2.2	Experimental validation	41
5.2.3	Results and discussion.....	41
5.3	Population balance modeling for solid-liquid reactive dissolution	45
5.3.1	Introduction.....	45
5.3.2	Experimental validation	45
5.3.3	Results and discussion.....	46
5.4	Compartmental modeling of gas-liquid crystallization	52
5.4.1	Introduction.....	52
5.4.2	Experimental validation	53
5.4.3	Numerical details.....	53
5.4.4	Compartment number/size independence study	54
5.4.5	Result and discussion	55
5.5	The influence of microwave field on reactive crystallization.....	61
5.5.1	Introduction.....	61
5.5.2	Experimental validation	61
5.5.3	Numerical details.....	61
5.5.4	Results and discussion.....	62
6.	Conclusions	67
	REFERENCES	71

1.Introduction

Metallurgy process refers to extraction of metal from ores and refinement of the raw metal into a purer form to produce alloys (Seetharaman, 2005). Metallurgy, in terms of performance, can be categorized into physical metallurgy, mechanical metallurgy, chemical metallurgy, mineral dressing, powder metallurgy and engineering metallurgy (Gupta, 2003). Powder metallurgy is concerned with production and processing of powdery forms of materials by means of crushing, grinding, chemical reactions and electrolytic deposition. Reactive crystallization plays an important role during formation of pure metal or crystal alloys due to high purity of product, moderate operating conditions and low energy cost (Mersmann, 2001).

Reactive crystallization, also known as precipitation, refers to the crystallization process driven by fast chemical reaction, which is commonly used in CO₂ capture and storage, mineral carbonation and production of fine chemicals and biomaterials (Varma et al., 2011; Olajire, 2013; Ye et al., 2016). Many of the reactive crystallization processes are carried out in either liquid-liquid or gas-liquid phase systems, in which chemical reaction, interphase transport of species and energy, crystallization kinetics and hydrodynamics are dominating physical mechanisms. The design and scale-up of a crystallizer remains challenging due to the complex physical and chemical processes and still depends on the expensive cold-flow experiments from the bench scale to the pilot scale and highly empirical or semi-empirical correlations (Jones et al., 2004). In general, empirical methods have several limitations: (1) homogeneous flow regime is assumed in the domain, which is seldom maintained even in the lab scale multiphase reactor; (2) flow pattern in the vicinity of dispersed phase is unpredictable with the present measuring techniques; (3) empirical correlations and physical parameters are typically case dependent; (4) hydrodynamic similarities cannot preserve between processes with different scales (Joshi & Nandakumar, 2015). Therefore, a better understanding of the mechanisms occurs at different phases and scales (molecular, macro-micro and equipment scale) and their interactions are needed in the process development.

With rapid development of computer power in the past decades, the mathematical prediction of reactive crystallization becomes possible. However, a practical and high fidelity

model (computational fluid dynamics coupled with detailed chemistry models) is still demanding. On one hand, physical models of reactive crystallization are complex, involving descriptions of mass transfer, chemical reaction, crystallization and multiphase flow dynamics. On the other hand, mathematical expressions consist of algebraic, ordinary and partial differential equations with strong nonlinearity and mutual coupling (Yang & Mao, 2014). Multiscale simulation represents the most promising methodology that provides the insights into crystallization kinetics and chemical reaction at the molecular scale, transport phenomena at particle scale and the flow fields at the equipment scale (Bi & Li, 2004). The synthesis of the mechanisms at different scales provides a powerful and rigorous computational tool for rational and effective design procedure of crystallizers.

As the most important character of the dispersed phase in the reactive crystallization, the variation of particle size distribution (PSD) caused by physical source terms including nucleation, growth, agglomeration and breakage can be described by solving population balance equations (PBEs) (Randolph & Larson, 1988). For a gas-liquid system, the driving force of the source terms, namely supersaturation, is mainly determined by the chemical reaction at molecular scale and gas-liquid mass transfer at particle scale. The intrinsic kinetics of the chemical reaction is decided by the electron cloud interactions, which can be described by utilizing the computational chemistry tools, such as density functional theories (DFT) (Gubbins et al., 2011) and molecular dynamics (MD) (Nørskov et al., 2011). The mass transfer usually becomes a rate-limiting step of reactive crystallization when an instantaneous reaction occurs at ambient temperature and pressure. For a gas-liquid system, the physical and chemical gas absorption could govern the crystallization performance (Wachi & Jones, 1991). For a gas-solid-liquid system, the dissolution rate of solid reactants could limit the overall crystallization rate (Han et al., 2014).

The mass transfer fluxes and areas originated from various parameters such as local micro-scale mixing intensity and physical properties of dispersion should be predicted separately (Laakkonen, 2006). Therefore, mixing becomes crucial during the modelling of reactive crystallization: the non-uniform mixing condition affects the local mass transfer fluxes by altering the mass transfer coefficient and specific mass transfer area of the dispersed phase in the domain. The breakage and coalescence rates of the dispersed phase are strongly affected by the local turbulent intensity. Moreover, the crystallization kinetics, including nucleation and crystal growth, are commonly calculated by power-law function of the average supersaturation in the multi-phase crystallization, which leads to different prediction in stirred tanks with various shapes and sizes.

Computational fluid dynamics (CFD) is an effective method to explore the hydrodynamics that dominate the overall crystallization rate and the crystal properties in the liquid solution (Ashraf Ali et al., 2013; Rigopoulos & Jones, 2001; Wei & Garside, 1997). For the multiphase reactive crystallization, nevertheless, the exploitation of a straightforward and effective model that couples the flow field with several specific models, such as mass transfer,

chemical reaction, PBEs for particles (crystals and bubbles) may require a heavy workload of computation. It could be realizable to moderate the CFD computational costs by using a coarse-grained description of the flow field with a compartmental simulation (Patterson, 1975) in which CFD is just employed to collect the hydrodynamic information, including the fluid fields and physical properties for each defined compartment. After that, the compartmental model can be solved by coupling the hydrodynamics and detailed physical sub-models to describe the influence of fluid field on the investigated processes.

Four publications are included in this thesis. Publication [I] proposed a mathematical model of crystallization of MgCO_3 with CO_2 from the $\text{Mg}(\text{OH})_2$ slurry, including a description of dissolution of $\text{Mg}(\text{OH})_2$, absorption of CO_2 and crystallization of MgCO_3 . In publication [II], a population balance model coupled with a mass transfer model is introduced to simulate the simultaneous shrinkage and breakage of particles during the reactive dissolution of particle agglomerates in stirred tank. The high-order moment-conserving method of classes is adopted to solve the population balance equation. Publication [III] investigated effects of fluid field on the gas–liquid reactive crystallization of $\text{CO}_2(\text{G})\text{-Ca}(\text{OH})_2(\text{aq})$ system in a stirred tank reactor with compartmental model. Publication [IV] investigated the influence of microwave field on the reactive crystallization of MgCO_3 .

2. Mass transfer

Mass transfer rates between two fluid phases depend on mass transfer fluxes and interfacial area. The mass transfer fluxes across a phase boundary are mainly determined by the properties of fluid phases, the concentration differences and the degree of turbulence, which can be described by two film theory, penetration theory, surface renewal theory and film penetration theory. The two film theory suggests that the resistance to transfer in each phase could be considered as lying in two adjacent thin films, namely gas film and liquid film (Whitman, 1924). The transfer across these films is regarded as a steady state molecular diffusion. The turbulence in the bulk fluid disappears at the film interface. Higbie (1935) suggested that the transfer process was essentially attributed to fresh material being brought by the small eddies to the interface, where an unsteady state transfer took place for a fixed period at the freshly exposed surface, that is generally known as the penetration theory. Then Danckwerts (1951) modified the penetration theory and suggested that the species could remain on the surface for random periods. Subsequently, Toor and Marchello (1958) proposed a more general theory, the film-penetration theory, and discussed the limitations of the earlier models. In the multiphase reactive crystallization, the gas absorption and reactive dissolution are relevant phenomena. Therefore, the gas-liquid mass transfer and solid-liquid mass transfer models will now be considered. The mass transfer rate can be generally presented as:

$$n_m = N_m \cdot a \quad (2.1)$$

$$N_m = k(c_{interface} - c_{bulk}) \quad (2.2)$$

where m is the index of component; n is the mass transfer rate; N is the mass transfer flux; a is the specific mass transfer area; k is the overall mass transfer coefficient; $c_{interface}$ and c_{bulk} are the concentration of component on the interface and in the bulk solution respectively.

2.1 Phase equilibrium

Phase equilibrium refers to the transport of matter between phases (solid, liquid, or gas) of the system without conversion of one species to another. These phases may interconvert from one to another, but the overall amount of any one particular phase is constant if the system is in phase equilibrium. As a limit for mass transfer, the phase equilibrium is commonly adopted to estimate the concentration of components on the phase boundary.

For the gas-liquid mass transfer, the Henry's law can describe the equilibrium concentration in the liquid exposed to a gas containing a solute. There are various forms of Henry's law which have been discussed in the literature (Sander, 2015). The concentration based equation is introduced to calculate the liquid concentration on the interface ($c_{L,i}$):

$$c_{L,i} = H_{cc}(P,T)c_{G,i} \quad (2.3)$$

where $H_{cc}(P,T)$ is the Henry's coefficient; $c_{G,i}$ is the gas concentration at the interface. For the gas absorption in a stirred tank, the gas-liquid mass transfer resistance mainly remains in the liquid film. Therefore, the concentration of $\text{CO}_2(\text{G})$ on the interface is assumed equal to the concentration of the inlet gas phase (pure carbon dioxide) in Publication [I] and Publication [III].

For the solid-liquid mass transfer, the transport of uncharged molecules can be described by the typical Noyes-Whitney equation (Noyes & Whitney, 1897). The solid-liquid interface concentration is commonly calculated from the solubility of solid component. The reactive dissolution rate is instead determined by the transport of charged ions. The electric neutrality principle should be naturally satisfied during the estimation of the interface concentration. In Publication [II], the interface concentrations of component are calculated numerically based on the rigorous physical constraints including electroneutrality, water dissociation and solubility equilibrium for the reactive dissolution of $\text{Mg}(\text{OH})_2(\text{s})$ into aqueous HCl solution.

2.2 Mass transfer coefficient (k)

The prediction of mass transfer coefficient, k , depends on the choice of mass transfer theories. In the two-film theory, k is directly proportional to the diffusivity and inversely proportional to the film thickness. According to the penetration theory, it is proportional to the square root of the diffusivity. When all surface elements are exposed for an equal time, it is inversely proportional to the square root of time of exposure. When random surface renewal is assumed, it is proportional to the square root of the rate of renewal. In the film-penetration theory, the mass transfer coefficient is a complex function of the diffusivity, the film thickness, and either the time of exposure or the rate of renewal of surface. In addition, gas-liquid mass transfer coefficient (k_L) and solid liquid mass transfer coefficient (k_S) were

treated differently based on different theories in the literature (Beenackers & Van Swaaij, 1993).

2.2.1 Gas-liquid mass transfer coefficient

The gas-liquid mass transfer coefficient is often obtained from an empirical correlation that is volumetric mass transfer coefficient ($k_L a$), in the design and scale up of gas-liquid contactor, such as bubble column, internal-loop and external-loop airlift reactor and fluidized bed. In the literature, $k_L a$ is calculated either by using dimensionless groups or energy input based on Kolmogorov's theory under the assumption of spatial homogeneity (Yawalkar et al., 2002). As previously mentioned, mass transfer fluxes and areas should be predicted separately since they are governed by different physical phenomena. k_L is mainly determined by the properties of species and the turbulent intensity. Several studies have proved the fact that the penetration theory is widely accepted for the description of gas-liquid mass transfer under various geometries and operating conditions (Babcock et al., 2002; Billet and Schultes, 1993; Kawase and Hashiguchi, 1996). k_L significantly depends on the turbulent intensity, expressed as a function of the dissipated energy, while the surface renewal rate is considerably higher than that found for bubbles in free rise under potential flow (de Figueiredo & Calderbank, 1979). The exposure time, t_e , is necessarily affected by the eddies or turbulence at Kolmogorov length scale. Subsequently, Garcia-Ochoa and Comez (2004) proposed the empirical models based on the Hebie penetration theory and Kolmogorov's theory for the gas-liquid mass transfer in the stirred tank, which has been adopted in Publication [I] and [III]:

$$k_L = \frac{2}{\pi} \sqrt{D_m} \left(\frac{\varepsilon_T \rho_L}{\mu_L} \right)^{1/4} \quad (2.4)$$

where ρ_L is density of the liquid phase; μ_L is dynamic viscosity of the liquid phase; ε_T is turbulent energy dissipation.

The mass transfer area is strongly influenced by average bubble diameter (d_b) and gas hold up (φ), which can be calculated as (Bhavaraju et al., 1978; Garcia-Ochoa & Gomez, 2004):

$$d_b = \frac{7}{10} \frac{\sigma_G}{(P_N/V_L)^{2/5} \rho_L^{1/5}} \left(\frac{\mu_L}{\mu_G} \right)^{1/10} \quad (2.5)$$

$$\frac{\varphi}{1-\varphi} = 0.819 \frac{v_G^{2/3} N^{2/5} T^{4/15}}{g^{1/3}} \left(\frac{\rho_L}{\sigma_G} \right)^{1/5} \left(\frac{\rho_L}{\rho_L - \rho_G} \right) \left(\frac{\rho_L}{\rho_G} \right)^{-1/15} \quad (2.6)$$

where V_L is the total volume of liquid phase; N is the impeller rate; T is the diameter of the impeller; σ_G is the surface tension of bubbles. Corresponding experimental validations under different geometries of reactor and a wide range of operating conditions have been performed in the literature (Garcia-Ochoa & Gomez, 2004). In Publication [I], the tank average mass transfer area was predicted by Eq. (2.5) and Eq. (2.6). In Publication [III], the local mass transfer area was obtained by tracking local bubble size distribution with population balance model.

2.2.2 Solid-liquid mass transfer coefficient

Empirical correlations of the solid-liquid mass transfer coefficient (k_S) can be classified into four methods, including dimensional analysis, Kolmogorov's theory of isotropic turbulence, slip velocity theory and analogy between mass transfer and momentum transfer (Pangarkar et al., 2002). The dimensional approach can be performed easily without considering the effects of various system parameters on the k_S and can only be adopted to the similar geometry with similar operating conditions (Lal et al., 1988). Kolmogorov's theory claims that the k_S can be predicted only by the specific power input without considering geometric configuration, particle loading and density difference. Nevertheless, the available experimental results in the literature indicated that, for constant energy dissipation rate, k_S is still a function of the type, size and position of the impeller (Harriott, 1962; Nienow, 1969; Nienow & Miles, 1978). The slip velocity theory is developed by assuming particles are well suspended in the turbulent flow. Meanwhile, steady state forced convection is assumed to describe mass transfer flux (Harriott, 1962; Nienow, 1975), which is an important improvement compared with Kolmogorov's theory. The calculation of a characteristic slip velocity, however, requires numerical solution of complex equations and information of local turbulence. In the larger reactor, prediction of k_S with slip velocity theory is especially challenging due to the difficulties in measurement of local turbulence intensity (Hughmark, 1974). The approach based on analogy between momentum transfer and mass transfer presents a straightforward way to relate the drag coefficient and the mass transfer coefficient either in two phase system or three phase system (Datta & Pangarkar, 1994, 1996). A more detailed investigation about the influence of system configuration, operating conditions and physical properties on k_S and systematical analysis of the application and limitations regarding the mentioned approaches has been discussed elaborately in the literature (Pangarkar et al., 2002).

After comparing a range of scales and operating conditions of the literature experiments with our studies, including particle size, volume of tank and mixing intensity, the following correlation was found to be the most appropriate prediction to calculate k_S in Publication [I] and [II] (Asai et al., 1989):

$$Sh = \left[2^{5.8} + \left(0.61 Re_\epsilon^{0.58} Sc^{1/3} \right)^{5.8} \right]^{1/5.8} \quad (2.7)$$

where Sh is the Sherwood number; Re_ε is the particle Reynolds number; Sc is the Schmidt number. There are many ways to define the particle Reynolds number. In this case, the inertial contribution is mainly caused by the agitation of the impeller. Therefore, the Re_ε is calculated based on the energy dissipation rate and particle size (Levins & Glastonbury, 1972):

$$Re_\varepsilon = (\varepsilon_T L^4)^{1/3} / \nu_L \quad (2.8)$$

where L is the particle size; ν_L is the kinematic viscosity of liquid. The Sh_p and Sc_p are component-dependent dimensionless numbers which are defined as:

$$Sh = k_s L / D_p \quad (2.9)$$

$$Sc = \mu_L / (\rho_L D_p) \quad (2.10)$$

2.3 Electroneutrality

In dilute nonelectrolyte solutions, diffusion is mainly determined by diffusivities and concentration gradient of species. However, solutes do not diffuse independently in electrolyte solutions. The electroneutrality of mass transfer fluxes and charged components should be naturally satisfied. This aspect can be addressed by introducing the Nernst-Planck equation, which can calculate the flux of ionic components affected by electric field and concentration gradient in the liquid film (Newman, 1991). The flux between interface and bulk solution, N_m , is the summation of convection of electrolyte, diffusion and migration:

$$N_m = \bar{c}_m v - D_m \nabla c_m - z_m \frac{D_m}{RT} F \bar{c}_m \nabla \phi \quad (2.11)$$

The electric current exists in the solution can be calculated as:

$$I = F \sum_m (z_m N_m) = F \sum_m (z_m \bar{c}_m v) - F \sum_m (z_m D_m \nabla c_m) - F^2 \nabla \phi \sum_m (z_m^2 \frac{D_m}{RT} \bar{c}_m) \quad (2.12)$$

where z_m is charge of component m ; F is Faraday constant; R is gas constant; T is temperature; $\nabla \phi$ is potential gradient. In the case of mass transfer between electrically neutral solids and surrounding solution, the current (I) must be zero. In addition, the convection term (first one on the right hand side) is zero due to electroneutrality in the liquid solution. After reorganizing Eq. (2.12), the mass transfer flux can be presented as:

$$N_m = z_m \frac{D_m}{RT} c_m \left[\frac{\sum_m (z_m D_m \nabla c_m)}{\sum_m (z_m^2 D_m c_m)} \right] - D_m \nabla c_m \quad (2.13)$$

Under ideal mixing hypothesis, mass transfer resistances exist in liquid films. Linear concentration profiles can be assumed:

$$\nabla c_m \approx \frac{\Delta c_m}{\delta} \quad (2.14)$$

$$\Delta c_m = c_{m,interface} - c_{m,bulk} \quad (2.15)$$

$$c_m = \frac{c_{m,interface} + c_{m,bulk}}{2} \quad (2.16)$$

$$k_{s,m} = \frac{D_m}{\delta} \quad (2.17)$$

After substituting Eq. (2.14) – Eq. (17) into Eq. (2.13), the flux between interface and bulk solution becomes:

$$N_m = k_{s,m} \Delta c_m - k_{s,m} z_m c_m \left[\frac{\sum_m (z_m k_{s,m} \Delta c_m)}{\sum_m (z_m^2 k_{s,m} c_m)} \right] \quad (2.18)$$

The first term on the right side of Eq. (2.18) is the conventional form of mass transfer rate, namely Noyes-Whitney equation (Noyes & Whitney, 1897). The second term is the contribution of Nernst-Planck equations. In Publication [I] and [II], the reactive dissolution rate of $\text{Mg}(\text{OH})_2(\text{s})$ is described by the mass transfer fluxes of Eq. (2.18) which ensures that mass transfer fluxes always fulfill electroneutrality. Thus, the transports of cations and anions of all the components are taken into account in the solid-liquid mass transfer model.

2.4 Enhancement factor for mass transfer

For the convective mass transfer accompanied with complex chemical reactions, the previous theories can still be adopted calculate the mass transfer fluxes. However, necessary modifications are needed since the actual concentration profiles are no longer linear due to chemical reaction as in Fig 1 (Trambouze et al., 1988).

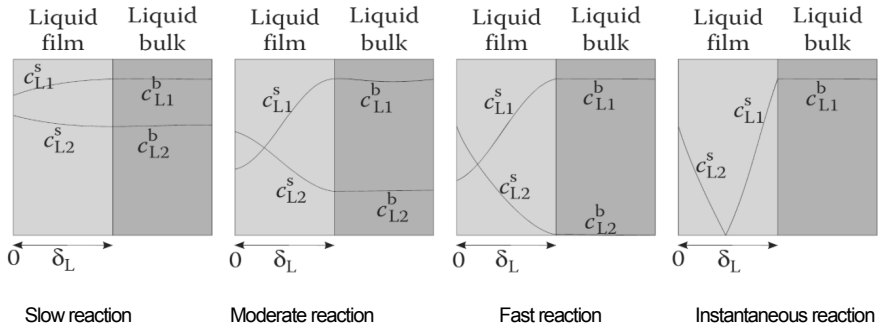


Fig. 2.1 Influence of reaction kinetics on the concentration gradients in the liquid film for gas-liquid mass transfer.

The chemical reaction shown in Fig. 2.1 may vary from slow to extremely fast. The instantaneous reactions usually occur at the interface while fast reactions occur within the liquid film, and slow reactions occur at both liquid film and bulk solution. A more detailed description of different reaction types is summarized Table 2.1 (Salmi et al. , 2011).

Table 2.1 Classification of the chemical reaction along with mass transfer

Regime	Description
Slow reaction	Very slow reaction in the liquid film and bulk solution. Linear concentration gradient in the liquid film.
Moderate reaction	Moderate reaction in the liquid film and in the liquid bulk. Nonlinear concentration gradient in the liquid film.
Fast reaction	Fast reaction in the liquid film. No chemical reaction in the bulk solution. Nonlinear concentration profiles in the liquid film. The gas-phase component concentration is zero in the liquid phase.
Instantaneous reaction	Instantaneous reaction in the reaction zone in the liquid film. The diffusion rates dominant reaction velocity.

In order to consider the influence of chemical reaction on the mass transfer rate, an enhancement factor (E) which is defined as the ratio of the absorption rate with and without the reaction, is presented as follows:

$$E = \frac{\text{Mass transfer rate with chemical reaction}}{\text{Mass transfer rate without chemical reaction}} \quad (2.19)$$

In Publication [I], the dissolution rate of $\text{Mg}(\text{OH})_2(\text{S})$ in $\text{Mg}(\text{OH})_2(\text{S})\text{-CO}_2(\text{G})\text{-H}_2\text{O}(\text{L})$ system is modified by second order chemical reaction between $\text{CO}_2(\text{aq})$ and OH^- , which can be calculated as (van Krevelen & Hoftijzer, 1948):

$$E = \frac{Ha \sqrt{(E_i - E)/(E_i - 1)}}{\tanh\left[Ha \sqrt{(E_i - E)/(E_i - 1)}\right]} \quad (2.20)$$

where Ha is Hatta number; E_i is the reaction parameter. Meanwhile, the $\text{CO}_2(\text{G})$ absorption rate in Publication[I] and [III] were modified by the same reaction.

3. Population balance

3.1 General formulation

Nowadays, population balance model is a broadly accepted tool that can describe the multiphase systems characterized by dispersed phase, such as solid particles, bubbles or droplets, with a distribution of properties in a continuous phase (Buffo & Alopaeus, 2016). There are numerous reviews of population balance targeting specific area in the literature. Besides the early contribution (Randolph & Larson, 1988), which specifically addressed crystallization processes, there have been books on population balance dealing with its generic treatment (Ramkrishna, 2000) or focusing on applications to biomedical engineering (Hjortso, 2005). In the multiphase system, the dispersed phases would experience complex interaction changing the particle size distribution (PSD). These interactions could occur between the dispersed phase, between the dispersed and the continuous phase, and between dispersed phase and parts of the equipment (Alopaeus et al., 2006).

For the gas-solid-liquid reactive crystallization, the prediction of PSD of the dispersed phases is vital to the process development and scale up. The bubble behaviors significantly influence the gas-liquid mass transfer rate, which governs the following chemical reaction rate and the supersaturation of the crystallization process. Meanwhile, the crystal behaviors directly determine the PSD of final products. These relevant mechanisms can be described by simultaneously solving the PBEs of crystals and bubbles with the corresponding closure models: nucleation, growth, agglomeration and breakage for crystals as well as growth, coalescence and breakage for bubbles. The dynamic population balance equation for a homogeneous volume element can be generally written for one positive-valued internal coordinate as (Rod and Misek, 1982; Marchisio et al., 2003):

$$\begin{aligned} \frac{\partial(n(L))}{\partial t} = & \int_L^\infty \beta(L, \lambda) g(\lambda) n(\lambda) d\lambda + \frac{L^2}{2} \int_0^L \frac{F\left(\left(L^3 - \lambda^3\right)^{1/3}, \lambda\right) n\left(\left(L^3 - \lambda^3\right)^{1/3}\right) n(\lambda)}{\left(L^3 - \lambda^3\right)^{2/3}} \\ & - g(L) n(L) - n(L) \int_0^\infty F(L, \lambda) n(\lambda) d\lambda + \frac{\partial(G(L) n(L))}{\partial L} + J_n + \dot{n}(L)_{in} - \dot{n}(L)_{out} \quad (3.1) \end{aligned}$$

where L and λ are the internal coordinates, namely diameters of particles; $n(L)$ is number density; $\beta(L, \lambda)$ is daughter size distribution (DSD) function; $g(L, \lambda)$ is breakage frequency; $F(L, \lambda)$ is the agglomeration or coalescence frequency; $G(L)$ is the growth rate; J_n is the primary nucleation rate. Terms on the left-hand side describes the evolution of number density function (NDF). The terms on the right-hand side are birth of particles by breakage, birth by agglomeration, death by breakage, death by agglomeration or coalescence, growth, primary nucleation, particles flow into the domain and particles flow out of the domain. For homogenous systems, all terms only depend on internal coordinate, L . For inhomogeneous systems, all terms are generally also functions of spatial location (external coordinate). Although the analytical solution of the PBE exists under limited and well-defined simplified cases, for the realistic physical process, efficient numerical techniques are required to solve the PBE with complex integro-differential form.

3.2 Numerical solution

For population balance model with only one internal-coordinate, namely monovariate problem, most widely adopted approaches are the moment methods (Hulburt & Katz, 1964) and the method of classes (Valentas & Amundson, 1966). Then, several approaches for the solution of bivariate and multivariate PBE are presented (Iveson, 2002; Braumann et al., 2010x). The most famous approaches available for solving PBE can be classified into the following groups: Monte Carlo methods, moment based method and classes method (Buffo et al., 2013). Ramkrishna (2000) presented a more comprehensive review of various methods in his book.

Monte Carlo methods are based on the solution of a set of stochastic differential equations that dominate the behaviors of dispersed phase, which mostly concern artificial realizations of the multiphase system (Kendal, 1950). In Monte Carlo methods, the evolution of each particle is tracked. The behavior of the continuous phase are represented deterministically as a continuous change of the internal-coordinate vector while the dispersed phase are represented by random events occurring with specific and prescribed probabilities. In order to obtain a realizable solution, the number of artificial realizations is very high, which could lead to unsustainable computational costs. Therefore, this group of method are often employed for validation of cases with simplified assumptions (Zucca et al., 2007).

The moment based methods are originally formulated based on the idea that the integration of the PBE in the space of the internal coordinates, leading to a set of equations that can be solved only for some lower-order moments (Hulburt & Katz, 1964). This group of methods become popular due to their low computational demand and easy implementation in fluid dynamics calculation. For realistic problems, however, it is only possible to formulate the governing equations for case with highly simplified closure models: constant aggregation and size-independent growth, and that breaking modeling is not possible. Therefore, a

particular method called Quadrature Method of Moments (QMOM) is proposed, in which the number density function is assumed to be a summation of some function centered on the zeros of orthogonal polynomials of a Gaussian Quadrature (McGraw, 1997). After the moment transformation, the quadrature approximation of the moments can be carried out through a specific algorithm, such as PD algorithm or the adaptive Wheeler algorithm (Marchisio, 2013). The QMOM provides an attractive and accurate alternative when the moments rather than an exact PSD are desired. Naturally, the information representing the exact shape of PSD is lost due to this integration procedure. Besides QMOM, there are several analogical approaches belong to the moment based methods. For example, the extended quadrature method of moment (EQMOM) can be adopted to deal with the growth issue in the evaporation and condensation technology (Yuan et al., 2012). Direct Quadrature Method of Moments (DQMOM) and Conditional Quadrature Method of Moments (CQMOM) can be employed to solve the multivariate problems (Marchisio & Fox, 2005; Yuan & Fox, 2011).

Classes method is a compromise between the Monte Carlo method and moment based methods in terms of computation time (Vanni, 2000), in which the continuous internal coordinate space is discretized in a finite number of discrete size classes or bins. This procedure transforms the PBEs from integro-partial differential equations (PDEs) into a coupled set of ordinary differential equations (ODEs). Consequently, the actual shape of PSD could be tracked by monitoring the number of elements belong to each class. Several approaches belonging to this group, such as discretization methods, the method of characteristics, the cell-average technique, the method of weight residuals, Lattice Boltzmann methods and the finite volume method, have been reviewed in the literature (Buffo & Alopaeus, 2016). The most popular numerical scheme belonging to the family of classes is the so-called fixed-pivot technique. It predicts the exact PSD by conserving two distribution moments (Kumar & Ramkrishna, 1996a, 1996b). The accurate solution of such low order approach, however, is only satisfied by adopting a large number of classes, which may be unacceptable when PBE is coupled with Computational Fluid Dynamics (CFD) simulations or when the PBE is used to formulate and test new sub-models. Therefore, the low order fixed-pivot approach is extended by conserving defined number of moments of the distribution, leading to the high-order moment method of classes (HMMC) (Alopaeus et al., 2006, 2007). Comparing to the traditional numerical methods, HMMC offers accurate solution with considerably lower number of classes, as well as tracks the actual shape of PSD directly. Moreover, this method is very flexible since it can preserve an arbitrary set of moments and consider a different number of internal variables of the population balance equation. For the gas-liquid system, it has been proved that 20 categories are enough to achieve a reasonable accuracy (Nauha & Alopaeus, 2013). For the solid-liquid system, such as crystallization or dissolution processes, a larger number of categories is required as solid has a wider size range.

The major issues of the numerical methods include the accuracy and computational load. For the moment-based method, the moments of PSD can be tracked by means of QMOM even in the multivariate calculation. This is desirable for empirical parameters fitting in Publication [I, II] and CFD-PBE coupling calculation in Publication [III]. However, the real shape of PSD is lost, which makes the strong coupling between the particle size and phase variable not possible. For the Monte Carlo and classes method, the accurate solution requires a large number of size categories of particles, which introduces equal number of equations to be solved. This procedure could considerably increase the computational cost when the CFD-PBE coupling calculation is performed for realistic chemical processes. In addition, optimization is often carried out at the final stage of simulation. Small errors brought from numerical methods could make deterministic optimization inefficient and unlikely to be successful during solving the population balance equations that are a set of complex and high non-linear equations. The nonlinearity of the PBE is caused by the agglomeration terms. For some special cases in which only nucleation, growth and breakage phenomena are considered, such as reactive dissolution or cooling crystallization, the PBE could have an analytical solution. Therefore, an analytical time stepping (ATS) technique should be developed and tested in the future.

3.2.1 HMMC

According to the principle of classes method, the internal coordinate space is discretized into a finite number of size classes (NC) and the number densities of particles (Y_i) belonging to each class is counted. By transforming relevant terms, such as nucleation, growth, agglomeration and break, into their discrete counterparts, the PBE for a closed system becomes the following (coupled) set of ordinary differential equations (Alopaeus et al., 2008):

$$\begin{aligned} \frac{dY_i}{dt} = & \sum_{j=1}^{NC} B(L_i, L_j) g(L_j) Y_j + \sum_{j=1}^{NC} \sum_{k=1}^{NC} \chi(L_i, L_j, L_k) F(L_j, L_k) Y_j Y_k \\ & - g(L_i) Y_i - Y_i \sum_{j=1}^{NC} F(L_i, L_j) Y_j + \sum_{j=1}^{NC} \xi(L_i, L_j) G(L_j) Y_j + \Omega(L_i) \end{aligned} \quad (3.2)$$

where i, j and k are the indices of particle size classes; Y_i is the particle number density of class i ; $B(L_i, L_j)$ is the breakage table, that determines the contribution of breakage event of particles in j -th class to particles number in i -th class; $\chi(L_i, L_j, L_k)$ is the agglomeration table, that describe the contribution of agglomeration event of particles in j -th and k -th class to particles number in i -th class; $\xi(L_i, L_j)$ is the growth table, that represents the contribution of growth event of particles in j -th class to particles number in i -th class; $\Omega(L_i)$ is the nucleation table. Compared with the typical fixed-pivot technique, HMMC can preserve an arbitrary number of mixed-order moments of the distribution. The terms referred as ‘tables’ are built to describe the contribution of the corresponding phenomena to the evolution of PSD, which depend only on the discretization used and remain the same during time

integration. In another words, the table construction can be carried out only once at the beginning, which significantly reduce the overall computational load.

3.2.2 QMOM

The quadrature method of moments (QMOM) is an extension of the standard moment method where the realistic closure problems are solved by a quadrature approximation. The moment transformation of number density function can be performed as:

$$m_k = \int_0^{\infty} n(L)L^k dL \quad (3.3)$$

Then the continuous NDF, $n(L)$, is presented as a quadrature approximation:

$$n(L) \approx \sum_{i=1}^{Nq} w_i \delta[L - L_i] \quad (3.4)$$

Therefore, the k -th moment, m_k , becomes:

$$m_k \approx \sum_{i=1}^{Nq} w_i L_i^k \quad (3.5)$$

where i is the index of quadrature node; w_i is the weight of i -th quadrature node.

In QMOM, the quadrature approximation of order Nq is defined by the abscissas (L_i) and weights (w_i) and can be specified from the its first $2Nq$ moments by writing the recursive relationship for the polynomials in terms of the moments m_k . Once this relationship is written in matrix form, the roots of such polynomials corresponding to the eigenvalues of the Jacobi matrix can be obtain by using product-difference (PD) algorithm (Gordon, 1968). Once L_i and w_i have been computed, any integral involving $n(L_i)$ can be approximated using Eq. (3.5). Finally, the PBE for a closed system becomes the following (coupled) set of ordinary differential equations (Marchisio et al., 2003):

$$\begin{aligned} \frac{dm_k}{dt} = & \sum_{i=1}^{Nq} w_i \int_0^{\infty} L^k g(L_i) \beta(L|L_i) dL + \frac{1}{2} \sum_{i=1}^{Nq} w_i \sum_{j=1}^{Nq} w_j (L_i^3 + L_j^3)^{k/3} F(L_i, L_j) \\ & - \sum_{i=1}^{Nq} w_i L_i^k g(L_i) - \sum_{i=1}^{Nq} L_i^k w_i \sum_{j=1}^{Nq} w_j F(L_i, L_j) + k \sum_{i=1}^{Nq} w_i L_i^{k-1} G(L_i) + L_0^k \Theta(L_0) \end{aligned} \quad (3.6)$$

3.3 Closure models

Several physical and chemical phenomena coexist in the multiphase reactive crystallization, such as interphase mass transfer, chemical reaction, crystallization and the behavior of dispersed phases. This process has several characteristics: (1) interphase mass transfer could be the rate limiting step compared to the chemical reaction; (2) the relatively high supersaturation caused by the chemical reaction leads to extremely fast primary nucleation and produces a large amount of crystals with small sizes; (3) the PSD of the final crystal product could be also influenced by the secondary processes, including agglomeration,

breakage and Ostwald ripening. Therefore, closure models coupled with population balance models are essential to properly describing the multiphase reactive crystallization.

3.3.1 Supersaturation

Formation of crystal P via charged ions A and B can be presented as:



The chemical potential of solute in the solid phase is equal to the liquid phase at equilibrium state. As the driving force of the crystallization, supersaturation can be thermodynamically expressed as the potential difference of solute in the solid phase and liquid phase as:

$$S = \phi - \phi^* = RT \ln(a / a^*) \quad (3.8)$$

In the dilute binary solution, S can be approximately calculated as (Dirksen & Ring, 1991):

$$S = \sqrt{c_A c_B} - \sqrt{K_{sp}} \quad (3.9)$$

where $*$ represents the solid-liquid equilibrium state; ϕ is the chemical potential; a is the activity of solute; c is the concentration of components in the liquid phase; K_{sp} is the solubility product of the new formed crystals. Several other expressions of the supersaturation have been reviewed in the literature (Mersmann, 2001).

3.3.2 Nucleation

The nucleation can be classified into primary homogeneous nucleation, primary heterogeneous nucleation and secondary nucleation. Homogeneous nucleation occurs in the absence of a solid interface while heterogeneous nucleation occurs in the presence of a solid interface of a foreign seed. Classical theory assumed that homogeneous nucleation is achieved by the aggregation of clusters with a critical size when the Gibbs free energy reaches the maximum value. In the region of relatively high supersaturation, the homogeneous nucleation rate, $J_{N,hom}$, can be written as an Arrhenius type of expression (Nielsen, 1964):

$$J_{N,hom} = A \exp\left(\frac{-\Delta G_{hom}}{kT}\right) \quad (3.10)$$

where A is the pre-exponential factor and has a theoretical value of 10^{30} nuclei/cm³; ΔG_{hom} is free Gibbs energy for the homogeneous nucleation. In practice, however, most primary nucleation are likely to be of heterogeneous type induced by other foreign surfaces. This requires a lower surface energy (ΔG_{het}) than that of a new solute particle and occurs at a

lower critical supersaturation. Then the total primary nucleation rate, J_N , can be simply expressed as:

$$J_N = J_{N,hom} + J_{N,het} \quad (3.11)$$

Once the suspension density increase to a certain level in the stirred tank reactor, the secondary nucleation could occur due to a large amount of nuclei produced by the crystal-crystal collisions and crystal-impeller collisions. The mechanism of secondary nucleation is complex and not well understood. In the stirred tank reactor, it is also difficult to distinguish one single nucleation mechanism from the other experimentally due to the turbulent flow. Therefore, the empirical powder law functions were proposed to calculated the nucleation rate (Nielsen, 1964):

$$J_{N,pr} = k_{n,pr} (S)^{n_1} \quad (\text{Primary nucleation}) \quad (3.12)$$

$$J_{N,se} = k_{n,se} N_s^a M_T^b (S)^{n_2} \quad (\text{Secondary nucleation}) \quad (3.13)$$

where $k_{n,pr}$ and $k_{n,se}$ are empirical nucleation constants for primary and secondary nucleation respectively; n_1 and n_2 are the exponents of supersaturation; N_s is the impeller speed; M_T is the suspension density; a and b are the case dependent adjustable parameters.

3.3.3 Growth

The crystal growth rate is determined by diffusion/convection and surface integration procedures. The diffusion/convection-controlled growth is mainly controlled by supersaturation and diffusion coefficient of the components, which is analogous to the film theory of mass transfer (Wilcox, 1993). When the diffusive/convective transport takes place rapidly, crystal growth is determined by the integration reaction occurring on the crystal surface. The mechanisms of the integration-controlled growth mainly include linear growth, two-dimensional growth and screw dislocation growth. Most of the theories are mathematically rather complex but helpful in understanding the nature of the crystal growth process. In addition, the experimental results of several authors indicated that the crystal growth of several substances is a function of crystal size or have a growth dispersion (Garside et al., 1974; Phillips and Epstein, 1974; Mitrovic et al., 1999). Then three major models including the growth diffusivity model (Randolph & White, 1977), the constant (or inherent) crystal growth model (Berglund & Larson, 1984) and the common history growth model (White et al., 1998) were proposed in order to interpret and describe these phenomena. It should be noted that the mentioned models were mostly built for pure growth problems. In another words, the influence of nucleation and flow field of reactors were not taken into account. For the reactive crystallization process in a stirred tank reactor, however, the final crystal sizes are largely dominated by the nucleation due to the fast chemical reaction and

the turbulent intensity caused by rotation of impeller. Therefore, a similar empirical power law function is proposed for the size independent crystal growth (Nielsen, 1964):

$$G = k_g (S)^g \quad (3.14)$$

where k_g is the empirical growth rate constant; g is the exponent of supersaturation.

For the bubbles and the dissolving solids in Publication [II] and [III], the grow rate of particles with size L_i were calculated directly from the corresponding mass transfer flux, $N(L_i)$:

$$G(L_i) = \frac{N(L_i)A(L_i)f_s}{3k_v L_i^2} \quad (3.15)$$

where $N(L_i)$ is mass transfer flux for particle with size L_i ; $A(L_i)$ is the particle surface area; k_v is the volume shape factor (equal to $\pi/6$ for spheres); f_s is the molar volume of solid.

3.3.4 Coalescence and Agglomeration

Coalescence of bubbles and agglomeration of crystals are generally considered complex because they involve not only the interactions of particles with the surrounding fluid, but also the interactions between fluid particles themselves once these particles are brought together due to the action of the external flow or body forces. It is also worthwhile mentioning that gas bubbles behave rather differently than solid particles because they are deformable, elastic, and may agglomerate or eventually coalesce after random collisions (Yeoh et al., 2014). Therefore, the bubble coalescence and crystal agglomeration are introduced individually.

3.3.4.1 Coalescence of bubbles

In the gas-liquid system, three mechanisms are commonly adopted to describe bubble coalescence: coalescence resulting from turbulent eddies, coalescence resulting from bubble with different rise velocities, and coalescence resulting from bubble wake entrainment. The coalescence rate can be presented as the product of collision frequency and coalescence efficiency.

In stirred tank, numerical tests here shown that the turbulence is the dominating driving force of bubbles coalescence. Turbulent collision frequencies are calculated by analogy with kinetics gas theory (Alopaeus et al, 1999; Prince & Blanch, 1990):

$$F_G(L_i, L_j) = c_{co} \cdot \varepsilon^{1/3} (L_i + L_j)^2 (L_i^{2/3} + L_j^{2/3})^{1/2} \quad (3.16)$$

where adjustable collision frequency constant, c_{co} , varies from 0.28 to 1.11 depending on the effective collision cross-sectional area and the expression for turbulent fluctuation velocities (Jakobsen et al., 2005). Coalescence efficiency, ψ_G , is described by film drainage theory. The coalescence only occurs when the bubble contact time exceeds the time required for drainage of the liquid film between bubbles to a critical rupture thickness (Chesters, 1991). Prince and Blanch (1990) developed a model based on the assumption that inertia of draining liquid (low viscosity) and the surface tension forces control the drainage of a fully mobile bubble surface:

$$\Psi_G(L_i, L_j) = \exp\left(-c_\psi \frac{\rho_L^{1/2} \varepsilon^{1/3}}{(1/L_i + 1/L_j)^{5/6} \sigma^{1/2}}\right) \quad (3.17)$$

where c_ψ is the adjustable parameter, which is of magnitude of 2.3, considering the initial and critical film thicknesses. The collision frequency and coalescence efficiency introduced above were adopted in Publication [III]. Besides the turbulence induced bubble coalescence, several models and modifications based on different mechanisms and experimental validations are available in the literatures (Fu & Ishii, 2003; Lehr et al., 2002; Wang et al., 2005).

3.3.4.2 Agglomeration of crystals

The crystal agglomeration often occurs along with primary nucleation and crystal growth under relatively high supersaturation during reactive crystallization. Besides the properties of surrounding solution, the crystals agglomeration depends on particle-particle and particle-fluid interactions, particle morphology and fluid mixing. Generally, three steps are needed to obtain agglomerates: (a) the collision of two particles, (b) a sufficient time interval during which the two particles stay together with the help of the flow, and (c) the adherence of the two particles caused by supersaturation. As with the bubble coalescence, the agglomeration rate can be analogously expressed as the production of collision frequency function and the collision efficiency. The collision frequency can be described by the Brownian kernel when the crystals are sufficiently small that they neither influence the fluid phase nor are disturbed by fluid shear (Von Smoluchowski, 1917):

$$F_s(L_i, L_j) = \frac{2k_B T}{3\mu} \frac{(L_i + L_j)^2}{L_i L_j} \quad (3.18)$$

where k_B is Boltzmann's constant; μ is the fluid dynamic viscosity; T is the absolute temperature. When particles are sufficiently large compared to shear gradients, collision frequencies are influenced by fluid motion. In the case of turbulent flow, the collision

frequency of the particles which are smaller than the eddies with Kolmogorov length scale can be calculated as (Adachi et al., 1994):

$$F_s(L_i, L_j) = 1.29 \left(\frac{\varepsilon}{\nu} \right)^{1/2} (L_i + L_j)^3 \quad (3.19)$$

where ε is the turbulent dissipation rate and ν is the kinematic viscosity. Both of these two collision kernels were considered in Publication [III].

The agglomeration efficiency, ψ_s , is initially governed by a variety of effect, such as attractive force (Van der Waals theory) and repulsive force (DLVO theory). This balance is significantly influenced by the ionic strength of the solution. Another major effect is due to hydrodynamics or viscous interaction, which tends to hinder the approach of colliding particles. For the reactive crystallization system, an important factor is the strength of 'bridge' formed in regions of high supersaturation (Hounslow et al., 2001). The agglomeration efficiency can be expressed as:

$$\psi_s = \frac{(\Gamma(\varepsilon)/\Gamma_{50})^\gamma}{1 + (\Gamma(\varepsilon)/\Gamma_{50})^\gamma} \quad (3.20)$$

The strength of aggregate, $\Gamma(\varepsilon)$, is a function of the energy dissipation, crystal size, apparent yield stress, density of particle, dynamic viscosity of liquid and the growth rate of crystal:

$$\Gamma(\varepsilon) = \frac{\alpha \mu^{1/2} G^2}{\rho_L^{3/2} d_{3,0}^2 \varepsilon^{3/2}} \quad (3.21)$$

where $d_{3,0}$ is the volume mean diameter, calculated as the ratio of the 3rd and 0-th order moment; Γ_{50} and γ are parameters fitted against experimental data.

3.3.5 Breakage

Similar to the coalescence or agglomeration of particles in turbulent flows, the breakage of particles in turbulent dispersions is significantly influenced by the continuous phase hydrodynamics and interfacial interactions. In another word, the breakage of bubbles and crystals is determined by the flow field and the characteristics of the particles themselves.

3.3.5.1 Breakage of bubbles

Bubble breakage depends on the balance between external stresses that tend to deform and break the bubbles and internal forces, such as viscous and interfacial forces, that restore their form. The turbulent fluctuation and the shear rate are commonly considered as reasons for instability on the gas-liquid interface. Narsimhan et al. (1979) proposed a model for

breakage of droplets in liquid-liquid system, based on the eddy arrival rate at the drop surface. They assumed that only eddies smaller than the droplets and with sufficient kinetic energy are able to result in a breakup event, whereas bigger eddies only contribute to their transport. Then, a model for bubble breakage frequency is proposed based on Narsimhan's theory (Lee et al., 1987):

$$g_G(L_i) = c_1 \varepsilon^{1/3} L_i^{2/3} \left[1 - \frac{1}{L_i} \int_0^{L_i} F \left(c_2 \frac{\sigma L^2}{\rho_L \varepsilon^{2/3} x^{11/3}} \right) dx \right] \quad (3.22)$$

where F represents the cumulative chi-squared distribution function with three degrees of freedom; c_1 and c_2 are two parameters to be obtained via fitting with experiments. It has been reported that viscous forces proportional to the viscosity of the liquid phase could contrast bubble breakup (Walter & Blanch, 1986). Therefore, the breakage model was extended by Laakkonen et al. (2006) as:

$$g_G(L_i) = c_1 \varepsilon^{1/3} \operatorname{erfc} \left(\sqrt{c_2 \frac{\sigma}{\rho_L \varepsilon^{2/3} L_i^{5/3}} + c_3 \frac{\mu_L}{\sqrt{\rho_L \rho_G \varepsilon^{1/3} L_i^{4/3}}}} \right) \quad (3.23)$$

where $\operatorname{erfc}()$ indicates the complementary error function. The fitting parameters, c_1 , c_2 and c_3 , were identified through an extensive experimental campaign on a gas-liquid stirred tank reactor (Laakkonen et al., 2006). In general, the breakage frequency was developed based on the empirical and phenomenological consideration. It can be used for different fluids and flow conditions, as the relevant properties of phases and the parameters of flow dynamics have been taken into account. This model has been implemented in the Publication [III]. In addition, Luo and Svendsen (1996) formulated a kernel for the binary bubble breakup that implicitly includes the distribution of the bubbles after breakage. Several well-known deficiencies of this model has been avoided either by considering capillary (Lehr et al., 2002) or kinetic energy density constrains (Hagesaether et al., 2002) or both of them (Wang et al., 2003). By reviewing and comparing the available bubble breakage models, Kostoglou and Karabelas (2005) found that various forms of breakage model were developed by several authors, which lead to great uncertainties of bubble beakage. Therefore, the scope of application and limitation of models should be carefully considered during the model development.

Together with the breakage frequency, the breakage pattern that specify the number and size of bubbles after breakage of mother bubble should be described by the daughter size distribution (DSD) function. Theoretically, the DSD function depends on the properties of phases, the size of mother bubbles and the local turbulence intensity. In reality, a bubble could divided into two (binary breakup) or several fragments with equal or unequal sizes, depending on the initial extent of active state and the gas redistribution mechanisms. In a

fully developed turbulence flow, binary breakup caused by local turbulent eddies is the most likely event in which the size of the daughter bubbles may be different.

Luo and Svendsen (1996) proposed a DSD function based on the theories of isotropic turbulence and probability:

$$\beta(f_v, L_i) = \int_{\zeta_{min}}^L P_b(f_v | L_i, \zeta) \varpi(L_i) d\zeta \quad (3.24)$$

where $P_b(f_v | L, \zeta)$ is the probability density that a bubble/droplet with size L_i breaks into two parts, one with volume fraction of f_v and the other with volume fraction of $(1-f_v)$; ζ is the size of turbulent eddy that collides with bubble of size L_i ; $\varpi(L_i)$ is the collision frequency of eddies of size between L_i and dL with bubble of size L_i . The major shortcoming of the Luo's model is that only the energy constraint is considered. To account for the capillary constrains, Lehr et al. (2002) formulated a daughter distribution function based on local fluid properties and turbulence intensity, as well as the size of the mother bubble (L_j):

$$\beta_v(L_i, L_j) = \begin{cases} \frac{6}{\pi^{3/2} L_i^3} \frac{\exp\left\{-\frac{9}{4} \left[\ln\left(2^{2/5} L_i \varepsilon^{2/5} (\rho_L / \sigma)^{3/5}\right)\right]^2\right\}}{1 + \operatorname{erf}\left\{\frac{3}{2} \ln\left(2^{1/15} \lambda \varepsilon^{2/5} (\rho_L / \sigma)^{3/5}\right)\right\}}, & 0 \leq L_i^3 \leq \frac{L_j^3}{2} \\ \beta_v(L_j - L_i, \lambda), & \frac{L_j^3}{2} \leq L_i^3 \leq L_j^3 \end{cases} \quad (3.25)$$

Then a more complicate breakup kernel function accounting both energy constraint and capillary pressure constraint was developed and validated by Wang et al. (2003, 2005) in a bubble column. In the stirred tank reactor, the local turbulent kinetic energy is extremely large near the impeller. Binary breakage is not always valid in such complex flow conditions. The experiments of Risso and Fabre (1998) proved that multi-breakage events are a major source of bubbles formed from breakage of larger bubbles in the turbulent flow field. Therefore, Laakkonen et al. (2007) proposed a DSD function based on the Beta probability density function:

$$\beta(L_i, L_j) = \frac{1}{2} (1 + c_\gamma)(2 + c_\gamma)(3 + c_\gamma)(4 + c_\gamma) \left(\frac{L_i^2}{L_j^3}\right) \left(\frac{L_i^3}{L_j^3}\right)^2 \left(1 - \frac{L_i^3}{L_j^3}\right)^{c_\gamma} \quad (3.26)$$

where c_γ is the adjustable parameter of beta distribution. The break event is binary when c_γ is 2.0. For the multi-fragments breakage, the c_γ can be obtained by parameter fitting against experimental data. It should be noticed that the construction of β table could produce small numerical error. Therefore, the table is further scaled for exact volume conservation. In

another word, the volume of mother particle must be conserved during the numerical integration of beta distribution:

$$\int_0^{L_i} \beta(L_i, L_j) L_i^3 dL = L_j^3 \quad (3.27)$$

The easy implementation and flexible application represent the major advantages of the Beta distribution in Publication [II]. This DSD function was successfully validated in the case of fully turbulent gas-liquid flow performed in a stirred tank (Laakkonen et al., 2006; Petitti et al., 2010).

3.3.5.2 Breakage of crystal agglomerates

In the reactive crystallization, the crystals sizes are commonly very small (under 10 μm) due to the relatively high supersaturation as mentioned previously.

Two mechanisms contribute to the breakage of agglomerates. The first one is normal stresses acting on surface of the particle while the second is disrupting stresses acting on a crystal agglomerate captured by two eddies acting on the opposite sides of the particle. The normal stresses could dominate the breakage when the size of the turbulence eddy is smaller than size of particle. When the size of turbulence eddy is larger than the size of particle, the breakage could be governed by the shear stress originating from different eddies with different turbulent velocities.

Particle breakage functions can be factored into two parts. The breakage frequency, $g(L_i)$, is the rate function for particle breakage, and daughter size distribution, $\beta(L_i|L_j)$, defines the probability that a fragment of size L_j is formed from the breakage of an L_i -sized particle. The expressions of particle breakage frequency for liquid-liquid and liquid-solid systems have been reviewed in the previous literature (Marchisio et al., 2003). The breakage rate can be written as a function of the aggregate strength (τ_f) when the detail information of the particle agglomerate is known (Ayazi Shamlou et al., 1994):

$$g_s(L_i) = \frac{1}{\sqrt{15}} \left(\frac{\varepsilon}{\nu_L} \right)^{1/2} \exp \left[- \frac{\tau_f}{\mu_L (\varepsilon / \nu_L)^{1/2}} \right] \quad (3.28)$$

where is a function of inter-particle force and the volume fraction of solid with the aggregate. In practice, however, it is impossible to obtain these varying parameters during the chemical process, such as crystallization in Publication [II] and reactive dissolution in Publication [III]. The widely applied breakage rate for particle agglomerates is based on a power law function including kinematic viscosity, turbulence dissipation, and agglomerate size (Kramer & Clark, 1999; Wójcik & Jones, 1998):

$$g_s(L_i) = c_{br} v^\alpha \varepsilon^\beta L_i^\gamma \quad (3.29)$$

where c_{br} is a dimensionless breakage constant; α , β and γ are empirical exponents. It is worth noting that the powers in this model are not independent due to dimensional consideration. Therefore, the breakage rate could be rewritten in terms of the size of the agglomerate, the Kolmogorov length scale (η), and Kolmogorov time scale (η_T). As a result, the breakage rate can be expressed as (Zhao et al., 2017):

$$g_s(L_i) = c_{br} \left(\frac{L_i}{\eta} \right)^\gamma \eta_T^{-1} \quad (3.30)$$

Together with the breakage frequency, also the daughter size distribution (DSD) function is needed to model the outcome of a breakage event. A variety of functional forms for the DSD functions, including uniform, erosion, parabolic, fixed mass ratio (1:4) and symmetric fragmentation has been proposed and validated through comparison with the experimental data in Publication [II]. Most of the DSD functions are proposed based on the breakage of single particle, droplet and bubbles (Luo & Svendsen, 1996; Zaccone et al., 2007). Kramer and Clark (1999) summarized the breakage mechanisms of particle agglomerates and proposed the model of breakage frequency. For the particle agglomerate, however, many factors such as the structure of the particle agglomerates, the strength of particle-particle bridges and the breakage pattern should be considered in the formulation of the DSD. Unfortunately, a comprehensive study on DSD functions for the breakage of particle agglomerates is not available in the literature. An empirical way adopted in this work to overcome this issue is to introduce a well-defined probability density function form with a limited number of parameters controlling the shape of the distribution and the number of the fragments generated by the breakage event, which can be fitted through comparison with the experiments. For this purpose, previously mentioned beta distribution is a suitable continuous probability distributions function, which is capable of empirically describing the breakage of particle agglomerates.

4. Flow dynamics

Simulation of reactive crystallization under ideal mixing assumption can be performed by solving the population balance model coupled with detailed chemistry. As previously mentioned, the crystallization kinetics are closely related to the physical properties and fluid dynamics characteristics. In fact, non-uniform distribution of the supersaturation caused by the non-ideal mixing condition frequently appears in industrial scale crystallizers. Nucleation could firstly happen in the region with higher supersaturation, such as evaporation interface, cooling surface and feeding area, which have a strong influence on the PSD of crystal products. Besides, the particle (bubbles and crystal) behaviors, such as coalescence/agglomeration and breakage, are strongly affected by local turbulent intensity near the impeller of stirred tank, especially in the gas-liquid reactive crystallization. As a typical rate-limiting step, mass transfer rate is determined by local mass transfer coefficient and mass transfer area. Therefore, the prediction of the local flow dynamics acts as a vital procedure in the simulation of reactive crystallization.

Computational fluid dynamics (CFD) presents a useful approach to predict the flow field that govern the crystallization rate and the physical properties of crystals in the solution. Kramer et al. (2000) predicted the distribution of supersaturation during evaporative and cooling crystallization in the forced circulation crystallizers. They indicated that only a part of the crystallizer volume is effectively used for the growth of crystals. Logashenko et al. (2006) coupled the population dynamics and the flow in the continuous stirred crystallizer to investigate crystal growth and breakage under different residence time. Sha et al. (2001) simulated size-dependent crystal classification under different mixing intensities, product removal locations and crystallizer geometries by means of CFD. By comparing results from CFD simulation and results calculated under the assumption of ideal mixing in various types of crystallizers: draft tube magma (DTM), double draft tube (DDT) and fluidized bed (FL), Plewik et al (2010) found a large deviation and underlined the importance of the CFD simulation. Wei and Garside (1997) first combined CFD calculation of turbulent flow field with reactive crystallization kinetics of barium sulfate in a liquid solution, investigating the influence of position and direction of feeding process on the PSD of the final products. Subsequently, the CFD-PBE became a popular approach to simulate the industrial-scale crystallizers. As regards the gas-liquid system, Rigopoulos and Jones (2001) tried to simulate a bubble column by coupling a very simplified multiphase CFD model with PBE

model for crystals. For bubbles, only monodisperse bubble distribution was assumed without considering bubble coalescence and breakage. For crystals, only nucleation and growth were considered. These assumptions may be not reasonable for stirred tank reactors, since the intensive breakage of bubbles and crystals near the impeller could considerably improve the gas-liquid mass transfer and crush the crystals into smaller pieces. However, performing a comprehensive model coupling the multiphase flow dynamics with a detailed gas-liquid crystallization could require a heavy computational resource. Therefore, compartmental model could act as an alternative approach to reduce the computational costs of the CFD simulation with a coarse-grained description of the fluid field.

Compartmental model is a trade-off between the ideal mixing assumption and CFD, which was firstly proposed by Partterson (1975) to describe the turbulent flow field. Zauner and Jones (2002) predicted the nucleation rate and evolution of particle size for a reactive crystallization with compartmental model. Kagoshima and Mann (2006) built a fluid mixing model to successfully simulate the PSD of BaSO₄ in an unbaffled stirred tank. Regarding the gas-liquid chemical adsorption, Rigopoulos and Jones (2003) developed a hybrid CFD framework to calculate the chemical absorption rate of CO₂ bubbles into alkali solution in the bubble column. Nauha and Alopaeus (2013) coupled the CFD simulation and algal growth model in a bubble column by using compartmental model. To introduce the modeling approach, we take the gas-liquid reactive crystallization of Ca(OH)₂(aq) – CO₂(G) in a stirred tank reactor as an example. The model combines the description of flow field with several sub-models, namely gas to liquid mass transfer, chemical reaction, crystallization processes and population balances for both gas and crystals in Figure. 4.1.

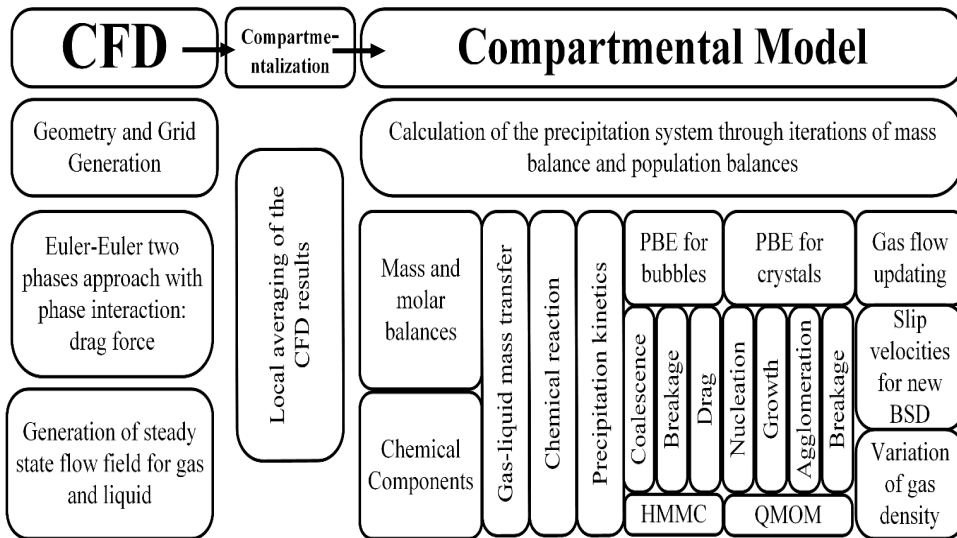


Figure 4.1 Flowchart of the compartmental model of gas-liquid crystallization.

4.1 Computational flow dynamics (CFD)

Compartmental model is carried out based on the realistic flow field calculated using CFD. The simulation domain of the stirred tank is divided into a number of computational cells (grid) with finite volume approach. A transient two-phase simulation of water and CO₂ is performed with the dispersed Eulerian multiphase model. The basic equations of flow motion, namely Navier-Stokes (N-S) equations, are solved numerically in each cell.

4.1.1 Basic two-fluid equation

The mass conservation equation:

$$\frac{\partial(\rho_p \varphi_p)}{\partial t} + \nabla \cdot (\rho_p \varphi_p \mathbf{u}_p) = 0 \quad (4.1)$$

The momentum conservation equation:

$$\frac{\partial(\rho_p \varphi_p \mathbf{u}_p)}{\partial t} + \nabla \cdot (\rho_p \varphi_p \mathbf{u}_p \mathbf{u}_p) = -\varphi_p \nabla P + \rho_p \varphi_p \mathbf{g}_p + \varphi_p \mu_p \nabla^2 \mathbf{u}_p + \mathbf{F}_p \quad (4.2)$$

where p is the index of phase (G and L); φ is the volume fraction, $\sum \varphi_p = 1$; \mathbf{u} is the vector of velocity; \mathbf{g} is the vector of gravity; μ_p is the shear viscosity; \mathbf{F} are the interfacial forces including drag forces, lift forces, turbulent dispersion forces and virtual mass forces.

4.1.2 Turbulence model

Several approaches are available for dealing with the turbulent flow, such as direct numerical simulation (DNS), large eddy simulation (LES) and Reynolds averaging N-S equations (RANS) (Ranade, 2001). DNS provide the most exact approach that requires resolving the smallest eddies and represents the turbulent mixing accurately. Such mechanism, however, needs extremely expensive computation. In LES, the turbulent flow consisted of eddies with a wide spectrum of scales, in which large eddies are resolved directly while the small eddies are modeled. LES modes are also three-dimensional and time-dependent but much less costly than DNS. In RANS, the instantaneous N-S equations are decomposed into time-averaged and fluctuating components. It is not necessary to resolve all the small scale eddies since the variation of time-averaged quantities occurs at much larger scales. Therefore, RANS requests much less computing resources than LES or DNS and presents the most widely used method for engineering simulation. RANS-based turbulence models can be grouped into two categories: the Reynolds stress modes (RSMs) and the eddy-viscosity models. For general-purpose flow simulation, the most frequently used two equation eddy-viscosity models, including Standard k - ε model, renormalization group k - ε (RNG) model, realizable k - ε model and k - ω model, are based on the assumption that an analogy exists

between Reynolds stress and viscous stress and the turbulent flow is isotropic. The comparisons between different turbulent models and their limitations have been widely discussed in the literature (Yakhot and Orszag, 1986; Ranade, 2001; Sajjadi et al., 2012). It is desirable to use the realizable k - ϵ turbulence model to predict the turbulent intensity in the agitated (Buffo & Marchisio, 2014).

4.1.3 Interphase forces

Theoretically, the interphase forces between the gas and liquid phase include drag force, lift force, virtual mass force and turbulent dispersion force. In aerated stirred tank, however, the effects of virtual mass and turbulent dispersion are almost negligible compared to the drag force. Scargiali et al. (2007) have reported an increase of overall gas holdup from 4.36 % to 4.67 % and from 4.36 % to 4.60 % by considering the effect of lift force and virtual mass respectively. Ashraf Ali and Pushpavanam (2011) found that the drag force are mainly responsible for lateral migrations of bubbles and distribution of gas volume fraction in the reactor. In addition, McClure et al. (2014) found that the lift force is important for smaller bubbles near the impeller. Therefore, only lift and drag force are involved by the Tomiyama correlation in this study (Tomiyama et al., 1998).

4.2 Compartmentalization

To begin with the compartmentalization, the time averaged cells values (pressure, volume fraction, turbulence dissipation, etc.) were simply calculated. These intermediate values are stored in user-defined memory locations for cells. The flows between cells, however, could not be averaged and saved for later retrieve by the algorithm termed compartmentalization. In order to calculate the volume flows between compartments, the division of flow domain into compartments should be carried out before the time averaging calculation. Noting that the flows between compartments are considered two way flows. In the stirred tank reactor, the radial mixing is prevailing due to the rotation of impeller. The radial flows would possibly eliminate each other and produce a zero result if the flow between compartments was considered one way (Nauha & Alopaeus, 2015).

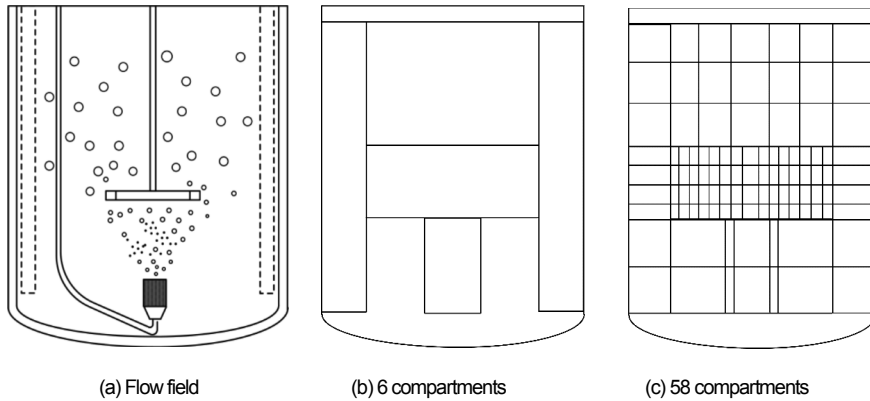


Fig. 4.2 Schematic diagram of the compartmentalization of the stirred tank reactor

Compartmentalization (division of compartments) can be performed automatically or manually. Automatic compartmentalization refers to a procedure capable of automatically defining a suitable network of zones after scanning the information in all of the cells according to a certain division criteria (Bezzo et al., 2003; Bezzo & Macchietto, 2004). The main advantages of this procedure include: (1) a quick and reliable definition of a network of zones; (2) the possibility of increasing the model resolution without major time expenditure during the model definition; (3) the ease of re-defining and adjusting previous zone models. However, the number of compartments could vary under different operating conditions, since it is only determined by the division criteria. It is difficult to compare the simulation results in this way. In addition, a large number of compartments coupled with a full population balance model could significantly reduce the calculation speed. Moreover, the shape of compartment could vary by collecting the cells that satisfy the division criteria. Thus, it is possible to miss some cells during automatic compartmentalization, making debugging process rather time consuming. In fact, the steady state flow fields in such stirred tanks are quite predictable, making manual compartmentalization possible. This division can be decided through observation of the gas-liquid flow pattern (Laakkonen et al., 2006). For the gas-liquid crystallization, the local gas-liquid mass transfer could dominate the overall reaction rate. On one hand, gas volume fraction in the feeding area could be larger than the tank averaged value, which could lead to higher mass transfer rate. On the other hand, turbulence energy dissipation in the vicinity of impeller could be much higher than other zones in the agitated vessel. Several variables, such as mass transfer coefficient, coalescence and breakage rates for the gas bubbles, aggregation and breakage rates for the crystals, are governed by the local turbulent intensity. Therefore, the spatial distribution of energy dissipation and gas volume fraction are chosen to be references to subdivide the flow field into different regions: feeding zone, stirring zone, baffle zone, suspension zone, and degassing zone in Fig. 4.2. Then the number/size independence study was performed by simulate the gas-liquid crystallization with an increasing number of compartments from 6

to 85, which indicates that a division of 58 compartments is enough to achieve a number/size independent simulation.

4.3 Compartmental model

Compartmental models have been broadly adopted to study the local multiphase hydrodynamics in agitated vessels (Vasconcelos et al., 1995; Vlaev et al., 2002; Laakkonen et al., 2007). In this work, the flow fields captured from the previous CFD simulation are coupled with gas-liquid crystallization models, including gas-liquid mass transfer, chemical reaction, crystallization kinetics and PBEs for bubbles and crystals, by means of the compartmental model.

The compartmental model mainly solve the dynamic mass, scalar and population balances for every compartment. The liquid flow rates crossing the compartment interface are taken directly from the previous CFD simulation of gas-liquid flow and assumed constant. The bubble flow rates are calculated based on the bubble velocities that are summation of liquid velocities and slip velocities. In the CFD-PBE simulation, slip velocities of dispersed phase are commonly calculated from the Sauter Mean Diameter (d_{32}). In compartmental model, slip velocity of each bubble size category is considered by solving population balance equations (PBEs). HMMC is adopted to solve PBEs of bubbles to achieve a good compromise between computational load and accuracy. In order to save the computational resource, QMOM was used to solve the PBEs of crystals. In addition, physical properties, such as average density, viscosity and volume fraction of each phase are updated constantly during the simulation. The heat balances are not involved, since the gas-liquid reactive crystallization is performed at ambient temperature and pressure.

4.3.1 Governing equations

4.3.3.1 Mass balance

For compartment i , the mass balance equation for each liquid component can be expressed as:

$$\frac{dn_{L,i}}{dt} = \sum_{j=1}^{NB} c_{L,j} F_{L,j,i} - c_{L,i} \sum_{j=1}^{NB} F_{L,i,j} + N_{GL,i} a_{GL,i} V_{L,i} + r_i V_{L,i} \quad (4.3)$$

where i and j are the indexes of compartments; NB is the total number of compartments; in and out represent the indexes of feeding and degassing compartment respectively; F is the flow rate; N is the gas-liquid mass transfer fluxes; a is the mass transfer area; r is the chemical reaction rate; V is the volume of liquid phase. Terms on the right hand side are: (1) internal liquid flow in, (2) internal liquid flow out, (3) mass transfer rate and (4) reaction rate.

The mass balance equation for each chemical specie of gas phase in compartment i is calculated as follow:

$$\begin{aligned} \frac{dn_{Gj}}{dt} = & c_{G,in}F_{G,in} - c_{G,out}A_{out} \sum_{p=1}^{NC} v_p U_{p,slip,out} Y_{p,out} \\ & + \sum_{j=1}^{NB} \left[c_{G,j} A_{ij} \varphi_j \sum_{p=1}^{NC} v_p U_{p,j,i} Y_{p,j} \right] - c_{G,i} \sum_{i=1}^{NB} \left[A_{ij} \varphi_i \sum_{p=1}^{NC} v_p U_{p,i,j} Y_{p,i} \right] - N_{GL,i} a_{GL,i} V_{L,i} \end{aligned} \quad (4.4)$$

where p is the index of bubble size category; slip represent the index of slip velocity; A is the area between compartments; v_p is the volume of single bubble in the p -th size category; U is the velocity of gas phase; φ is the volume fraction of gas phase; Y is the particle density of bubbles. Terms on the right hand side are: (1) Gas feed, (2) Gas outlet, (3) internal gas flow in, (4) internal gas flow out and (5) mass transfer rate.

The mass balance of solid phase can be represented directly by the population balance of crystals, since there is no inflow and outflow for the liquid phase and solid phase in the semi-batch operation in this work.

4.3.1.2 Population balance

The reference volume of the variable (particle density for bubbles and moment for crystals) in PBEs is the dispersion volume:

$$V_{disp} = V_L + V_G \quad (4.5)$$

The liquid volume, V_L , is assumed constant. However, the gas volume, V_G , is allowed to change slightly since the terminal velocities of bubbles recalculated from real bubble size distribution could cause variation of gas volume fraction.

The discrete version of PBE for the bubbles can be written as:

$$\begin{aligned} \frac{\partial Y_{pj}}{\partial t} = & \frac{I}{V_{disp,in}} F_{G,in} Y_{p,in} - \frac{I}{V_{disp,out}} U_{p,slip,out} A_{out} Y_{p,out} + \frac{I}{V_{disp,j}} \sum_{j=1}^{NB} U_{p,j,i} A_{ij} \varphi_j Y_{p,j} - \frac{Y_{pj}}{V_{disp,i}} \sum_{i=1}^{NB} U_{p,i,j} A_{ij} \varphi_i \\ & + G_{p,i} + B_{p,i}^{cl} + B_{p,i}^{br} - D_{p,i}^{cl} - D_{p,i}^{br} \end{aligned} \quad (4.6)$$

where G is the growth term of bubbles; B and D is the birth and death term calculated from the coalescence (cl) and breakage (br) of bubbles. Terms on the right hand side are: (1) Gas feed, (2) Gas outlet, (3) internal gas flow in, (4) internal gas flow out, (5) growth due to the mass transfer and varying pressure, (6) birth due to coalescence, (7) birth due to breakage, (8) death due to coalescence and (9) death due to breakage.

After performing the moment transformation, the PBE for the crystals becomes:

$$\frac{\partial m_{k,i}}{\partial t} = \frac{I}{V_{dispj}} \sum_{j=1}^{NB} m_{k,j} F_{dispji} - \frac{I}{V_{dispi}} m_{k,i} \sum_{j=1}^{NB} F_{dispij} + G_{k,i} + J_{k,i} + B_{k,i}^{ag} + B_{k,i}^{br} - D_{k,i}^{ag} - D_{k,i}^{br} \quad (4.7)$$

Terms on the right hand side are: (1) internal crystals flow in, (2) internal crystals flow out, (3) growth term, (4) nucleation term, (5) birth due to agglomeration, (6) birth due to breakage, (7) death due to agglomeration and (8) death due to breakage. The Wheeler algorithm is used to calculate the quadrature approximation from the set of the transported moments.

In order to solve the balance equations from Eq. (4.3) to Eq. (4.7), several sub-models are needed, including the internal flows between compartments, interphase forces between bubble and liquid, the physical properties of dispersion and the closures models for the PBEs.

4.3.2 Flows between compartments

As mentioned earlier, the flows between compartments need to be calculated based on the previous CFD results. Two algorithms are available in the literatures. Laakkonen et al. (2007) directly derived the liquid flows from the results of one phase CFD simulation and assumed that the bubbles follows the liquid flow field with addition of slip velocity. The slip velocity is calculated by Newton-Raphson iteration of the force balance on a bubble, including the gravity, buoyancy and drag force. It is worth noting that the liquid flow are assumed bi-directional at the interfaces between compartments, which improve the accuracy of flow field prediction. The rise of bubbles due to slip causes a backward liquid flow of equivalent volume, namely bubble induced flow. The consideration of bubble induced flow ensures that relative volume of compartments remain unchanged. For the gas-liquid reactive crystallization, however, the flow rate correction from one phase CFD calculation could increase the computational cost, especially coupling with population balance equation. In addition, this assumption is not correct in the case that liquid flow is caused by the gas flow, such as bubble columns or suspension area in the stirred tank reactor. In Publication [III], an extended algorithm proposed by Nauha and Alopaeus (2015) to estimate the liquid flow and gas flow from results of two phase CFD simulation was adopted. Firstly, the gas flow rate and bubble velocity are taken from the CFD simulation as initial values. Then, the difference between slip velocities calculated from exact bubble size distribution and Sauter

Mean Diameter is estimated. Finally, this diameter is utilized to correct the initial bubble velocity and gas flow rate in compartmental model.

4.3.3 Closure models

Several variables, such as slip velocity, bubble growth rate and correction of energy dissipation rate are still needed to solve these balance equation. In addition, the gas-liquid mass transfer fluxes has been introduced in Chapter 2. Nucleation, growth, agglomeration and breakage terms in the PBE of crystal and coalescence and breakage terms in the PBE of bubbles have been presented in Chapter 3.

4.3.3.1 Slip velocity

The force balance (gravity, buoyancy and drag forces) on a bubble in size category p can be written as:

$$v_p (\rho_G - \rho_L) g = \frac{1}{2} a_{p,h} C_{p,D} \rho_L \bar{U}_{p,slip} |\bar{U}_{p,slip}| \quad (4.8)$$

where a_h is the projected area of bubble in the direction of flow; C_D is the drag force coefficient. Bubble slip velocities can be obtained by calculating Eq. (4.8) with Newton-Raphson iteration. Several empirical correlations have been developed for the calculation of drag coefficient in a gas-liquid system (Clift et al., 1978; Ishii & Zuber, 1979; Morsi & Alexander, 1972; Schiller & Naumann, 1933; Akio Tomiyama et al., 1998). Most correlations are valid for individual bubbles rising in stagnant liquid. Meanwhile, swarm and turbulence effects are known to have effect on drag force. However, the measurement of these effects in a stirred tank is difficult due to the intensive coalescence and breakage of bubbles in the feeding and stirring region. According to the previous experimental validation (Laakkonen, Moilanen, Alopaeus, & Aittamaa, 2007), the Tomiyama correlation for isolated bubbles in slightly contaminated Newtonian liquids was adopted in this work (Akio Tomiyama et al., 1998):

$$C_D = \max \left(\min \left(\frac{24}{Re} (1 + 0.15 Re^{0.687}), \frac{72}{Re} \right), \frac{8}{3} \frac{Eo}{Eo + 4} \right) \quad (4.9)$$

where Eo is the Eötvös number that determines the shape of bubbles:

$$Eo = \frac{g(\rho_G - \rho_L)L_p^2}{\sigma} \quad (4.10)$$

4.3.3.2 Volumetric bubble growth rate

The bubble grow term is commonly driven by gas-liquid mass transfer and hydrostatic pressure. Therefore, growth term, $G_{p,i}$, are obtained from:

$$G_{p,i} = \sum_{q=1}^{NC} \xi(v_p, v_q) B_{q,i} Y_{q,i} \quad (4.11)$$

where p and q are the index of bubble size category; $\xi(v_p, v_q)$ is volumetric growth table; $B_{q,i}$ is volumetric growth rate of bubbles of category q in compartment i (Laakkonen, 2006):

$$B_{q,i} = -a_q \sum_{p=1}^{NC} N_{GL,p,i} f_{G,p,i} + \sum_{j=1}^{NB} \left(1 - \frac{f_{G,j}}{f_{G,i}} \right) U_{q,j,i} A_{j,i} Y_{q,j} v_q \quad (4.12)$$

where a_q is the surface area of bubble of category q ; $N_{GL,p,i}$ is the gas-liquid mass transfer flux of bubble of category p in compartment i ; $f_{G,p,j}$ is the partial molar volume of bubbles of component p in compartment i . The first term on right hand side of Eq. (4.12) is growth due to gas-liquid mass transfer while the second term considers the effect of pressure variation, when bubble moves from a compartment to another. In stirred tank (3L) adopted in Publication [III], the influence of hydrostatic press can be neglected since press difference between compartments is very small in a lab scale stirrer. It is worth mentioning that hydrostatic press should be taken into account during the simulation in a bubble column or reactor scale-up.

4.3.3.3 Correction of local energy dissipation rate

Breakage, agglomeration and coalescence rates of bubbles and crystals, slip velocities and mass transfer fluxes are mainly governed by local turbulence energy dissipation rate (ε_{mix}). Therefore, ε_{mix} each compartment should be defined locally from the overall value obtained from the CFD simulation. However, it is worth noting that the k - ε turbulent model, or more in general on RANS models, which are known to underestimate the total turbulent energy dissipation(Montante et al., 2001; Li et al., 2016). In this case, it is desirable to first scale the average energy dissipation rate (ε_{ave}) to match the realistic value. Then ε_{ave} can be distributed to different compartment by means of relative dissipation factor to obtain local turbulence energy dissipation rate ($\varepsilon_{mix,i}$). Estimation of ε_{ave} from Torque moment, M , is known as a feasible way to give better prediction without adopting extremely fine grids (Li et al., 2016). Therefore, ε_{ave} is calculated as:

$$\varepsilon_{ave} = \frac{2\pi N_s |M|}{\rho_L V_L} \quad (4.13)$$

Then the local dissipation rate can be defined by the relative dissipation factor, ϑ_i :

$$\vartheta_i = \frac{\varepsilon_{CFD,i}}{\sum_{i=1}^{NB} \varepsilon_{CFD,i} w_i} \quad (4.14)$$

$$\varepsilon_{mix,i} = \vartheta_i \varepsilon_{ave} \quad (4.15)$$

where $\varepsilon_{CFD,i}$ is the local average energy dissipation calculated from CFD simulation; w_i is mass fraction of liquid in compartment i of the total mass of liquid. The scaling ensures that the mass integral of local dissipation is equal to the overall power consumption.

In regions with high gas hold up, influence of gas feeding and buoyancy on local energy dissipation rate should be taken into account. Finally, local dissipation rates are calculated by summing turbulence energy inputs due to mixing, buoyancy and kinetic energy of gas injection:

$$\varepsilon_i = \varepsilon_{mix,i} + \frac{\sum_{p=1}^{NC} Y_{p,i} |F_{p,drag,i}| U_{p,slip,i}}{\rho_{L,i} (1 - a_{G,i})} + \frac{F_{G,in} \rho_{G,i} U_{G,in}^2}{2V_{L,i} \rho_{L,i}} \quad (4.16)$$

4.4.4 Advantages and limitations of compartmental model

Two assumptions are commonly made in the CFD-PBE simulation: (1) the gas phase is incompressible and (2) the drag force of all bubbles is calculated based on d_{32} . Therefore, the bubble growth rate will not be affected by the local pressure. Bubbles with different sizes share the same slip velocity. These two limitations can be addressed in the compartmental model. The density of the gas phase is allowed to update with the local pressure in the system. Consequently, the influence of pressure differences is considered in the calculation of growth term in Eq. (4.12). In addition, the bubbles with different sizes are allowed to rise at different velocities since the slip velocity of each size category is obtained by solving the force balance equation with Newton-Raphson iteration. In this way, instead of the fixed gas volume flow in CFD simulation, gas volume flows from compartment to compartment are allowed to be updated with modifications of slip velocity and gas hold up in different batch operations. It is desirable to perform the time-consuming operations, including parameter fitting or process optimization, with compartmental model due to its low computational load compared to a full CFD simulation. In addition, it is also possible to directly scale up the reactor with compartmental model. By appropriate division of the fluid domain, compartmental model can be used to model gas-liquid reactor of different geometries without repeating CFD simulation. This is highly preferable in scale-up and in the cases where the product property demand or the geometries are changed.

Meanwhile, compartmental model still has several limitations: (1) accuracy of compartmental model significantly relies on the flow field captured by the previous CFD simulation; (2) test of compartments independence is always needed; (3) extreme values of important variables such as energy dissipation rate, gas hold up and concentration of components could vanish due to the averaging calculation in the compartmentalization.

5.Applications of mass transfer, population balance and compartmental model

The general formulations of mass transfer model, population balance model and the flow dynamics model for the reactive crystallization have been introduced in the previous chapters. The detailed applications involved in the related publications will be presented. Publication [I] proposed a mathematical model for reactive crystallization of magnesium carbonate with carbon dioxide from the magnesium hydroxide slurry in a stirred tank reactor. It is a very complex system, including dissolution of solid particle, absorption of gas bubble and formation of crystals. To simplify the mathematical description, assumption of ideal mixing and monodisperse bubble and crystal distribution were made. In addition, the breakage, coalesce and agglomeration of crystals and bubbles were neglected. The simulation results were found to be very sensitive to different operating conditions. A large deviation existed between experimental measurements and modeling results. In order to understand such complicated multiphase reaction, separate studies of reactive dissolution and gas-liquid crystallization were carried out in following publications. Publication [II] investigated the influence of particle breakage on overall dissolution rate and evolution of particle size distribution by using population balance model. Publication [III] studied the effect of fluid dynamics on gas-liquid reactive crystallization by means of compartmental model. As mentioned earlier, compartmental model is a compromise between the CFD-PBE simulation with detailed physical model and simulation under ideal-mixing assumption. The heavy computational load of CFD-PBE simulation can be attributed to the integration of N-S equations and PBEs. Publication [IV] investigated the influence of microwave field on the reactive crystallization of MgCO_3 . In order to validate models introduced previously, isolated experimental validations were also carried out. The experimental equipment and methods will be discussed along with the related applications in this chapter.

5.1 Experimental equipment

Experimental set up (Fig. 5.1) consists of a jacked glass reactor of 3L capacity equipped with an impeller, a sparger, a thermostat (Lauda T2200), a pH meter (Metrohm 744), and a calibrated CO_2 flow meter (Kytola LH-LB18-HR). The internal diameter of the crystallizer is 150 mm and its height is 200 mm. A 50 mm diameter Rushton turbine with six blades is used as the impeller. In order to improve mixing and prevent vortex formation, four baffles

are located symmetrically at the inner wall of the reactor. Several equipment were adopted to analyze the samples taken during the experiment. Concentration of components in the liquid phase was measured by ion chromatography (IC, ICS-1100). The particle size distribution (PSD) of the crystal was measured by Beckman Coulter LS 13320 laser diffraction analyzer after filtration. The morphologies and surface features of the dried crystals were photographed with a scanning electronic microscope (SEM, JEOL JSM-5800). In addition, the mass fraction of component in the solid mixture was analyzed by using thermal measurements, thermogravimetry (TG) and differential scanning calorimetry (DSC). The experimental set up and measurement technique were adopted during validations of the models in Publications [I-III] together with Lappeenranta University and Technology.

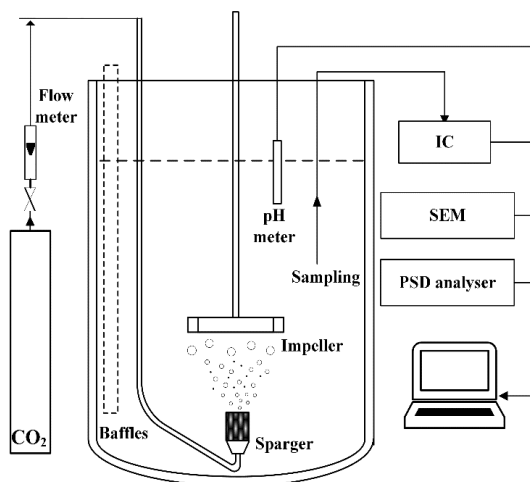


Figure 5.1 Scheme of experimental setup

5.2 Modelling of mass transfer, reaction and crystallization in gas-solid-liquid system

5.2.1 Introduction

A mathematical model was proposed in Publication [I] to describe a reactive crystallization of MgCO_3 in a heterogeneous stirred tank reactor. The model includes dissolution of $\text{Mg}(\text{OH})_2$, absorption of CO_2 and crystallization of MgCO_3 . The electroneutrality was maintained by modifying the dissolution model with Nernst-Planck equation. Two-film theory was adopted for solid-liquid mass transfer of dissolution and gas-liquid mass transfer of absorption. However, chemical reactions occur in the liquid film adjacent to surface of solid or gas bubble could enhance interphase mass transfer (Sada & Kumazawa, 1973; Salmi et al., 2011). A test of one dimensional diffusion-reaction model was performed with real

physical boundary to confirm this enhancement effect. Then, van Krevelen–Hoftijzer expression was adopted to quantitatively evaluate the enhancement effect of chemical reaction between dissolved CO₂ and OH⁻ on rate of dissolution and absorption. Population balance equation was solved by a moment method to predict the evolution of particle size during the dissolution and crystallization process. The unknown parameters, including nucleation rate constant, growth rate constant and exponents of supersaturation in Eq. (3.12) and Eq. (3.14) were fitted against evolution of components concentration in the liquid phase and pH of the solution measured at different operating conditions. The fitted parameters has been reported in Publication [I].

5.2.2 Experimental validation

The experimental results of the investigated system have been reported in the literature (Han et al., 2014a, 2014b). In each batch operation, 100 g of Mg(OH)₂ and 2.5 L of deionized water were first mixed in a stirred crystallizer. The Sauter Mean Diameter of particle sample is 26.4 μm. When the temperature of the Mg(OH)₂ slurry achieved the target temperature of 25 °C, pure CO₂ (purity 99.7%, AGA) was introduced through a metal pipe with a porous sparger from the bottom of the crystallizer. The flow rate of CO₂ was controlled by a calibrated CO₂ flow meter. A pH meter (Metrohm 744) was used to monitor in situ the pH of the reaction system during the crystallization process. Slurry samples were taken at different times during the experiments. CO₂ flow was stopped when the pH of the suspension approached a constant value. All samples were filtered immediately after sampling, and crystals were dried at room temperature in order to avoid any change of the solid form or the composition of the samples that might be induced by high temperature drying. To validate the proposed model, the batch operation was carried out under operating conditions in Table 5.1.

Table 5.1 Operating conditions

Exp	<i>N</i> , rpm	<i>Q_G</i> , m ³ ·s ⁻¹
1	560	1.67×10 ⁻⁵
2	560	1.50×10 ⁻⁴
3	650	1.67×10 ⁻⁵

5.2.3 Results and discussion

5.2.3.1 Parameter fitting

The unknown crystallization parameters were fitted against measurement results at different operating conditions and shown in Table 5.2. It is worth noting that, the nucleation constant (*k_n*) is sensitive to the geometry and mixing conditions in the stirred tank reactor (Myerson, 2001). Therefore, *k_n* should be fitted separately for different operating conditions.

Table 5.2 Parameter fitting results of crystallization kinetics (95%)

Parameter	Value	Unit
k_n (Case 1)	$(9.73 \pm 0.06) \times 10^6$	$\text{mol}^{-n} \cdot \text{m}^{(3n-3)} \cdot \text{s}^{-1}$
k_n (Case 2)	$(5.69 \pm 0.03) \times 10^7$	$\text{mol}^{-n} \cdot \text{m}^{(3n-3)} \cdot \text{s}^{-1}$
k_n (Case 3)	$(3.37 \pm 0.04) \times 10^7$	$\text{mol}^{-n} \cdot \text{m}^{(3n-3)} \cdot \text{s}^{-1}$
k_g	$(1.02 \pm 0.05) \times 10^{-10}$	$\text{mol}^{-g} \cdot \text{m}^{(3g+1)} \cdot \text{s}^{-1}$
n	(1.11 ± 0.04)	dimensionless
g	(1.29 ± 0.09)	dimensionless

5.2.3.2 The influence of impeller speed (N) and gas flow rate (Q_G)

The evolution of magnesium concentration ($[\text{Mg}^{2+}]$), mass fraction of $\text{Mg}(\text{OH})_2$ and MgCO_3 in the solid mixture are shown in Fig. 5.2. Three distinctive periods can be found: 1) Induction period, 2) Growth period, and 3) Equilibrium period. In the induction period, nucleation is introduced under relatively high supersaturation. $[\text{Mg}^{2+}]$ increases gradually at the beginning and tends to decrease after a peak value. However, the MgCO_3 crystals cannot be detected due to the small size of nucleus. In the growth period, $[\text{Mg}^{2+}]$ decreases quickly due to the high supersaturation and the following growth of nucleus after reaching a critical level. Meanwhile, MgCO_3 begins to accumulate during the growth period. In the equilibrium period, supersaturation produced by the magnesium and carbonate ions is not adequate for further crystal growth. Therefore, $[\text{Mg}^{2+}]$ tends to remain at a relatively high value. After comparing experimental and modelling results under different operating conditions, it turns out that higher impeller speed and gas flow rate can significantly improve the dissolution and crystallization rate. The higher impeller speed results in an increase of average turbulent intensity in the agitated vessel. Consequently, the higher mass transfer coefficient in proportion to the turbulent intensity accelerates overall rate of dissolution and absorption. Meanwhile, the higher impeller speed and gas flow rate can also improve the breakage of bubbles and increase the mass transfer area. It is interesting to note that the dissolution rate tends to slow down during the crystal growth period in Fig. 5.2 (b). According to the experimental observation, almost no gas exists under the gas sparger in the tank. Therefore, the local supersaturation could be different from the average value calculated by the model.

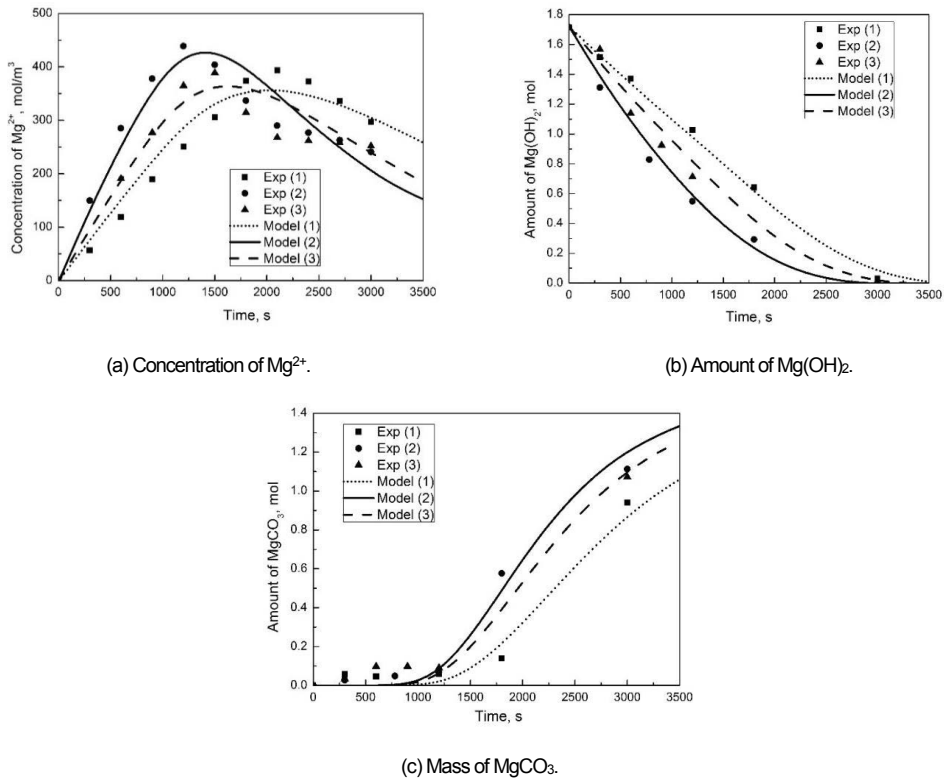


Figure 5.2 Modeling vs experimental results from Han et al. (2014b)

5.2.3.3 The effect of pH and enhancement factor (E)

The experimental and modeling results of pH are presented in Fig. 5.3(a). pH decreases quickly at the first few seconds and then drops gradually. As a key parameter, pH dominates the composition of the CO_2 - H_2O equilibrium system. Evolution of $[Mg^{2+}]$, $[CO_3^{2-}]$ and supersaturation are shown in Fig. 5.3(b). $[CO_3^{2-}]$ begins to reduce when pH is lower than 8.5 and remains at relatively low value at the end of crystallization. Even though the $[Mg^{2+}]$ still remains at a high level at the end of crystallization, a low value of $[CO_3^{2-}]$ can significantly decrease the supersaturation since it is defined as a product of $[Mg^{2+}]$ and $[CO_3^{2-}]$. As a result, nucleation and growth of crystal tends to slow down due to the decreasing supersaturation. Therefore, $[Mg^{2+}]$ remains at relatively high value even under further introduction of carbon dioxide. In addition, the pH is one of the reasons that lead to nucleation in the electrolyte solution.

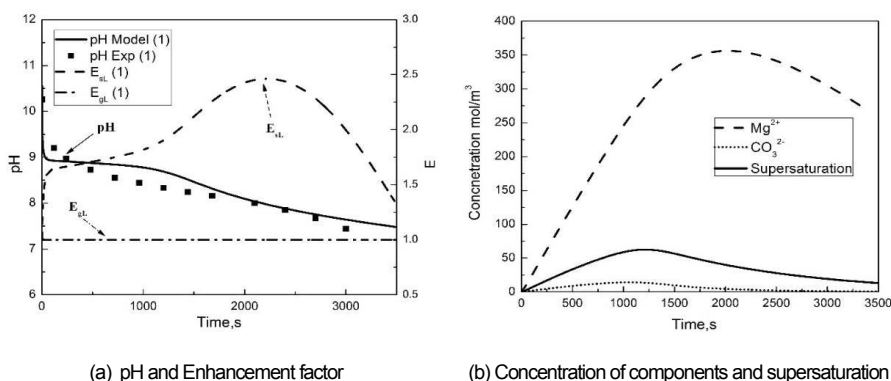


Figure 5.3. pH, enhancement factor and supersaturation

The enhancement factors for solid-liquid mass transfer (E_{sl}) and gas-liquid mass transfer (E_{gl}) are shown in Fig. 5.3(a). E_{sl} and E_{gl} are mainly determined by the concentration of components in bulk solution and the thickness of the liquid film near the surfaces of solids and bubbles. The enhancement factor of the solid-liquid mass transfer, E_{sl} increases at first 2300s of crystallization. This is because film reaction between $\text{CO}_2(\text{aq})$ and OH^- improve the mass transfer near the solid-liquid interface. Meanwhile, the decrease of the thickness of the liquid film due to the shrinkage of dissolving particle could limit the variation of E_{sl} . This limitation becomes more significant when the diameter of solid particle reduces to certain level at around 2300s of reactive crystallization. Subsequently, the dissolution rate tends to slow down due to the decrease of E_{sl} at the end of crystallization in Fig. 5.2 (b). For the gas-liquid mass transfer, E_{gl} remains at constant during the absorption of CO_2 , which means the enhancement effect of chemical reaction on gas-liquid mass transfer can be neglected.

The proposed mathematical model is able to predict the evolution of ions concentration, pH of the solution and the amount of dissolving solids and newly formed crystals. However, a certain degree of uncertainty of the simulation still exists, namely deviations between the experimental and modeling results. One reason could be the simplification of the dissolution model, as the solids here are assumed perfect spherical particles with identical diameters. In reality, the raw materials are not always perfect spheres or cubes, but rather agglomerates with various morphology, and the breakage of such large agglomerates may alter the total solid-liquid contact area, influencing the dissolution rate. This issue was addressed in Publication [II]. The other reason is the assumption of ideal mixing in the stirred tank. The breakage rate of particle agglomerates and gas bubbles near the impeller could be larger than the tank average value due to the non-uniform distribution of the turbulent intensity. As a result, gas-liquid and solid-liquid mass transfer rates can be different from point to point in the domain. In addition, the nucleation rate could be strongly influenced by several parameters, including supersaturation, turbulent intensity and suspension density (Mersmann, 2001). Therefore, different nucleation kinetics were fitted against experimental data under different operating conditions in this chapter. In publication [I], the nucleation

kinetics present a linear dependence with volumetric gas-liquid mass transfer coefficient, which is determined by fluid, filled in stirred tank reactors. The influence of fluid field on the multiphase crystallization will be investigated in Publication [III].

5.3 Population balance modeling for solid-liquid reactive dissolution

5.3.1 Introduction

Publication [II] proposed a population balance model coupled with a mass transfer model to simulate the simultaneous shrinkage and breakage of particles during the reactive dissolution of particle agglomerates in stirred tank as in Fig. 5.4. The high-order moment-conserving method of classes (HMMC) was adopted to solve the population balance model. The shrinking particle model was used to calculate the solid-liquid mass transfer rate in which driving force was estimated by considering the physical constraints including electroneutrality, water dissociation and dissolution equilibrium. The simulation results, including the concentration and the particle size distribution of the final products, were validated by experiments carried out in a laboratory scale stirred tank.

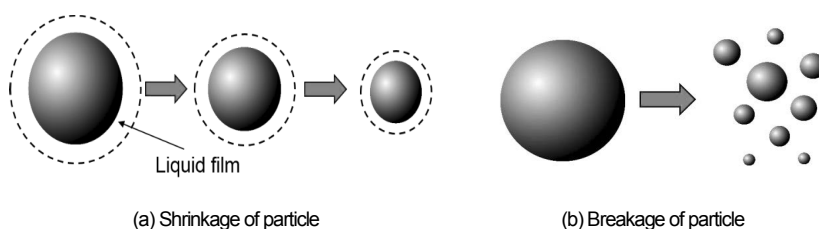


Figure 5.4 Graphical representation of different phenomena occurring during the reactive dissolution.

5.3.2 Experimental validation

In each batch reactive dissolution, 2.5L HCl solution ($\text{pH} \approx 1$) was first mixed in the reactor at 25°C . When the temperature and pH achieved stable values, $\text{Mg}(\text{OH})_2$ solids were rapidly added into the solution. Samples were taken at different times and filtered immediately. The dissolution rate can be obtained by tracking the concentration of magnesium ion in the filtrate and pH of solution. Unfortunately, based on the separate tests, the response time of pH meter was around 15s, which is too slow to follow the reactive dissolution. The PSD of the final products were measured by analyzing the filter residue with a Mastersizer 3000 laser diffraction analyzer. In order to validate the proposed model, different initial conditions (particle sizes) and operation conditions (impeller speeds) are used in Table 5.3. For the raw material, it is difficult to validate the dissolution rate due to the present of a mass of fine particles that dissolve extremely rapidly. Therefore, the two larger samples were obtained by mechanical sieving (Retsch AS-200). The influence of initial conditions on the

reactive dissolution can be found by carrying out the tests with different sieved samples and identical impeller speed (Case 1 vs Case 2) while the effect of operating conditions on the reactive dissolution can be revealed by performing the tests with the same sample but different impeller speeds (Case 2 vs Case 3).

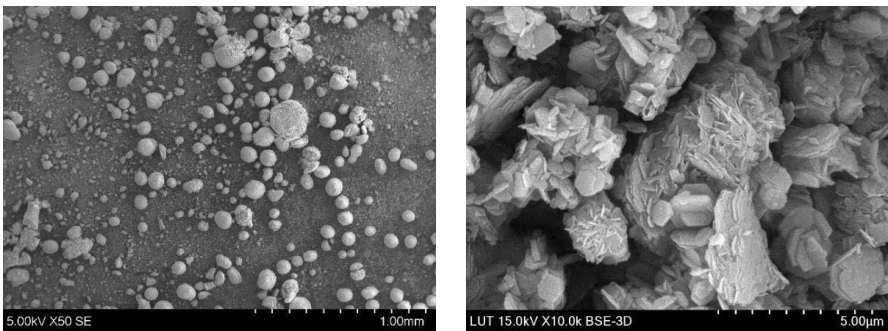
Table 5.3. Initial and operating conditions

No.	Seived sample, μm	Impeller speed, rpm	Initial pH	Initial mass of solids, g
Case 1	25 - 250	560	1.01	10.04
Case 2	125 - 500	560	0.97	10.09
Case 3	125 - 500	360	0.98	10.01

5.3.3 Results and discussion

5.3.3.1 Initial PSD

As the proper description of the initial condition is essential in the solution of the population balance model, the accurate discretization of the initial PSD is crucial to model the reactive dissolution. The SEM pictures of the raw materials are illustrated in Fig. 5.5: (a) raw materials are polydispersed particle mixture with roughly spherical shape, providing the feasibility of the assumption on the agglomerate shape; (b) the enlargement of the same sample shows the morphology of the particles. A high degree of the agglomeration in the raw material can be observed on a smaller spatial scale, demonstrating the fact that the breakage event can produce particles with a wide size range.



(a) $\text{Mg}(\text{OH})_2$ (scale bar 1mm)

(b) $\text{Mg}(\text{OH})_2$ (scale bar 5µm)

Figure 5.5. Characteristic SEM images of raw particle material

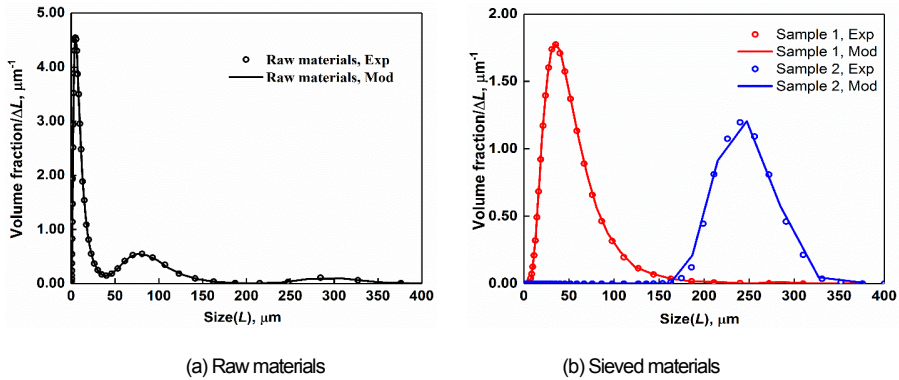


Figure 5.6. Initial PSD of the Mg(OH)₂ particles

The initial PSD of particles is usually obtained by using a predetermined probability density function such as lognormal or Weibull distribution in which parameters are fitted against measured PSD. The high degree of polydispersity of the raw materials in Fig. 5.6(a), however, may lead to deviations between the fitted and measured initial PSD, which introduces further modelling errors. Therefore, the moment-conserving discretization of the initial PSD is performed. The main idea of discretization is to distribute the measured PSD into the predefined size classes, which can give excellent prediction of not only the shape, but also of the moments of the initial PSD in Fig. 5.6.

5.2.3.2 Parameter fitting

The concentration of magnesium ion and the PSD of the final products were calculated and compared with the experimental results under different initial and operating conditions. The only unknown physical parameters including the particle breakage constant (c_{br}) and the parameter of the DSD function (c_γ) were fitted against the experimental data, and the results of this procedure are reported in Table 5.4. These parameters are tank average values that are obtained based on the assumption of spatial homogeneity of the laboratory scale reactor. In the stirred tank reactor, the breakage rate of particle agglomerates near the impeller could be larger than the tank average value due to the non-uniform distribution of the turbulent intensity, as well as the PSD can be different from point to point in the domain. Indeed, a fitting process that involves the influence of hydrodynamics, mainly considering the local energy dissipation rate, could result in a more applicable and realistic set of physical parameters. However, the aim of Publication [I-II] is to formulate a simple model that helps us in the understanding of the investigated process; a detailed CFD model of the reactive dissolution is outside the scope of Publication [II] and left for the future.

Table 5.4 Breakage rate constant and parameter of beta distribution

Parameter	Value (95% confidence interval)
c_{br} (Eq 3.34)	$1.12 \times 10^{-5} \pm 9.82 \times 10^{-7}$
c_γ (Eq 3.30)	$1.35 \times 10^2 \pm 7.42$

5.2.3.3 The influence of operating conditions on the reactive dissolution

The dissolution rate can be calculated from the time evolution of the magnesium ion concentration in Fig. 5.7(a). It shows that the dissolution rate increases when the impeller speed increases or the initial particle size decreases: such rate is in fact governed by the solid-liquid mass transfer rate, which consists of three different terms, namely the mass transfer coefficient, the mass transfer area and the dissolution driving force. The effect of PSD and turbulent energy dissipation on the solid-liquid mass transfer coefficient and, therefore, on the total mass transfer area is clear in Fig. 5.7(b) and Fig. 5.7(c): the total mass transfer area is the highest in Case 1, where the initial PSD is shifted towards smaller particle diameters and where the impeller speed are constant. By observing Case 2 and Case 3, it is possible to note that a stronger turbulent intensity caused by the faster impeller speed results in a higher mass transfer rate, with a combined effect provided by an enhanced mass transfer and a higher particle breakage rate. In fact, in Case 2 a large amount of fine particles generated by the agglomerate breakage can speed up the dissolution as compared with Case 3, by providing a larger interfacial area for mass transfer. In addition, the present model can give a better understanding of reactive dissolution by analyzing the influence of operating conditions on both particle diameter and mass transfer area. The Sauter Mean Diameter (d_{32}) of the particles and the solid-liquid mass transfer area (A) are shown in Fig.5.7 (b) and Fig.5.7 (c). Case 1 produces the particles with smallest d_{32} and largest A , which results in a highest mass transfer rate, while Case 3 produces the particles with the largest d_{32} and smallest A , which results in a lowest mass transfer rate. These results agree with the experimental data in Fig. 5.7(a). Compared with Case 2 and Case 3, it is worth noting that the mass transfer area decreases in Case 1 in the first 40 s and then increase as depicted in Fig. 5.7(c). In theory, the mass transfer process reduces the mass transfer area according to the shrinking particle model while the particle breakage increases mass transfer area by generating fine particles. Therefore, it can be deduced that the particle dissolution has a major influence on the solid-liquid mass transfer area of the smaller particles (Sample 1) while particle breakage dominates the evolution of mass transfer area of the large particles (Sample 2). The different tendency between d_{32} and A proves that the mass transfer rate cannot be predicted accurately by only tracking two moments of the distribution, which usually are the total number of particles and the total volume of the system. A proper prediction in fact requires also the inclusion of an additional moment accounting for the total interfacial area, and therefore the use of the HMMC for the solution of the PBE for mass transfer problems is favorable. Finally, the present model can give an excellent prediction of the PSD with the fitted physical parameters in Fig. 5.7 (d). It is also possible to notice that

the final particle size at the steady state is mainly determined by the impeller speed, with a negligible effect of the initial PSD.

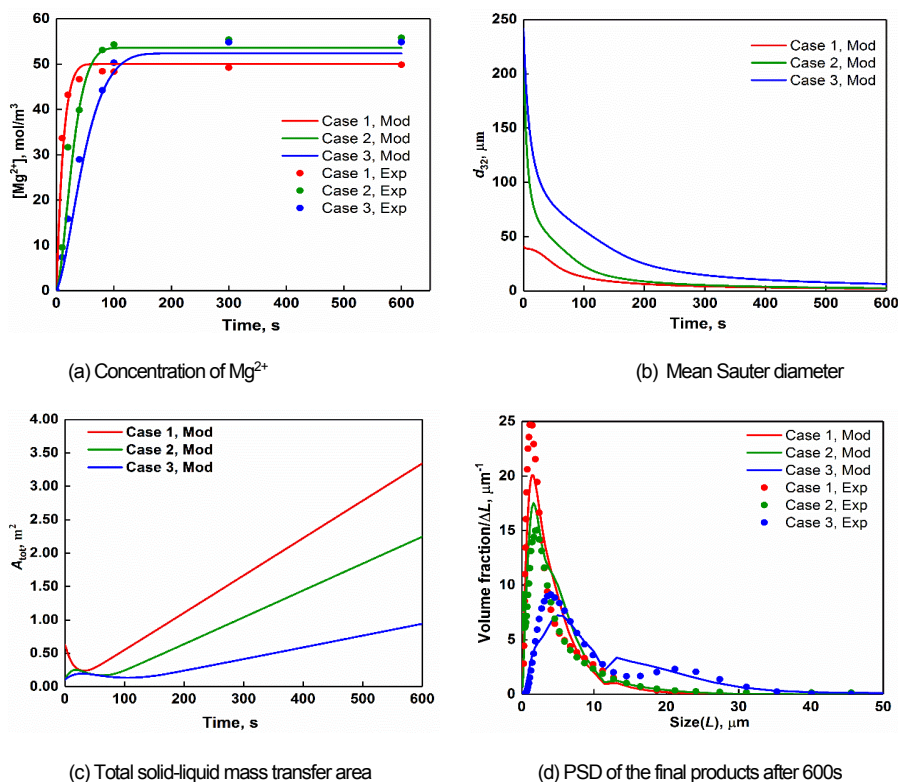


Figure 5.7 Modelling vs Experimental results

5.2.3.4 The influence of breakage frequency and DSD function on the reactive dissolution

The influence of the impeller speeds on particle diameter and mass transfer area shows that particle breakage could play an important role in the reactive dissolution of particle agglomerate. The evolution of PSD simulated by the reactive dissolution model (Case 2) with and without breakage are compared in Fig. 5.8. The PSD calculated by the model without breakage is only controlled by the solid-liquid mass transfer. Since the mass transfer rate of the smaller particles is higher than the larger ones, the PSD slowly becomes wider in Fig. 5.8(a). This behavior is not consistent with the experimental data reported in Fig. 5.7 (d). The results calculated by the model including breakage shows instead that such phenomenon rapidly shifts the PSD towards smaller particle diameters, as depicted in Fig. 5.8(b). Therefore, it is crucial to correctly describe the breakage of the agglomerations for the modeling of the present reactive dissolution.

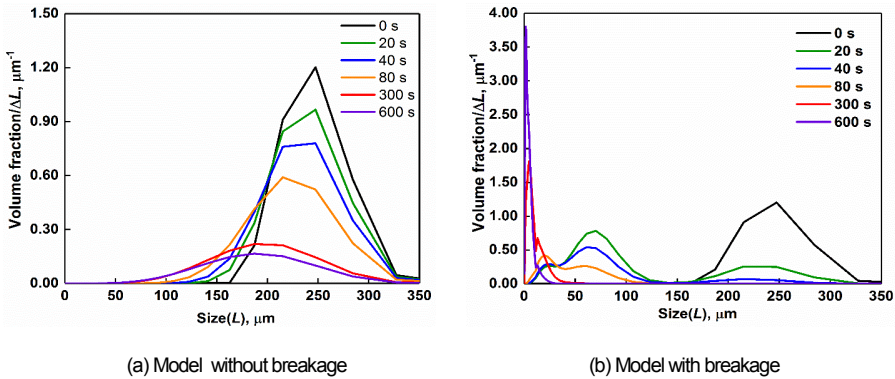


Figure 5.8 Modelling results of PSD evolution (based on the initial solid volume)

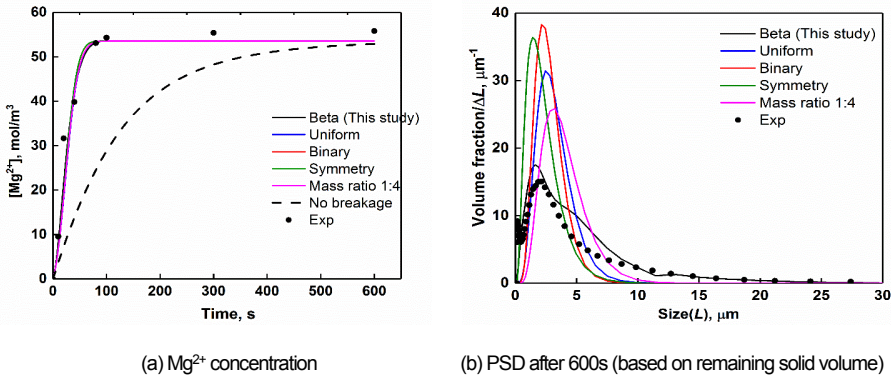


Figure 5.9 The influence of different DSDs on the PSD

As it is possible to see from Fig. 5.9(a), the model without breakage results in a large deviation from the experimental data, which again stresses the importance of the particle breakage in the modeling of reactive dissolution of $Mg(OH)_2$ agglomerates. Meanwhile, the DSD functions accounting for the number of fragments (and their sizes) generated after the breakage event must be properly selected in order to predict the PSD accurately. Several DSD functions were implemented into the population balance model. To compare the influence of DSD functions, breakage rate constants (c_{br}) in Eq. (3.29) were fitted independently for each DSD function to guarantee the same dissolution rate in Table 5.5. It is apparent that different DSD functions result in different PSDs of the final product in Fig. 5.9(b) with the same dissolution rate. It is worth remarking that the DSD highly depends on the investigated system and in particular on the agglomerates internal stress and the interaction with the hydrodynamics. Therefore, the formulation of a phenomenological model can be very tricky, since the available experimental data are not sufficient for a more detailed validation. The prescribed beta distribution, instead, due to its flexibility compared with other imposed DSD, is able to provide a good agreement compared with the

experimental data at different operating conditions (Fig. 5.7 (d)) by using a unique set of parameters. Nevertheless, since the structure and the strength of the particle agglomerates are case dependent, the breakage rate constant could be varying in different systems, although these results are promising from a modeling point of view.

Table 5.5 Breakage rate constants corresponding to the tested DSD functions

DSD functions	Value of c_{br} (95% confidence interval)
Beta (Study case)	$1.12 \times 10^{-5} \pm 9.82 \times 10^{-7}$
Uniform	$9.83 \times 10^{-5} \pm 5.60 \times 10^{-6}$
Binary	$9.04 \times 10^{-5} \pm 1.33 \times 10^{-5}$
Symmetry	$5.47 \times 10^{-5} \pm 8.23 \times 10^{-6}$
Mass ratio 1:4	$1.02 \times 10^{-4} \pm 5.83 \times 10^{-6}$

5.2.3.5 The solid-liquid interface concentration

The interface concentration and mass transfer rate of components in Case 2 are presented in Fig.5.10 and Fig. 5.11. The interface concentration of Mg^{2+} and Cl^- are larger than the saturated concentration while the concentration of OH^- is smaller than the saturated concentration in Fig.5.10. The concentration gradient of Cl^- between the bulk solution and solid-liquid interface exists during the reactive dissolution even though the mass transfer flux of Cl^- is zero. By introducing the Nernst-Planck equation, moreover, the conservation for the electroneutrality of the mass transfer flux is also guaranteed in Fig. 5.11. According to Eq. (2.11) and Eq. (2.18), the mass transfer fluxes are not only influenced by diffusion coefficient of each component but also by charges of ions. The mass transfer rate of Mg^{2+} increases at first 10s and then decreases. This is mainly caused by the small variation of mass transfer area in Fig. 5.7(c). It can be deduced that the accurate prediction of the mass transfer area, which is determined by the particle size distribution, is critical to the modelling of reactive dissolution. The time-dependent interface concentrations represent the major difference between the reactive dissolution and non-reactive dissolution. By considering the physical constraints (electroneutrality, water dissociation and dissolution equilibrium) and the transport of all the components, the model can provide a more feasible and accurate prediction of the mass transfer rate than the constant value simply calculated from the solubility equilibrium.

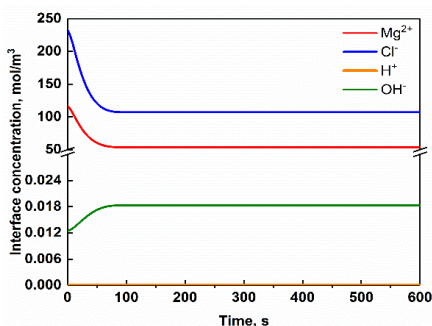


Figure 5.10. Interface concentration of components

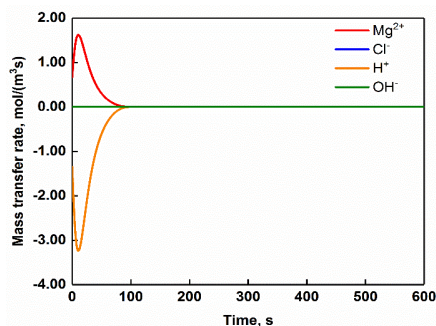


Figure 5.11. Mass transfer rate of components

The comparison between the modeling results and the data measured during reactive dissolution experimental campaign carried out in a laboratory scale stirred tank reactor pointed out several interesting aspects. Firstly, the model is capable of predicting the influence of different initial particle size and impeller speed on the reactive dissolution rate. Then, the influence of particle breakage on the Sauter Mean Diameter and the mass transfer area were identified: the inclusion of the particle breakage in the model is crucial to the accurate simulation of the dissolution rate and the evolution of particle size distribution. Compared to several daughter size distributions in the literature, the beta distribution provided the most flexible way to predict the breakage of solid agglomerates with complex internal structures. Finally, the interface concentration estimated by considering the physical constraints including electroneutrality, water dissociation and dissolution equilibrium, was found to be different from the values calculated by the solubility equilibrium during the reactive dissolution.

5.4 Compartmental modeling of gas-liquid crystallization

5.4.1 Introduction

As mentioned in section 5.2, the non-ideal mixing could lead locally different particle behaviors and mass transfer rates during the gas-liquid reactive crystallization in a stirred tank reactor. A ‘network of multi-zones’ analysis, namely compartmental model, was adopted in publication [III] to assess the influence of fluid dynamics on the crystallization process of $\text{CO}_2(\text{G})\text{-Ca}(\text{OH})_2(\text{aq})$ system in a stirred tank. The model combines the flow field with several sub-models, including gas to liquid mass transfer, chemical reaction, crystallization and population balance for both gas bubbles and solid crystals. The modeling predictions, including the average volumetric mass transfer coefficient, the concentration of calcium ions, the pH of the solution and the Sauter mean diameter of the final crystal products are eventually compared with experimental measurements.

5.4.2 Experimental validation

In order to validate the compartmental model, two different experiments were performed in this work. Measurements of the volumetric mass transfer coefficient ($k_L a$) of the investigated system were already carried out in the literature. To test the feasibility of compartmental model and validate the gas-liquid mass transfer separately, the compartmental model was first carried out for the CO₂-H₂O system. Then solution of Ca(OH)₂(aq) with initial concentration of 20.32 mol/m³ was prepared in a stirred tank reactor. The pure CO₂ gas was introduced from the gas sparger located at the bottom of tank. The dynamic calcium concentration, [Ca²⁺], and the pH of the solution from experiments performed under different operating conditions were measured. The initial and operating conditions are listed in Table 5.6.

Table 5.6. Initial and operating conditions

Initial condition	Values	Operating conditions	Values	
Concentration of Ca(OH) ₂ (aq)	20.32 mol/m ³	Impeller speed	350 rpm	650 rpm
			560 rpm	750 rpm
Volume of the dispersion	2.64×10 ⁻³ m ³	Gas flow rate	1.67×10 ⁻⁵ m ³ /s	
			8.35×10 ⁻⁵ m ³ /s	

5.4.3 Numerical details

Fluent 16.0 software was used to solve a transient gas-liquid flow field in a stirred tank with Rushton turbine and four baffles located symmetrically at the inner wall of the reactor. Impeller motion was accounted for using a Multiple Frames of Reference method, where the tank is divided into two zones, with a zone around the impeller in rotating frame of reference where impeller appears stationary as in Figure. 5.12 (a). The computational domain consisted of 366644 hexahedral grids as in Figure. 5.12 (b). Grid independent study shows no significant variations on the properties of interest after further refinements.

For a gas-liquid-solid system, the extremely complex interactions between different phases are poorly understood due to the lack of effective and reliable experiment validation. Therefore, several assumptions are proposed:

- (1) Normal distribution with mean diameter of 4 mm and standard deviation of 1 mm is assumed as the initial PSD for bubbles, as the bubbles ranging between 1-8 mm have approximately the same terminal velocity (Clift et al., 1978).
- (2) Only buoyancy, gravity and drag forces are taken into account, because they are the most important factors for determining gas holdup and bubble size distribution in agitated vessels (Lane et al., 2005).
- (3) The crystals are assumed to follow the liquid flow, since the Stokes number of the crystals (with size smaller than 100 μm) is generally smaller than 0.1 (Tropea et al., 2007).
- (4) The power-law functions of the supersaturation are adopted to calculation nucleation and crystal growth rate. The crystal growth rate is taken to be independent of crystal size.

The Eulerian multiphase model was chosen to describe the continuity and momentum equations for each phase. The RANS approach, namely the realizable $k-\varepsilon$ turbulence model for the mixture with standard wall functions, was adopted to predict the turbulence of the stirred tank. The degassing boundary condition was used to model the gas flowing out at the top surface of the tank. This calculation can provide an accurate prediction of gas-liquid flow field and local value of pressure, energy dissipation and volume fraction of each phase. Before coupling the flow field with the mass transfer, chemical reaction and crystallization models in the compartmental model, the CFD domain needs to be split into a network of inter connected compartments by utilizing a user-defined function in Fluent 16.0. An idealized mixing pattern is assumed for each compartment.

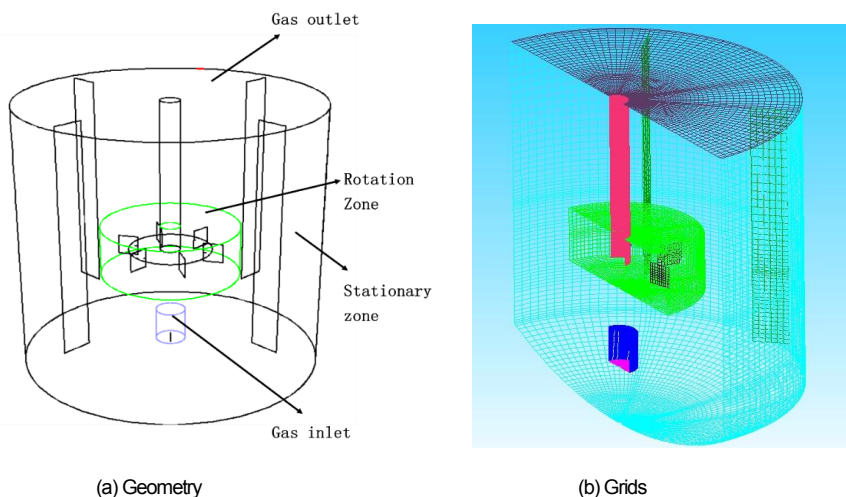


Figure 5.12 Geometry and mesh of the stirred tank

5.4.4 Compartment number/size independence study

The compartmental approach is always a compromise between computational costs and accuracy. The compartmental model was first tested with 6 compartments. The simulation results were found to change with the increased compartment number, especially near the impeller region. Therefore, compartment number/size independence was studied by increasing the compartment number from 6 to 85 in Figure 5.13. As can be noted, the difference between 48 and 58 compartments is mainly in the division of the upper part of the stirred tank, which is an area where bubble coalescence occurs, and the modeling of such part may influence the prediction of the overall mass transfer coefficient. We performed the study for the following operating condition: impeller rate is 560 rpm and the gas flow rate is $1.67 \times 10^{-5} \text{ m}^3/\text{s}$. The results in terms of pH time evolution and the volume averaged d_{32} of the final crystal product (at 150 s) were compared and shown in Fig 5.14 and Fig 5.15.

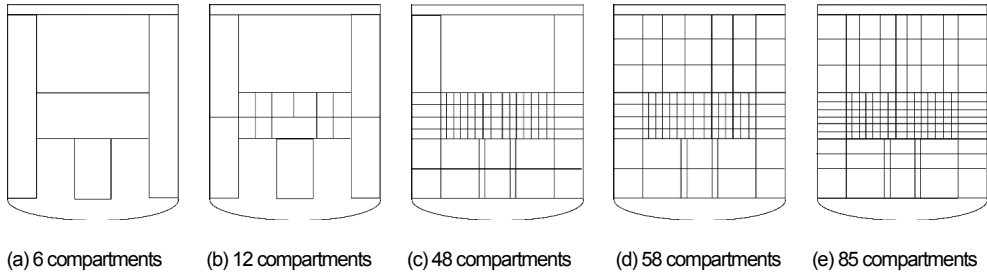


Figure 5.13. The schematic diagram of compartment number/size study

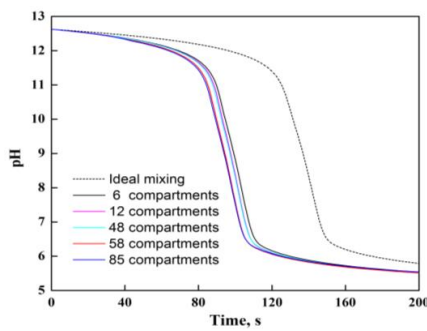


Figure 5.14. pH of the solution

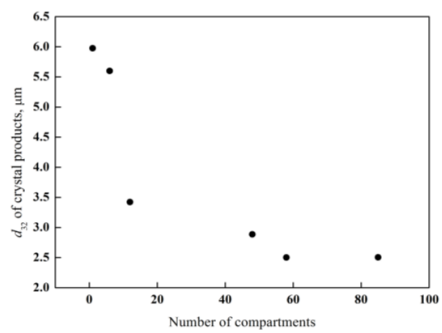


Figure 5.15. d_{32} of crystal products

As can be seen from the figures, the pH evolution is quite similar for all the cases, while the Sauter mean diameter of the crystal product first decreases rapidly with the number of compartments, after which the change is moderate. Based on this analysis, the predicted Sauter mean diameter remains constant when the number of compartments is above 58. Therefore, we decided to perform all the simulations with 58 compartments.

5.4.5 Result and discussion

5.4.5.1 CFD simulation and compartmentalization

The quality of the compartmentalization should be evaluated by comparing the flow field from CFD simulation and that obtained from compartmental algorithm, which has been shown Fig. 5.16. The comparison of essential variables including the distribution of energy dissipation rate (ε) and the gas volume fraction (φ_G) shows that compartmentalization with 58 subdivisions is capable of preserving the characteristic of flow fields in this investigated gas-liquid agitated vessel.

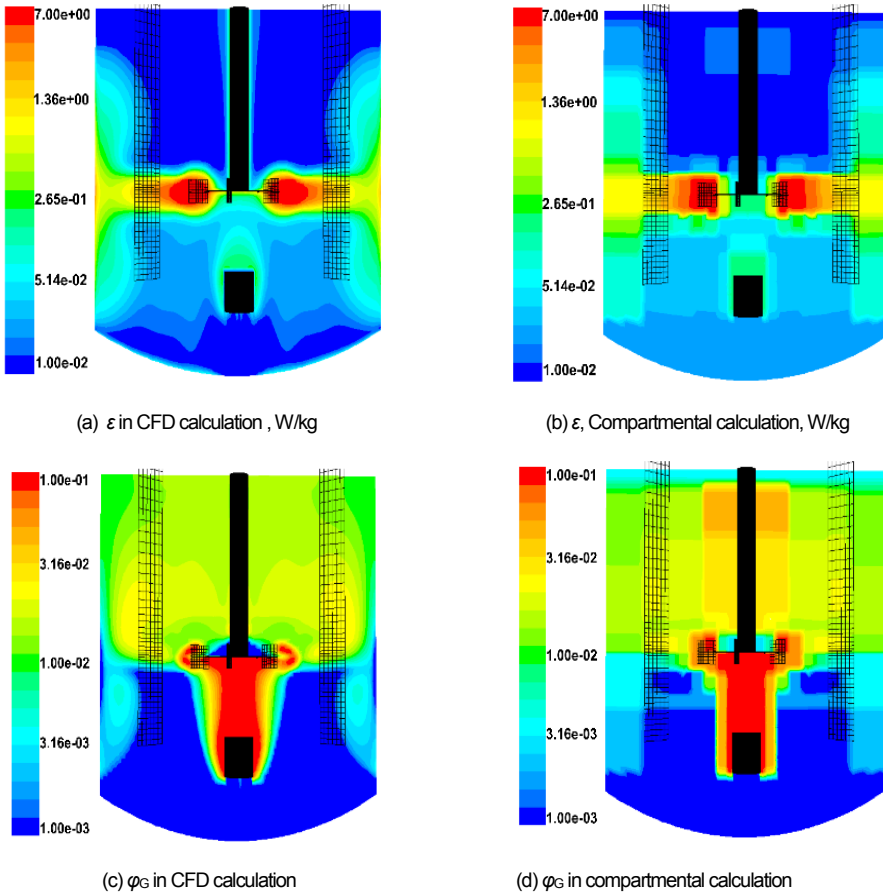


Figure 5.16. Comparison of energy dissipation (ϵ) and gas hold up (φ_G) between CFD and Compartmental simulation

5.4.4.2 The influence of impeller speeds and gas flow rate on the mass transfer and crystallization

The comparison between the modelling results and experimental results of volume average $k_L a$ at steady state in $\text{CO}_2\text{-H}_2\text{O}$ system are shown in Table 5.7. In order to estimate $k_L a$ of CO_2 , experiments of oxygen absorption in water were performed with different impeller speeds and gas flow rate in the same reaction. By monitoring concentration of oxygen in water, $k_L a$ of O_2 was firstly calculated with method published by Fuchs et al. (1971)(Fuchs, Ryu, Humphrey, & Fuchs, 1971). Then $k_L a$ of CO_2 is estimated by correlation of $k_L a_{\text{CO}_2} / k_L a_{\text{O}_2} = (D_{\text{CO}_2} / D_{\text{O}_2})^{0.5}$, proposed by Hu et al. (2005). As one may note, the agreement is very good under different operating conditions, meaning that the compartmentalization strategy and set of sub-models are adequate to describe the system.

Table 5.7. Experimental validation of the steady state $k_{1,a}$

N , rpm	Q , $\text{m}^3 \cdot \text{s}^{-1}$	$k_{1,a}$ (Experiment), s^{-1}	$k_{1,a}$ (Modeling), s^{-1}
560	1.67×10^{-5}	0.0196	0.0189
650	1.67×10^{-5}	0.0304	0.0289
750	1.67×10^{-5}	0.0452	0.0427
560	8.35×10^{-5}	0.0345	0.0333

Experimental and modeling results of $[\text{Ca}^{2+}]$ and pH under different impeller speeds are shown in Fig. 5.17. At the first 20s of crystallization, namely nucleation period, the value of $[\text{Ca}^{2+}]$ remains constant due to the small size of crystal nucleus. Then growth of crystal prevails the crystallization and $[\text{Ca}^{2+}]$ decreases quickly. The evolution of pH shows similar trend as $[\text{Ca}^{2+}]$. pH of the solution is mainly governed by the gas-liquid mass transfer and simultaneous chemical reaction between $\text{CO}_2(\text{aq})$ and OH^- . As previously mentioned, higher impeller speeds can improve gas-liquid mass transfer by increasing the average turbulent intensity and breaking the bubbles into smaller ones. In addition, the pH begins to drop dramatically when the crystallization stops, which is dominated by the $\text{CO}_2\text{-H}_2\text{O}$ equilibrium. Therefore, pH can be used to monitor the overall crystallization time and prevent the further dissolution of crystal products with extra CO_2 feeding.

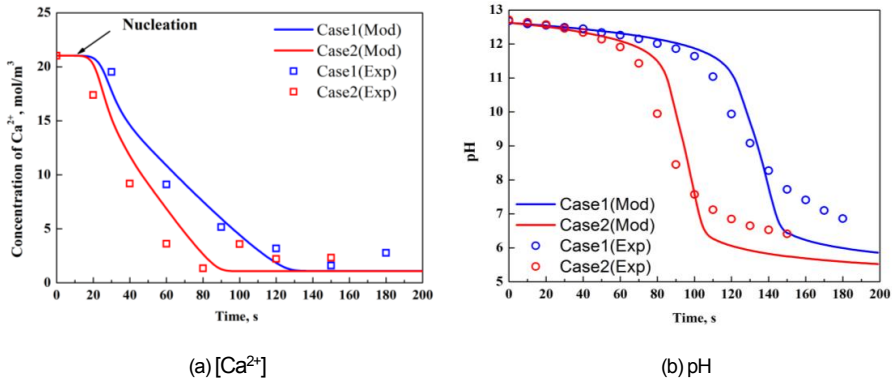


Figure 5.17. The revolution of $[\text{Ca}^{2+}]$ and pH.

Case1: $N= 350$ rpm; $Q = 1.67 \times 10^{-5} \text{ m}^3/\text{s}$; Case2: $N= 560$ rpm; $Q = 1.67 \times 10^{-5} \text{ m}^3/\text{s}$.

The effect of the impeller speed on the d_{32} of the final products is presented in Table 5.8. It is shown that d_{32} decreases with increase of impeller speed, as one may expect due to the prevailing of particle breakage over agglomeration at higher energy dissipation rate.

Table 5.8. The influence of impeller rate on the d_{32} of final crystal products (at 150s)

	N , rpm	Q , m ³ /s	d_{32} (Exp), μm	d_{32} (Mod), μm
Case 1	350	1.67×10^{-5}	8.86	7.24
Case 2	560	1.67×10^{-5}	2.24	2.56

5.4.5.3 Local information of the stirred tank

At the beginning of crystallization, the concentration of OH^- in the solution is relatively high. Therefore, $\text{CO}_2(\text{L})$ is quickly consumed by the chemical reaction between OH^- and $\text{CO}_2(\text{L})$. Therefore, the driving force of gas-liquid mass transfer is quite large due to the low level of $\text{CO}_2(\text{L})$ in bulk solution. Bubbles could shrink sharply caused by the fast mass transfer. As a result, the average gas volume fraction, φ_G , decreases quickly during the first few seconds in Fig. 5.18(a). Both of the experimental and modeling results of $[\text{Ca}^{2+}]$ show that the crystallization stops at 90s (Case 1) in Fig. 5.17(a). Then $\text{CO}_2(\text{L})$ starts to accumulate in the system, which will reduce the driving force of gas-liquid mass transfer. Therefore, φ_G starts to increase rapidly with time after 90s. In order to understand the behavior of the gas-liquid mass transfer during the crystallization, the local PSD of bubbles and volumetric mass transfer coefficient (k_{La}) at 30s are shown in Fig. 5.18(b) and Fig. 5.18(c). As can be seen, the bubbles in the feeding area (compartment 1) are larger than the impeller area (compartment 30) and suspension area (compartment 53), since coalescence phenomenon is prevailing in the region with high gas volume fraction. The bubble distribution in the impeller area is shifted towards smaller size as the breakage and mass transfer are prevailing in the region with high turbulent intensity. In the suspension area, the bubble have an average value in between these two extremes but a wider PSD, which is mainly determined by the combined action of gas-liquid mass transfer and bubble coalescence. The spatial distribution of k_{La} is shown in Fig. 5.18(c). As it is shown, the flow field with nonideal distribution of turbulent intensity and gas volume fraction has a significant effect on the local gas-liquid mass transfer rate. In the feeding area, higher local gas volume fraction leads to the larger values of k_{La} . Meanwhile, higher energy dissipation rate in the vicinity of impeller can also improve the gas-liquid mass transfer by increasing mass transfer coefficient (k_L) and breaking large bubbles into smaller ones.

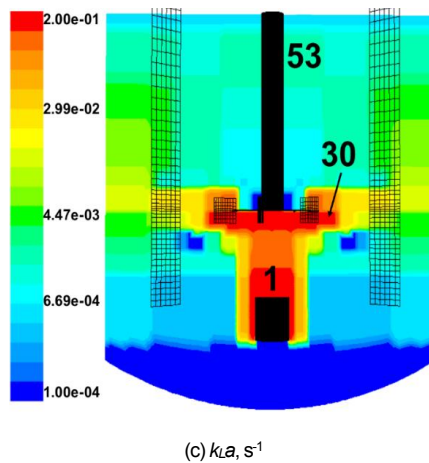
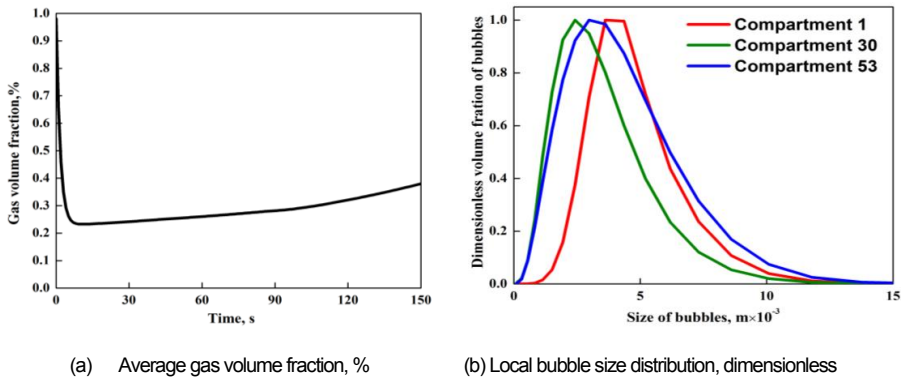


Figure 5.18. The gas volume fraction, local bubble size distribution (BSD) and local k_{La} .

The final PSD of crystal products is the result of the concurrent actions of several phenomena, including nucleation, growth, agglomeration and breakage. As the driving force of nucleation and crystal growth, local supersaturation is calculated and shown in Fig. 5.19. In the feeding region (compartment 1), evolution of supersaturation is faster than that in the impeller region and the suspension region due to the high gas volume fraction. Nevertheless, the difference of supersaturation among other regions of the vessel is very small, which means the mixing of liquid is uniform in other regions. Except nucleation and growth, the PSD of final crystal products is also influenced by the breakage and agglomeration in the agitated vessel.

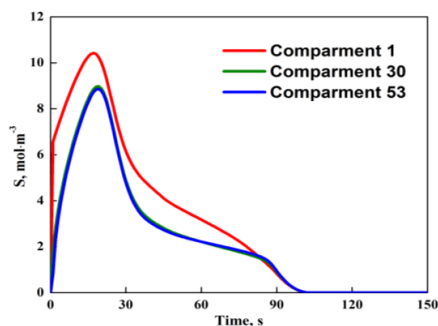


Figure 5.19. The local supersaturation

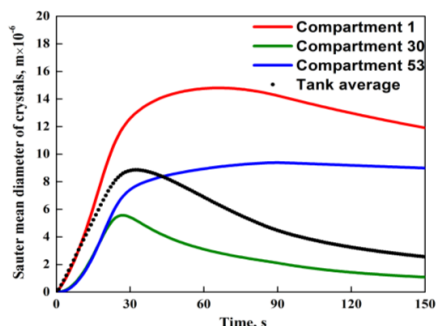


Figure 5.20. The local d_{32} of crystals

The local and volume averaged Sauter Mean Diameters, d_{32} , are shown in Fig. 5.20. The average d_{32} is determined by the competition of several processes. Nucleation, growth and agglomeration increase the average size of crystal while breakage decreases it. As it is shown, the nucleation, growth and agglomeration are prevailing at first 25s, corresponding to the highest value of supersaturation. After that, average d_{32} decreases since the breakage of larger agglomerates becomes predominant with decreasing of supersaturation. Regarding to the local evolution of d_{32} , the stronger turbulence near the impeller (compartment 30) will lead to an earlier drop of d_{32} . In addition, pH drops at about 90s in Fig. 5.17 (b). According to the $\text{CO}_2\text{-H}_2\text{O}$ equilibrium, $[\text{CO}_3^{2-}]$ cannot exist in the solution when pH is lower than 9. Therefore, the supersaturation also fades away with the decreasing pH after 90s. Further gas feeding after this point is not beneficial as it may produce extra hydrogen ion which leads to further dissolution of CaCO_3 crystal product (Cents et al., 2005).

In the light of above discussion, non-ideal distribution of turbulent intensity and gas volume fraction indeed have a significant influence on gas-liquid reactive crystallization in the investigated agitated vessel. Negligence of interactions between hydrodynamics and detailed physical and chemical processes could lead to larger deviation between simulation and realistic situation during scale up of gas-liquid crystallizers. Compared with a full coupling of CFD calculation and comprehensive models, compartmental model provides a versatile and effective way to simulate the complex multiphase system. In addition, it is also allowed to change the chemical components and operating parameters without performing extra CFD simulation, which is desirable at the initial stage of process development.

5.5 The influence of microwave field on reactive crystallization

5.5.1 Introduction

In order to quantitatively study the effect of microwave field on crystallization kinetic parameters, mathematical models and corresponding experimental validation for a continuous reactive crystallization process with MgCO_3 as the working substance were carried out and presented in Publication [IV]. A full population balance model considering inflow, outflow, nucleation, crystal growth, agglomeration and breakage were solved with HMMC. The unknown parameters, including nucleation rate constant (k_n), crystal growth rate constant (k_g), exponents of nucleation and growth rates (n and g) and breakage rate constants (k_{br}) were fitted against experimental results. The agglomeration efficiency (ψ_s) was calculated based on the fitted parameter and analyzed in Publication [IV].

5.5.2 Experimental validation

Crystals of MgCO_3 were formed via reaction between solutions of MgSO_4 and Na_2CO_3 in a continuous MSMR crystallizer (0.22 L) at constant temperature of 25.0°C and constant stirring speed of 300 rpm. Six feeding concentrations (0.1 mol/L, 0.125 mol/L, 0.15 mol/L, 0.175 mol/L, 0.2 mol/L and 0.225 mol/L) and five energy inputs of microwave (0 W, 1.94 W, 3.87 W, 5.81 W and 7.78 W) were applied as operating conditions. The concentration of Mg^{2+} and Sauter Mean Diameters (d_{32}) of final products were measured and used for model validation and parameter fitting. The sample of MgCO_3 crystals was analyzed by a BECKMAN COULTERTM particle size analyzer. For each operating condition, d_{32} of three parallel samples were tested to check the repeatability of the measurement. In addition, the concentration of Mg^{2+} in steady-state solution was obtained by titration with EDTA.

5.5.3 Numerical details

The crystallization kinetics MgCO_3 were fitted against the experimental data by adopting the least squares method (lsqnonlin function) in Matlab R2017a. The objective function of the fitting algorithm is defined as:

$$F = w_1 \frac{d_{32,mod} - d_{32,exp}}{d_{32,exp}} + w_2 \frac{c_{Mg,mod} - c_{Mg,exp}}{c_{Mg,exp}} \quad (5.1)$$

where subscripts *mod* and *exp* represent the modelling and experimental results respectively; w_1 and w_2 are weighting factors for d_{32} and c_{Mg} . In addition, the parameter fitting results could be very sensitive if there was a significant magnitude difference between variables. Therefore, nondimensionalization was performed by introducing average experimental values. The nonlinear least squares fitting procedure can be carried out as follow:

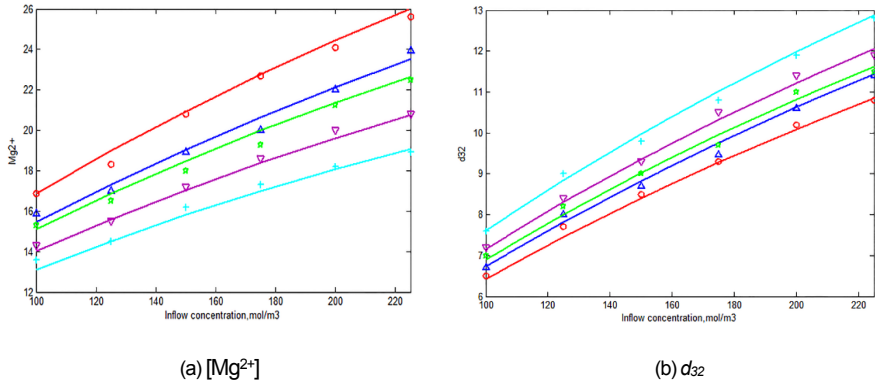
$$\min_{\mathbf{x}} \|F(\mathbf{x})\|_2^2 = \min_{\mathbf{x}} (F_1(\mathbf{x})^2 + F_2(\mathbf{x})^2 + \dots + F_n(\mathbf{x})^2) \quad (5.2)$$

where \mathbf{x} is the vector of unknown parameters; n is the total number of experiments used for parameter fitting. After giving initial values, the final parameters can be obtained with 95% confidence intervals.

5.5.4 Results and discussion

The experimental results and the prediction of Mg^{2+} concentration in steady-state solution under different inflow concentrations and microwave energy intensities are shown in Figure 5.21 (a). From this figure, it is observed that the concentration of Mg^{2+} increases when the inflow concentration increases. Meanwhile, at a given inflow concentration, the concentration of Mg^{2+} decreases with raise of microwave energy intensity. The steady-state concentration of Mg^{2+} is decided by the inflow concentration, outflow concentration and consumption by crystallization. With the increase of the inflow concentration, more Mg^{2+} and CO_3^{2-} are pumped into the reactor in a fixed time interval, which leads to a raise of supersaturation of crystallization. As a driving force, higher supersaturation must lead to faster mass deposition of crystals, which consumes more Mg^{2+} in the solution. However, the steady-state concentration of Mg^{2+} still raises with increasing feeding Mg^{2+} concentration. It's can be deduced that the inflow concentration has a major influence on the composition of the crystallization system under investigated operating conditions. Meanwhile, diffusion coefficient of system is enhanced significantly by the microwave electro-magnetic effect. Liquid to crystal surface mass transfer will be improved by higher microwave intensity, leading to a faster crystal growth rate. As a result, more Mg^{2+} in the solution will transform from liquid to crystal under same inflow condition.

The experimental results and the prediction of d_{32} at various inflow concentrations and energy inputs are shown in Figure 5.21 (b). The results show that inflow with higher concentration produces crystals with larger sizes. As mentioned previously, the increase of inflow concentration leads to higher supersaturation, which improves the crystal growth rate. With the increase of microwave energy input, the crystal growth rate also increases with a higher diffusion coefficient. Moreover, the agglomeration rate is directly proportional to the crystal growth rate as shown in Eq. (3.20) and Eq. (3.21). The increase of agglomeration rate leads to larger crystals. Therefore, d_{32} grows with the increase of microwave energy input.



- and ○: The modelling curve and the experimental data with 0W
- and △: The modelling curve and the experimental data with 1.95W
- and ☆: The modelling curve and the experimental data with 3.88W
- and ▽: The modelling curve and the experimental data with 5.83W
- and +: The modelling curve and the experimental data with 7.78W

Figure 5.21. $[Mg^{2+}]$ and d_{32} at various inflow concentration and microwave energy inputs

Table 5.9. Different microwave energy input vs the crystallization kinetic parameters obtained from simulation

E	0 W	1.94 W	3.87 W	5.81 W	7.78 W
$k_n \times 10^8$	0.81±0.03	1.08±0.05	3.05±0.07	4.13±0.09	5.02±0.07
$k_g \times 10^{-10}$	0.92±0.03	1.32±0.02	1.81±0.01	3.32±0.03	4.61±0.04
g	1.52±0.05	1.41±0.02	1.32±0.01	1.15±0.03	1.09±0.02
n	6.01±0.04	6.09±0.07	6.03±0.02	6.04±0.06	6.05±0.03
k_{br}	0.51±0.02	0.53±0.01	0.52±0.02	0.51±0.01	0.51±0.02

The crystallization kinetic parameters (with 95% confidence intervals) obtained by parameter fitting against experimental data are listed in Table 5.9. It is shown that microwave field has significant influence on nucleation rate constant (k_n), growth rate constant (k_g) and exponent of growth (g). On the contrary, exponent of nucleation (n) and breakage rate constant (k_{br}) almost remain constant. k_n increases quickly with the increase of E from 0 W to 7.78 W, which can be explained by using Arrhenius correlation introduced by Li et al. (2017). The increase of k_g with increasing E is also caused by diffusion process acceleration. The diffusion process of units transporting from the bulk of the fluid phase through a stagnant film to the solid surface is improved by higher diffusion coefficient on the account of increasing of E . In addition, g decreases with the increase of E . From Mullin (2000) and Mersmann (2001), the inorganic salts crystallization from aqueous solution gives an overall exponent of growth, in the range of 1 to 2. When g approaches 1, the

crystallization process is controlled by the diffusional operation, and when g approaches 2, the crystallization process is controlled by the surface integration. With the increase of microwave energy input from 0 W to 7.78 W, g decreases from 1.52 to 1.09. This means that with the energy input increase, the crystal growth is increasingly limited by diffusion process. This influence of microwave on k_n is consistent with the former study of Guo et al. (2017), which has shown that microwave does not increase the exponent of nucleation significantly during neither homogeneous nucleation nor heterogeneous nucleation. Furthermore, microwave does not affect the breakage process during the crystallization process. As an electromagnetic wave, microwave does not cause turbulent flow in crystallization system. The impact-induced stresses and fluid-induced stresses are not changed after microwave is applied to crystallization system. Therefore, compared to agitation, microwave provide a proper solution to increase the diffusion process, meanwhile, to avoid breakage rate increase simultaneously in crystallization system.

According to Eq. (3.21), the agglomeration of crystal can be further verified by calculating the crystal collision efficiency (ψ_s) by using parameters in Table 5.9. The change of ψ_s with various energy inputs during reactive crystallization is shown in Figure 5.22. The result shows that ψ_s is enhanced significantly with the increase of the energy input. According to Hounslow et al., ψ_s depends on the ability of two newly collided particles to cement themselves together. The strength of bridge between aggregates can be enhanced by faster crystal growth rate under stronger microwave intensity, which means two newly collided particles have more chance to cement themselves together. Therefore, agglomeration could be enhanced by applying microwave to reactive crystallization processes. In order to prove above analysis, SEM images of final crystal products from reactive crystallization under various microwave intensities were compared in Publication [IV].

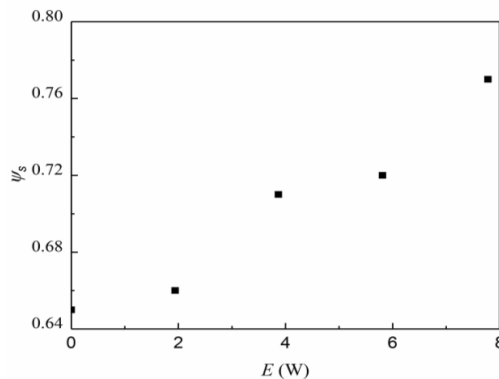


Figure 5.22. The collision efficiency (ψ_s) at various microwave energy inputs

This work shows a quantitative study of microwave energy input on crystallization kinetics at fixed temperature. It is found that the exponent of nucleation (n) and the breakage rate

constant (k_{br}) re-mains constant or changes only slightly with higher microwave energy inputs. However, the nucleation rate constant (k_n), the growth rate constant (k_g) and the collision efficiency (ψ_s) are increased significantly with microwave energy input. Furthermore, the growth rate exponent (g) is decreased. Compared to agitation, microwave provide a proper solution to increase the diffusion process and to avoid breakage rate increase simultaneously in reactive crystallization system.

6. Conclusions

In this thesis, a comprehensive study of multiphase system, including phase equilibrium, mass transfer, chemical reaction, population balance and flow dynamics is presented. The multiphase reaction models with several assumptions originated from practical applications were developed and validated experimentally. The mathematical description of the presented system provides the insight into physical phenomena from molecular scale to equipment scale, which is constituted of algebraic, ordinary and partial differential equations with strong nonlinearity and mutual coupling. Multiscale simulation, namely compartmental model, adopted in this study was found to synthesize the mechanisms at different scales and provide a powerful and rigorous computational tool for multiphase applications, including reactive dissolution, gas-liquid reactive crystallization and gas-solid-liquid reactive crystallization.

Mass transfer rate between two phases depend on mass transfer fluxes and interfacial area. For the solid-liquid mass transfer in dilute electrolyte solution, mass transfer fluxes can be described based on the two-film theory and Nernst-Planck electroneutrality. Instead of simple assumption of constant interface concentration, mass transfer fluxes are calculated numerically based on the rigorous physical constraints including electroneutrality, water dissociation and solubility equilibrium. For the gas-liquid mass transfer along with complex chemical reaction, the enhancement factor should be introduced to revise the mass transfer fluxes. The mass transfer interfacial area was calculated from particle size distribution simulated by the population balance equations (PBEs). In multiphase system, the variation of particle size distribution is mainly described by the PBEs with complex integro-differential form and high degree of nonlinearity. Two efficient numerical techniques, including classes method and moment based method, were formulated for the mentioned practical applications.

In stirred tank reactors, the non-ideal mixing could have significant effect on the behaviors of dispersed phase. Therefore, influence of flow field on detailed multiphase reaction should be investigated. A full calculation of fluid dynamics with comprehensive mass transfer, chemical reaction or population balance models requires a heavy calculation resource. To address this issue, a simulation with coarse grid method, namely compartmental model, was introduced and carried out in three steps: 1) Detail prediction of flow field by Computational

Fluid Dynamics (CFD), 2) Division of flow domain into predefined compartments and 3) Compartmental modeling. As a trade-off between the accuracy and CPU time, compartmental modeling can offer a more efficient simulation by appropriately dividing the fluid domain without the limitation of chemical components and geometries of different reactor.

For gas-solid-liquid crystallization in a stirred tank reactor, a simplified mathematical model, including dissolution of solid particles, absorption of gas bubbles and formation of crystals, was proposed with several assumptions: 1) monodispersed particle size distribution; 2) no breakage and coalescence of bubbles; 3) no breakage and agglomeration of crystals; 4) ideal mixing. The gas-liquid and liquid-solid mass transfer dominate the global rate of crystallization. Therefore, higher impeller speed and gas flow rate can significantly accelerate the gas-solid-liquid crystallization process. pH was found to be the key parameter which dominates the main species in the $\text{CO}_2(\text{G})\text{-H}_2\text{O}$ system. In addition, solid-liquid mass transfer is enhanced by the chemical reaction between $\text{CO}_2(\text{L})$ and OH^- occurring in liquid film near the solid-liquid interface. At last, the nucleation kinetics present a linear dependence with volumetric gas-liquid mass transfer coefficient, which is determined by the fluid field in stirred tank reactors. The current model was found to be very sensitive to different operating conditions. A certain degree of deviation between the experimental and modelling results was found. In order to understand the mechanism of gas-solid-liquid crystallization, reactive dissolution and gas-liquid crystallization were studied separately.

For reactive dissolution, a population balance model coupled with a mass transfer model were formulated to predict simultaneous shrinkage and breakage of particle agglomerates. Instead of average diameter, the real particle size distribution of raw material was constructed with high-order moment conserving method of classes. The dissolution rate increases with rising impeller speed and reducing initial particle size. Meanwhile, it is not sufficiently accurate to calculate the solid-liquid mass area by using Sauter Mean Diameter (d_{32}) of particle. For particle agglomerates, particle shrinkage has a major influence on the solid-liquid mass transfer area of the smaller particles while particle breakage dominates the evolution of mass transfer area of the large particles. The population balance model can provide a better prediction of mass transfer area than the assumption of monodispersed particle size distribution without particle breakage during the simulation of dissolution rate. It was also found that the inclusion of particle breakage in the PBEs is crucial to the accurate simulation of dissolution rate and evolution of particle size distribution. Compared to several daughter size distributions, the beta distribution provided the most flexible way to predict the breakage of solid agglomerates with complex internal structures. Finally, the interface concentration estimated by considering the physical constraints including electroneutrality, water dissociation and dissolution equilibrium, was found to be different from the values calculated by the solubility equilibrium during the reactive dissolution.

For gas-liquid crystallization in a stirred tank reactor, compartmental model was introduced to describe the influence of flow field on the several multiphase mechanisms, including gas to liquid mass transfer, chemical reaction, population balance and crystallization. The computational domain was subdivided into several compartments by using the spatial distribution of energy dissipation and gas volume fraction as a reference. A division with 58 compartments was found to be adequate to perform a number/size independent simulation. The model is capable of predicting tank averaged and local information, such as volumetric mass transfer coefficient, concentration of components and particle size distributions of crystals and bubbles. The results show that non-ideal mixing conditions can strongly affect not only the local gas-liquid mass transfer but also the size distribution of the final crystal product. Compartmental model is desirable at the initial stage of process development, since it is allowed to change the chemical components and operating parameters without performing extra CFD simulation. By appropriate division of the fluid domain, the compartmental model can also be used to model gas-liquid precipitation process in different geometries. Due to the low computational costs compared to a full CFD simulation, the compartmental model also allows fitting of the sub-model parameters, process optimization or model based control.

The goal of this PhD study was to develop an efficient computational methodology that describe the combination of flow dynamics and complex physical phenomena. Eventually, the compartmental model was successfully extended from previous gas-liquid system to gas-solid-liquid system to describe the reactive crystallization process. Several improvement could be considered in the future study: 1) consider the interphase force between solid and liquid; 2) scale-up the compartmental model from lab scale to pilot or industrial scale directly; 3) propose an analytical time stepping method for population balance model by reasonably allocating the time steps to further accelerate the compartmental model.

REFERENCES

- Adachi, Y., Cohen Stuart, M. A., Fokkink, R. (1994). Kinetics of Turbulent Coagulation Studied by Means of End-over-End Rotation. *J. Colloid Interface Sci.*, 165(2), 310–317.
- Alopaeus, V., Koskinen, J., Keskinen, K. I. (1999). Simulation of the population balances for liquid-liquid systems in a nonideal stirred tank. Part 1 Description and qualitative validation of the model. *Chemical Engineering Science*, 54(24), 5887–5899.
- Alopaeus, V., Laakkonen, M., Aittamaa, J. (2006). Solution of population balances with breakage and agglomeration by high-order moment-conserving method of classes. *Chemical Engineering Science*, 61(20), 6732–6752.
- Alopaeus, V., Laakkonen, M., Aittamaa, J. (2007). Solution of population balances with growth and nucleation by high order moment-conserving method of classes. *Chemical Engineering Science*, 62(10), 2277–2289.
- Alopaeus, V., Laakkonen, M., Aittamaa, J. (2008). Solution of population balances by high order moment-conserving method of classes: reconstruction of a non-negative density distribution. *Chemical Engineering Science*, 63(10), 2741–2751.
- Asai, S., Konishi, Y., Kajiwara, T. (1989). Effect of sparged gas on mass transfer between fine particles and liquids in an agitated vessel. *Journal of Chemical Engineering of Japan*, 22(1), 96–98.
- Ashraf Ali, B., Janiga, G., Temmel, E., Seidel-Morgenstern, A., Thévenin, D. (2013). Numerical analysis of hydrodynamics and crystal motion in a batch crystallizer. *Journal of Crystal Growth*, 372, 219–229.
- Ashraf Ali, B., Pushpavanam, S. (2011). Analysis of unsteady gas-liquid flows in a rectangular tank: Comparison of Euler-Eulerian and Euler-Lagrangian simulations. *International Journal of Multiphase Flow*, 37(3), 268–277.
- Ayazi Shamlou, P., Stavrinides, S., Titchener-Hooker, N., Hoare, M. (1994). Growth-independent breakage frequency of protein precipitates in turbulently agitated bioreactors. *Chemical Engineering Science*, 49(16), 2647–2656.
- Babcock, R. W., Malda, J., Radway, J. A. C. (2002). Hydrodynamics and mass transfer in a tubular airlift photobioreactor. *Journal of Applied Phycology*, 14(3), 169–184.
- Beenackers, A. A. C. M., Van Swaaij, W. P. M. (1993). Mass transfer in gas-liquid slurry reactors. *Chemical Engineering Science*, 48(18), 3109–3139.
- Berglund, K. A., Larson, M. A. (1984). Modeling of growth rate dispersion of citric acid monohydrate in continuous crystallizers. *AIChE Journal*, 30(2), 280–287.
- Bezzo, F., Macchietto, S. (2004). A general methodology for hybrid multizonal/CFD models: Part I. Theoretical framework. *Computers and Chemical Engineering*, 28(4), 501–551.
- Bezzo, F., Macchietto, S., Pantelides, C. C. (2003). General hybrid multizonal/CFD approach for bioreactor modeling. *AIChE Journal*, 49(8), 2133–2148.

- Bhavaraju, S. M., Russell, T. W. F., Blanch, H. W. (1978). The design of gas sparged devices for viscous liquid systems. *AIChE Journal*, 24(3), 454–466.
- Bi, H. T., Li, J. (2004). Multiscale analysis and modeling of multiphase chemical reactors. *Advanced Powder Technology*, 15(6), 607–627.
- Billet, R., Schultes, M. (1993). Predicting mass transfer in packed columns. *Chemical Engineering Technology*, 16(1), 1–9.
- Braumann, A., Kraft, M., Wagner, W. (2010). Numerical study of a stochastic particle algorithm solving a multidimensional population balance model for high shear granulation. *Journal of Computational Physics*, 229(20), 7672–7691.
- Buffo, A., Alopaes, V. (2016). Solution of bivariate population balance equations with high-order moment-conserving method of classes. *Computers and Chemical Engineering*, 87, 111–124.
- Buffo, A., Marchisio, D. L. (2014). Modeling and simulation of turbulent polydisperse gas-liquid systems via the generalized population balance equation. *Reviews in Chemical Engineering*, 30(1), 73–126.
- Buffo, A., Marchisio, D. L., Vanni, M., Renze, P. (2013). Simulation of polydisperse multiphase systems using population balances and example application to bubbly flows. *Chemical Engineering Research and Design*, 91(10), 1859–1875.
- Cents, A. H. G., Brilman, D. W. F., Versteeg, G. F. (2005). CO₂ absorption in carbonate/bicarbonate solutions: The Danckwerts-criterion revisited. *Chemical Engineering Science*, 60(21), 5830–5835.
- Chesters, A. K. (1991). The Modeling of Coalescence Processes in Fluid Liquid Dispersions - A Review of Current Understanding. *Chemical Engineering Research Design*, 69(4), 259–270.
- Clift, R., Grace, J. R., Weber, M. E. (1978). *Bubbles, Drops and Particles* (1st ed.). New York: Academic Press.
- Danckwerts, P. V. (1951). Significance of Liquid-Film Coefficients in Gas Absorption. *Industrial and Engineering Chemistry*, 43(6), 1460–1467.
- Datta, N. N., Pangarkar, V. G. (1994). Particle-Liquid Mass Transfer in Multiimpeller Mechanically Agitated Contactors. *Chemical Engineering Communications*, 129(1), 109–121.
- Datta, N. N., Pangarkar, V. G. (1996). Particle-liquid mass transfer in multi-impeller agitated three phase reactors. *Chemical Engineering Communications*, 146(1), 65–84.
- de Figueiredo, M. M. L., Calderbank, P. H. (1979). The scale-up of aerated mixing vessels for specified oxygen dissolution rates. *Chemical Engineering Science*, 34(11), 1333–1338.
- Dirksen, J. A., Ring, T. A. (1991). Fundamentals of crystallization: Kinetic effects on particle size distributions and morphology. *Chemical Engineering Science*, 46(10), 2389–2427.
- Fu, X. Y., Ishii, M. (2003). Two-group interfacial area transport in vertical air-water flow - I. Mechanistic model. *Nuclear Engineering and Design*, 219(2), 143–168.
- Fuchs, R., Ryu, D. D., Humphrey, A. E., Fuchs, R. (1971). Effect of Surface Aeration on Scale-Up Procedures for Fermentation Processes. *Industrial and Engineering Chemistry Process Design and Development*, 10(2), 190–196.
- García-Ochoa, F., Gómez, E. (2004). Theoretical prediction of gas-liquid mass transfer coefficient, specific area and hold-up in sparged stirred tanks. *Chemical Engineering Science*, 59(12), 2489–2501.
- Garside, J., Mullin, J. W., Das, S. N. (1974). Growth and Dissolution Kinetics of Potassium Sulfate Crystals in an Agitated Vessel. *Industrial Engineering Chemistry Fundamentals*, 13(4), 299–305.

- Gordon, R. G. (1968). Error Bounds in Equilibrium Statistical Mechanics. *Journal of Mathematical Physics*, 9(5), 655.
- Gubbins, K. E., Liu, Y.-C., Moore, J. D., Palmer, J. C. (2011). The role of molecular modeling in confined systems: impact and prospects. *Physical Chemistry Chemical Physics*, 13(1), 58–85.
- Guo, Z., Li, L., Han, W., Li, J., Wang, B., Xiao, Y. (2017) Interpretation of the microwave effect on induction time during CaSO₄ primary nucleation by a cluster coagulation model. *Journal of Crystal Growth*, 475, 220-231.
- Gupta, C. K. (2003). *Chemical metallurgy : principles and practice* (1st ed.). Weinheim: Wiley-VCH.
- Hagesaether, L., Jakobsen, H. A., Svendsen, H. F. (2002). A model for turbulent binary breakup of dispersed fluid particles. *Chemical Engineering Science*, 57(16), 3251–3267.
- Han, B., Qu, H., Niemi, H., Sha, Z., Louhi-Kultanen, M. (2014a). Mass Transfer and Kinetics Study of Heterogeneous Semi-Batch Crystallization of Magnesium Carbonate. *Chemical Engineering Technology*, 37(8), 1363–1368.
- Han, B., Qu, H., Niemi, H., Sha, Z., Louhi-Kultanen, M. (2014b). Mechanistic study of magnesium carbonate semibatch reactive crystallization with magnesium hydroxide and CO₂. *Industrial and Engineering Chemistry Research*, 53(30), 12077–12082.
- Harriott, P. (1962). Mass transfer to particles: Part I. Suspended in agitated tanks. *AIChE Journal*, 8(1), 93–101.
- Higbie, R. (1935). The rate of absorption of a pure gas into a still liquid during short periods of exposure. *Transactions of the American Institute of Chemical Engineers*, 31, 365–389.
- Hjortso, M. A. (2005). *Population Balances in Biomedical Engineering*. New York: McGraw-Hill Education.
- Hounslow, M. J., Mumtaz, H. S., Collier, A. P., Barrick, J. P., Bramley, A. S. (2001). A micro-mechanical model for the rate of aggregation during crystallization from solution. *Chemical Engineering Science*, 56(7), 2543–2552.
- Hu, Y., Liang, J. K., Myerson, A. S., Taylor, L. S. (2005). Crystallization Monitoring by Raman Spectroscopy: Simultaneous Measurement of Desupersaturation Profile and Polymorphic Form in Flufenamic Acid Systems, 44(5), 1233–1240.
- Hughmark, G. A. (1974). Hydrodynamics and mass transfer for suspended solid particles in a turbulent liquid. *AIChE Journal*, 20(1), 202–204.
- Hulburt, H. M., Katz, S. (1964). Some problems in particle technology: A statistical mechanical formulation. *Chemical Engineering Science*, 19(8), 555–574.
- Ishii, M., Zuber, N. (1979). Drag coefficient and relative velocity in bubbly, droplet or particulate flows. *AIChE Journal*, 25(5), 843–855.
- Iveson, S. M. (2002). Limitations of one-dimensional population balance models of wet granulation processes. *Powder Technology*, 124(3), 219–229.
- Jakobsen, H. A., Håvard Lindborg, Dorao, C. A. (2005). Modeling of Bubble Column Reactors: Progress and Limitations. *Industrial Engineering Chemistry Research*, 44(14), 5107–5151.
- Jones, A., Rigopoulos, S., Zauner, R. (2004). Crystallization and crystallization engineering. *Computer Aided Chemical Engineering*, 18(C), 75–86.
- Joshi, J. B., Nandakumar, K. (2015). Computational Modeling of Multiphase Reactors. *Annual Review of Chemical and Biomolecular Engineering*, 6, 347–378.
- Kagoshima, M., Mann, R. (2006). Development of a networks-of-zones fluid mixing model for an unbaffled stirred vessel used for crystallization. *Chemical Engineering Science*, 61(9), 2852–2863.

- Kawase, Y., Halard, B., Moo-Young, M. (1987). Theoretical prediction of volumetric mass transfer coefficients in bubble columns for Newtonian and non-Newtonian fluids. *Chemical Engineering Science*, 42(7), 1609–1617.
- Kawase, Y., Hashiguchi, N. (1996). Gas–liquid mass transfer in external-loop airlift columns with newtonian and non-newtonian fluids. *The Chemical Engineering Journal and the Biochemical Engineering Journal*, 62(1), 35–42.
- Kendal, D. G. (1950). An artificial realization of a simple birth-and-death process. *Journal of the Royal Statistical Society: Series B*, 12, 116–119.
- Kostoglou, M., Karabelas, A. J. (2005). Toward a unified framework for the derivation of breakage functions based on the statistical theory of turbulence. *Chemical Engineering Science*, 60(23), 6584–6595.
- Kramer, H. J. M., Dijkstra, J. W., Verheijen, P. J. T., Van Rosmalen, G. M. (2000). Modeling of industrial crystallizers for control and design purposes. *Powder Technology*, 108(2–3), 185–191.
- Kramer, T., Clark, M. (1999). Incorporation of Aggregate Breakup in the Simulation of Orthokinetic Coagulation. *Journal of Colloid and Interface Science*, 216(1), 116–126.
- Kumar, S., Ramkrishna, D. (1996a). On the solution of population balance equations by discretization—I. A fixed pivot technique. *Chemical Engineering Science*, 51(8), 1311–1332.
- Kumar, S., Ramkrishna, D. (1996b). On the solution of population balance equations by discretization—II. A moving pivot technique. *Chemical Engineering Science*, 51(8), 1333–1342.
- Laakkonen, M. (2006). Development and Validation of Mass Transfer Models for the Design of Agitated Gas-Liquid Reactors. Ph.D. Thesis, Tekillinen korkeakoulu, Espoo.
- Laakkonen, M., Alopaeus, V., Aittamaa, J. (2006). Validation of bubble breakage, coalescence and mass transfer models for gas-liquid dispersion in agitated vessel. *Chemical Engineering Science*, 61(1), 218–228.
- Laakkonen, M., Moilanen, P., Alopaeus, V., Aittamaa, J. (2007). Modelling local bubble size distributions in agitated vessels. *Chemical Engineering Science*, 62(3), 721–740.
- Lal, P., Kumar, S., Upadhyay, S. N., Upadhya, Y. D. (1988). Solid-Liquid Mass Transfer in Agitated Newtonian and Non-Newtonian Fluids. *Industrial Engineering Chemistry Research*, 27(7), 1246–1259.
- Lane, G. L., Schwarz, M. P., Evans, G. M. (2005). Numerical modelling of gas-liquid flow in stirred tanks. *Chemical Engineering Science*, 60(8–9), 2203–2214.
- Lee, C.-H., Erickson, L. E., Glasgow, L. A. (1987). Bubble Breakup and Coalescence in Turbulent Gas-Liquid Dispersions. *Chemical Engineering Communications*, 59(1–6), 65–84.
- Lehr, F., Millies, M., Mewes, D. (2002). Bubble-size distributions and flow fields in bubble columns. *AIChE Journal*, 48(11), 2426–2443.
- Levins, D. M., Glastonbury, J. R. (1972). Application of Kolmogoroff's theory to particle-liquid mass transfer in agitated vessels. *Chemical Engineering Science*, 27(3), 537–543.
- Li, D., Gao, Z., Buffo, A., Podgorska, W., Marchisio, D. L. (2016). Droplet breakage and coalescence in liquid-liquid dispersions: Comparison of different kernels with EQMOM and QMOM. *AIChE Journal*, 63(6), 2293–2311.
- Li, L., Guo, Z., Han, W., Wang, Q. (2017). The effect of microwave on the primary nucleation of CaSO₄ from aqueous solutions. *Powder Technology*, 317, 189–196.
- Logashenko, D., Fischer, T., Motz, S., Gilles, E. D., Wittum, G. (2006). Simulation of crystal growth and attrition in a stirred tank. *Computing and Visualization in Science*, 9(3), 175–183.

- Luo, H., Svendsen, H. F. (1996). Theoretical Model for Drop and Bubble Breakup in Turbulent Dispersions. *AIChE Journal*, 42(5), 1225–1233.
- Marchisio, D. L. (2013). *Computational Models for Polydisperse Particulate and Multiphase Systems* (1st ed.). Cambridge: Cambridge University Press.
- Marchisio, D. L., Fox, R. O. (2005). Solution of population balance equations using the direct quadrature method of moments. *Journal of Aerosol Science*, 36(1), 43–73.
- Marchisio, D. L., Pikturina, J. T., Fox, R. O., Vigil, R. D. (2003). Quadrature method of moments for population balance equations. *AIChE*, 49(5), 1266–1276.
- Marchisio, D. L., Vigil, R. D., Fox, R. O. (2003). Implementation of the quadrature method of moments in CFD codes for aggregation - breakage problems. *Chemical Engineering Science*, 58(15), 3337–3351.
- McClure, D. D., Kavanagh, J. M., Fletcher, D. F., Barton, G. W. (2014). Development of a CFD Model of Bubble Column Bioreactors: Part Two - Comparison of Experimental Data and CFD Predictions. *Chemical Engineering Technology*, 37(1), 131–140.
- McGraw, R. (1997). Description of Aerosol Dynamics by the Quadrature Method of Moments. *Aerosol Science and Technology*, 27(2), 255–265.
- Mersmann, A. S. (2001). *Crystallization Technology Handbook* (2nd ed.). New York: Marcel Dekker, Inc.
- Mitrovic, M. M., Zekic, A. A., Petrusevski, L. S. (1999). Growth rate dispersion of small KDP crystals. *Journal of Crystal Growth*, 198–199, 687–691.
- Montante, G., Lee, K. C., Brucato, A., Yianneskis, M. (2001). Numerical simulations of the dependency of flow pattern on impeller clearance in stirred vessels. *Chemical Engineering Science*, 56(12), 3751–3770.
- Morsi, S. A., Alexander, A. J. (1972). An investigation of particle trajectories in two-phase flow systems. *Journal of Fluid Mechanics*, 55(2), 193–208.
- Mullin, J.W. (2000). *Crystallization*. (3rd ed). Oxford: Butterworths-Heinemann.
- Narsimhan, G., Gupta, J. P., Ramkrishna, D. (1979). A model for transitional breakage probability of droplets in agitated lean liquid-liquid dispersions. *Chemical Engineering Science*, 34(2), 257–265.
- Nauha, E. K., Alopaeus, V. (2013). Modeling method for combining fluid dynamics and algal growth in a bubble column photobioreactor. *Chemical Engineering Journal*, 229, 559–568.
- Nauha, E. K., Alopaeus, V. (2015). Modeling outdoors algal cultivation with compartmental approach. *Chemical Engineering Journal*, 259, 945–960.
- Newman, J. S. (1991). *Electrochemical systems* (1st ed.). New Jersey: Prentice Hall.
- Nielsen, A. E. (1964). *Kinetics of crystallization* (1st ed.). Oxford: Pergamon Press.
- Nienow, A. W. (1969). Dissolution mass transfer in a turbine agitated baffled vessel. *The Canadian Journal of Chemical Engineering*, 47(3), 248–258.
- Nienow, A. W. (1975). Agitated vessel particle-liquid mass transfer: A comparison between theories and data. *The Chemical Engineering Journal*, 9(2), 153–160.
- Nienow, A. W., Miles, D. (1978). The effect of impeller/tank, configurations on fluid-particle mass transfer. *The Chemical Engineering Journal*, 15(1), 13–24.
- Noyes, A. A., Whitney, W. R. (1897). The rate of solution of solid substances in their own solutions. *The Journal of the American Chemical Society*, 19(12), 930–934.
- Nørskov, J. K., Abild-Pedersen, F., Studt, F., Bligaard, T. (2011). Density functional theory in surface chemistry and catalysis. *Proceedings of the National Academy of Sciences of the United States of America*, 108(3), 937–43.

- Olajire, A. A. (2013). A review of mineral carbonation technology in sequestration of CO₂. *Journal of Petroleum Science and Engineering*, 109, 364–392.
- Pangarkar, V. G., Yawalkar, A. A., Sharma, M. M., Beenackers, A. A. C. M. (2002). Particle - Liquid Mass Transfer Coefficient in Two-/Three-Phase. *Industrial Engineering Chemistry Research*, 41(17), 4141–4167.
- Patterson, G. K. (1975). Simulating Turbulent-Field Mixers and Reactors: Taking the Art Out of the Design. In *Turbulence in Mixing Operations* (1st ed., pp. 223–275). New York: Academic Press.
- Petitti, M., Nasuti, A., Marchisio, D. L., Vanni, M., Baldi, G., Chimica, I., Torino, P. (2010). Bubble size distribution modeling in stirred gas – liquid reactors with QMOM augmented by a new correction algorithm. *AIChE Journal*, 56(1), 3–5.
- Phillips, V. R., Epstein, N. (1974). Growth of nickel sulfate in a laboratory-scale fluidized-bed crystallizer. *AIChE Journal*, 20(4), 678–687.
- Plewik, R., Synowiec, P., Wójcik, J., Kuś, A. (2010). Suspension flow in crystallizers with and without hydraulic classification. *Chemical Engineering Research and Design*, 88(9), 1194–1199.
- Prince, M. J., Blanch, H. W. (1990). Bubble coalescence and break-up in air-sparged bubble columns. *AIChE Journal*, 36(10), 1485–1499.
- Ramkrishna, D. (2000). *Population balances: theory and applications to particulate systems in engineering* (1st ed.). New York: Academic Press.
- Ranade, V. V. (2001). *Computational Flow Modeling for Chemical Reactor Engineering*. (1st ed.). Amsterdam: Academic Press.
- Randolph, A. D., Larson, M. A. (1988). *Theory of particulate processes: analysis and techniques of continuous crystallization* (2nd ed.). New York: Academic Press.
- Randolph, A. D., White, E. T. (1977). Modeling size dispersion in the prediction of crystal-size distribution. *Chemical Engineering Science*, 32(9), 1067–1076.
- Rigopoulos, S., Jones, A. (2003). A hybrid CFD-reaction engineering framework for multiphase reactor modelling: Basic concept and application to bubble column reactors. *Chemical Engineering Science*, 58(14), 3077–3089.
- Rigopoulos, S., Jones, A. G. (2001). Dynamic modelling of a bubble column for particle formation via a gas-liquid reaction. *Chemical Engineering Science*, 56(21–22), 6177–6184.
- Risso, F., Fabre, J. (1998). Oscillations and breakup of a bubble immersed in a turbulent field. *Journal of Fluid Mechanics*, 372, 323–355.
- Rod, V., Misek, T. (1982). Stochastic Modelling of Dispersion Formation in Agitated Liquid-Liquid Systems. *Transactions of the Institution of Chemical Engineers and the Chemical Engineers*, 60(1), 48–53.
- Sada, E., Kumazawa, H. (1973). Gas absorption accompanied by a complex reaction: variation of the enhancement factors with the orders of reaction. *Chemical Engineering Science*, 28(10), 1903–1905.
- Sajjadi, B., Raman, A. A. A., Ibrahim, S., Shah, R. S. S. R. E. (2012). Review on gas-liquid mixing analysis in multiscale stirred vessel using CFD. *Reviews in Chemical Engineering*, 28(2–3), 171–189.
- Salmi, T., Mikkola, J.-P., Warna, P. (2011). *Chemical reaction engineering and reactor technology* (1st ed.). Boca Raton: CRC Press.
- Sander, R. (2015). Compilation of Henry's law constants (version 4.0) for water as solvent. *Atmospheric Chemistry and Physics*, 15(8), 4399–4981.

- Scargiali, F., D’Orazio, A., Grisafi, F., Brucato, A. (2007). Modelling and Simulation of Gas–Liquid Hydrodynamics in Mechanically Stirred Tanks. *Chemical Engineering Research and Design*, 85(5), 637–646.
- Schiller, L., Naumann, Z. (1933). A drag coefficient correlation. *Z.Ver.Deutsch.Ing*, 77(13–14), 318–320.
- Seetharaman, S. (2005). *Fundamentals of metallurgy*. Fundamental of metallurgy (1st ed). Cambridge: CRC Press.
- Sha, Z., Oinas, P., Louhi-Kultanen, M., Yang, G., Palosaari, S. (2001). Application of CFD simulation to suspension crystallization-actors affecting size-dependent classification. *Powder Technology*, 121(1), 20–25.
- Tomiyama, A. (2004). Drag and lift and virtual mass forces acting on a single bubble. 3rd International Symposium on Two-Phase Flow Modelling and Experimentation, Pisa.
- Tomiyama, A., Kataoka, I., Zun, I., Sakaguch, T. (1998). Drag Coefficients of Single Bubbles under Normal and Micro Gravity Conditions. *JSME International Journal Series B*, 41(2), 472–479.
- Toor, H. L., Marchello, J. M. (1958). Film-penetration model for mass and heat transfer. *AIChE Journal*, 4(1), 97–101.
- Trambouze, P., Wauquier, J.-P., Van Landeghem, H. (1988). *Chemical reactors : design, engineering, operation* (1st ed.). Houston: Gulf Publishing Company.
- Tropea, C., Yarin, A. L., Foss, J. F. (2007). *Springer Handbook of Experimental Fluid Mechanics* (1st ed.). New York: Springer-Verlag Berlin Heidelberg.
- Valentas, K. J., Amundson, N. R. (1966). Breakage and coalescence in dispersed phase systems. *Industrial and Engineering Chemistry Fundamentals*, 5(4), 533–542.
- van Krevelen, D. W., Hoftijzer, P. J. (1948). Kinetics of gas-liquid reactions part I. General theory. *Recueil Des Travaux Chimiques Des Pays??Bas*, 67(7), 563–586.
- Vanni, M. (2000). Approximate Population Balance Equations for Aggregation-Breakage Processes. *Journal of Colloid and Interface Science*, 221(2), 143–160.
- Varma, S., Chen, P.-C., Unnikrishnan, G. (2011). Gas–liquid reactive crystallization for the synthesis of CaCO₃ nanocrystals. *Materials Chemistry and Physics*, 126(1), 232–236.
- Vasconcelos, J. M. T., Alves, S. S., Barata, J. M. (1995). Mixing in gas-liquid contactors agitated by multiple turbines. *Chemical Engineering Science*, 50(14), 2343–2354.
- Vlaev, S. D., Valeva, M. D., Mann, R. (2002). Some effects of rheology on the spatial distribution of gas hold-up in a mechanically agitated vessel. *Chemical Engineering Journal*, 87(1), 21–30.
- Von Smoluchowski, M. (1917). *Versuch einer mathematischen Theorie der Koagulationskinetik kolloider Lösungen* (1st ed.). Frankfurt: Geest Portig.
- Wachi, S., Jones, A. (1991). Effect of gas–liquid mass transfer on crystal size distribution during the batch crystallization of calcium carbonate. *Chemical Engineering Science*, 46(12), 1027–1033.
- Walter, J. F., Blanch, H. W. (1986). Bubble break-up in gas-liquid bioreactors: Break-up in turbulent flows. *The Chemical Engineering Journal*, 32(1), B7–B17.
- Wang, T., Wang, J., Jin, Y. (2003). A novel theoretical breakup kernel function for bubbles/droplets in a turbulent flow. *Chemical Engineering Science*, 58(20), 4629–4637.
- Wang, T., Wang, J., Jin, Y. (2005). Population balance model for gas - Liquid flows: Influence of bubble coalescence and breakup models. *Industrial and Engineering Chemistry Research*, 44(19), 7540–7549.
- Wei, H., Garside, J. (1997). Application of CFD Modelling to Crystallization Systems. *Chemical Engineering Research and Design*, 75(2), 219–227.

- White, E., Mackintosh, D., Butler, B. (1998). Modeling growth rate dispersion (GRD) in sugar crystallization. *Proceedings of the Australian Society of Sugarcane Technologists*, 20, 524–531.
- Whitman, W. G. (1924). The Two-Film Theory of Gas Absorption. *Chemical and Metallurgical Engineering*, 29(4), 146–148.
- Wilcox, W. R. (1993). Transport phenomena in crystal growth from solution. *Progress in Crystal Growth and Characterization of Materials*, 26(C), 153–194.
- Wójcik, J. A., Jones, A. G. (1998). Particle disruption of precipitated CaCO_3 crystal agglomerates in turbulently agitated suspensions. *Chemical Engineering Science*, 53(5), 1097–1101.
- Yakhot, V., Orszag, S. A. (1986). Renormalization group analysis of turbulence. I. Basic theory. *Journal of Scientific Computing*, 1(1), 3–51.
- Yang, C., Mao, Z.-S. (2014). Preface. *Numerical Simulation of Multiphase Reactors with Continuous Liquid Phase* (1st ed.). New York: Chemical Industry Press.
- Yawalkar, A. a, Heesink, A. B. M., Versteeg, G. F., Pangarkar, V. G. (2002). Gas-Liquid Mass Transfer Coefficient in Stirred Tank Reactors. *Canadian Journal of Chemical Engineering*, 80(5), 840–848.
- Ye, W., Lin, J., Madsen, H. T., Sogaard, E. G., Hélix-Nielsen, C., Luis, P. (2016). Enhanced performance of a biomimetic membrane for Na_2CO_3 crystallization in the scenario of CO_2 capture. *Journal of Membrane Science*, 498, 75–85.
- Yeoh, G. H., Cheung, C. P., Tu, J. (2014). *Multiphase Flow Analysis Using Population Balance Modeling: Bubbles, Drops and Particles* (1st ed.). New York: Butterworth-Heinemann.
- Yuan, C., Fox, R. O. (2011). Conditional quadrature method of moments for kinetic equations. *Journal of Computational Physics*, 230(22), 8216–8246.
- Yuan, C., Laurent, F., Fox, R. O. (2012). An extended quadrature method of moments for population balance equations. *Journal of Aerosol Science*, 51, 1–23.
- Zaccone, A., Gäbler, A., Maaß, S., Marchisio, D., Kraume, M. (2007). Drop breakage in liquid–liquid stirred dispersions: Modelling of single drop breakage. *Chemical Engineering Science*, 62(22), 6297–6307.
- Zauner, R., Jones, A. G. (2002). On the influence of mixing on crystal crystallization processes-application of the segregated feed model. *Chemical Engineering Science*, 57(5), 821–831.
- Zhao, W., Buffo, A., Alopaeus, V., Han, B., Louhi-Kultanen, M. (2017). Application of the compartmental model to the gas-liquid crystallization of CO_2 - $\text{Ca}(\text{OH})_2$ aqueous system in a stirred tank. *AIChE Journal*, 63(1), 378–386.
- Zucca, A., Marchisio, D. L., Vanni, M., Barresi, A. A. (2007). Validation of bivariate DQMOM for nanoparticle processes simulation. *AIChE Journal*, 53(4), 918–931.



ISBN 978-952-60-7915-8 (printed)
ISBN 978-952-60-7916-5 (pdf)
ISSN-L 1799-4934
ISSN 1799-4934 (printed)
ISSN 1799-4942 (pdf)

Aalto University
School of Chemical Engineering
Department of Chemical and Metallurgical Engineering
www.aalto.fi

**BUSINESS +
ECONOMY**

**ART +
DESIGN +
ARCHITECTURE**

**SCIENCE +
TECHNOLOGY**

CROSSOVER

**DOCTORAL
DISSERTATIONS**